Universität Ulm | 89069 Ulm | Germany

Fakultät für Naturwissenschaften
Institut für Quantenoptik

Hochauflösende Mikroskopie und Spektroskopie an einzelnen Fehlstellenzentren in Diamant

Dissertation

zur Erlangung des Doktorgrades Dr. rer. nat.
der Fakultät für Naturwissenschaften der Universität Ulm

Vorgelegt von:

Andreas Johannes Häußler

aus

Neu-Ulm

2015

Amtierender Dekan: Prof. Dr. J. Ankerhold

1. Gutachter: Prof. Dr. F. Jelezko

2. Gutachter: PD Dr. B. Naydenov

Tag der Promotion: 15. Juli 2015

CONTENTS

A DIAMOND WITH A FLAW IS BETTER THAN A COMMON STONE THAT IS PERFECT.
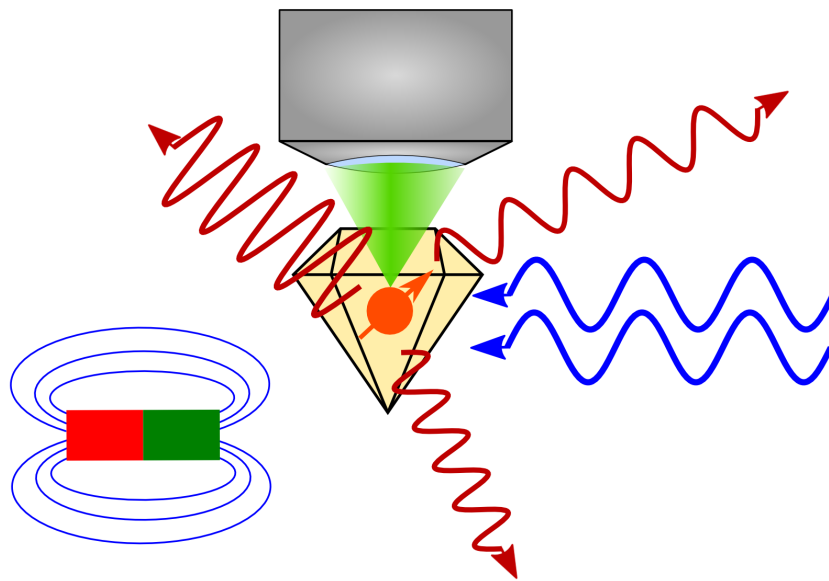
(Chinese Proverb)

Superresolution Microscopy and Spectroscopy on Single Defect Centers in Diamond

———— Preface

This thesis - titled *Superresolution Microscopy and Spectroscopy of Single Defect Centers in Diamond* - explores precise localization techniques at the nanoscale, of Nitrogen-vacancy (NV) centers in diamond. Accurate localization of NV centers is of great current relevance since shallow NV centers ($< 10\,\mathrm{nm}$) are today being used for nanoscale magnetic sensing, coupling to photonic/plasmonic devices as well as building quantum processors. Consequently, the challenges of knowing the exact positions of these emitters, both the position in relation to other NV centers as well as the precise determination of the depth below the surface of the diamond, is important.

This manuscript will address the problem by three different types of experiments. First, non-linear imaging by using ground state depletion microscopy (GSD) has been used to characterize the precise positioning of custom-created NV centers. By this method, it was possible to optically resolve the position of different emitters, that were located in a single diffraction limited spot. Such close NV centers separated from each other by less than $50\,\mathrm{nm}$ show strong dipole-dipole coupling and are promising candidates to build a quantum information processor. Thus, precise localization is one important step for further advances.

The second experiment dealt with accurate determination of the depth of NV centers in diamond by an adaption of fluorescence imaging with one nanometer accuracy (FIONA). Recently, techniques involving etching of the diamond or magnetic resonance force microscopy (MRFM) have been developed to determine the depth, however these techniques are either destructive or require a combined MRFM and confocal microscope. Here we demonstrate that the same sensitivity can be achieved by purely optical methods. The results are promising for e.g. fast investigation of implantation processes as well as precise imaging along the optical axis, that could provide additional information in the sensing of single molecules. In addition we exactly characterize the optical aberrations for imaging in diamond which is of interest to those performing super-resolution microscopy with diamond defects.

However, it may be convenient to be not solely limited to optical imaging for localization. Especially, if one wants to exploit the sensitivity of the NV to environmental conditions or to use them as sensors e.g. for electric and magnetic fields. Therefore localization and sensitivity are closely intertwined. This is addressed in our third experiment, that combines determination of depth with the ability to measure small amounts of spins in a liquid outside the diamond. We show the design and construction of a microfluidic channel, that was cut directly in the diamond. The characterization of implanted NV centers confirms the shallow depth of the defects by a simultaneous demonstration of the capability to detect less than 100 randomly fluctuating spins in the environment. The results are a promising foundation for further investigation and can be regarded as a novel application to spin sensing in liquids by single NV centers.

In all, the presented thesis enhances the scope of known localization techniques as well

as the application of single NV centers to sensing experiments. Some of the results, like the purely optical determination of depths, are not limited to defects in diamond, but principally are transferable to all tasks of relative localization problems along the optical axis. Other gained insights, especially the discussion of magnetic sensing in liquids, will allow a direct continuation by a variety of different measurements, that combine microfluidic experiments with the sensitivity of single NV centers.

Looking Beyond

A basic trait of mankind seems to be its never-ending quest for knowledge. Over the centuries, the *homo sapiens* (lat. 'wise man') has gained quite an impressive insight into the mechanisms that underlie the processes of the universe (to be more specific: of our little corner in space-time in which we can perform experiments and observations). A first fundamental prerequisite to gain this level of insight is man's ability to think in abstract systems and to perform *gedankenexperiments*. A second is the adaptation of this natural philosophy to the real world in conducting experiments and testing the theories. This is where science begins, most of the time hand in hand with advances in engineering to provide proper test facilities.

Naturally, the limit of our understanding of nature was always defined by the access of information one could get from the outside world. Since most of this information is related to one's visual perception, the ability to enhance one's limited sight plays a major role in this progress. A technical revolution started around the year 1600 when the Dutch developed techniques for precise grinding and polishing of glass lenses. This led to the invention of the first complex optical instruments, namely the telescope and the microscope. In the course of years the apparatuses for magnifying small structures became more and more refined and helped scientists and engineers from various disciplines to work on systems that could hardly be seen with the naked eye. Finally, the theoretical foundations of microscopy were laid down by Ernst Abbe in 1873 [1]. His famous resolution limit stated that the resolvable distance of two nearby points was defined by the wavelength of light and the aperture of the microscope. Thus, the achievable resolution for visible light cannot be smaller than about 200 nm.

This value was believed to be the absolute limit in optical microscopy for around a century. The first theoretical challenge to this barrier was proposed in 1971 by the method of 4π-microscopy in which a holographic imaging in all spatial directions was suggested [2] [3]. Stefan Hell was the one to realize such a microscope by using two opposing objectives in 1994 [4] [5]. In the same year Hell suggested an even more sophisticated technique: stimulated-emission-depletion microscopy (STED) [6]. This technique uses a nonlinear saturation process of a fluorescent emitter to squeeze the effective point spread function (PSF) of the microscope depending on the power of the excitation beam. The experimental proof followed in 1999 [7]. Due to its widespread application in localization [8] [9] [10], especially of biomolecules [11] [12] [13], Stefan Hell was awarded the Nobel prize in 2014 for this achievement. A similar though slightly different method as STED is ground state depletion microscopy (GSD), which was developed at the same time [14]

[15] [16]. Both methods are able to achieve a resolution of about 10 nm.

Since the first accomplishments in breaking the diffraction limit have been achieved, there has been a rapid progress in the development of other techniques that are able to perform superresolution imaging. Most of these methods rely on knowledge about physical properties of the imaged object, e.g. the method of photoactivated localization microscopy (PALM) [17] [18] or stochastic optical reconstruction microscopy (STORM) [19] [20], which use controlled switching of fluorescent markers.

However, there is a second approach to overcome the diffraction limit: fluorescence imaging with one nanometer accuracy (FIONA) [21]. Here, the position of the emitter is assumed to be at the maximum of the point spread function (PSF) of an isolated emitter. Typically the PSF is approximated as a Gaussian intensity profile and will be fitted to the measured image data [22] [23]. Consequently the number of collected photons determines the precision of the localization and can be much better than the diffraction limited spot size given by the full width half maximum of the PSF [24].

FIONA has been mainly used to increase the lateral resolution in the object plane by the use of widefield microscopy with charge-coupled-device (CCD) detectors [25] [26]. Since three dimensional tracking of particles is of great interest in many applications, different techniques based on the FIONA principle have been developed in recent years, e.g. confocal imaging with an achieved precision of 50 nm [27]. Even better results can be accomplished by other techniques like the application of special formed PSF with a precision of 20 nm [28] or defocused imaging with a resolution down to 5 nm [29]. In this thesis, such an approach is presented to localize single Nitrogen-Vacancy (NV) centers below a diamond surface with nanometer accuracy. Due to the high photostability of these emitters and the stable positioning, their depth could be determined down to an accuracy of 2.6 nm [30].

Applied Quantum World

The further we push the resolution of objects towards the atomic scale, the more apparent becomes their underlying trait: nature is quantized and non-classical, and these effects even emerge on the scale of large organic molecules [31] [32]. Since the rise of quantum theory in the early 20th century [33] [34] [35] [36] [37], its theoretical predictions and experimental confirmations have advanced in a triumphal procession to revolutionize our understanding of nature [38] [39]. Nowadays, access to the quantum world is as easy as it gets: one of the many defects in diamond, the Nitrogen-vacancy center (NV) proves to be an ideal candidate to study numerous quantum effects, even under standard ambient conditions [40] [41].

The NV center can be described as an atom-like system that is trapped in the diamond lattice. Due to its high fluorescence stability it can be used as a fluorescent marker in nanodiamonds [42] [43] as well as a single photon source [44] [45]. One of its most interesting features however is the spin-dependent fluorescence intensity of the negatively charged state of the NV (the NV^- state). The two different spin configurations of its unbound electron pair (parallel spin or anti-parallel spin) show a contrast in fluorescence

intensity of about 30%. This allows a purely optical readout of the spin state [46], that in addition can easily be initialized in the ground state altogether with long coherence times up to milliseconds [47] [48]. Thus the NV center is an ideal system to test protocols for quantum information processing (QIP) [49] and lay a foundation to the development of a solid-state quantum computer [50] [51]. As an example it is possible to couple the electron spin to the nuclear spin of the Nitrogen or a nearby ^{13}C atom in the diamond to create quantum logical gates [52]. Besides experiments with a quantum register of coupled NV centers that show promising coherence and readout fidelities have also been performed [53] [54]. Another interesting application is the proof of the non-classical behavior of quantum theory. This has been shown by experiments that confirm the violation of the Bell inequality [55].

Moreover, the energy splitting in the ground state proves to be very sensitive to its environment. Experiments have shown that the NV center can be used as a sensor for magnetic [56] [57] [58] [59] and electric fields [60], external spins [61] [62] [63] [64], temperature [65] [66] [67] and pressure [68]. Recent applications of NV centers include experiments in nanodiamonds to measure fields in biological samples like cells [69], highly efficient fluorescence resonance energy transfer (FRET) sensing to investigate optically active molecules [70] [71] or the combination of atomic force microscopy and magnetic resonance imaging to be applied in magnetic resonance force microscopy (MRFM) [72] [73] [74] [75]. Parts of this thesis will cover experiments that use single NV centers as a probe to measure magnetic fields created by external spins outside the diamond.

Thesis Outline

As mentioned in the beginning, this thesis deals with the application of single Nitrogen-vacancy centers to precise localization techniques in microscopy and magnetic sensing of single spins in liquids. Therefore, chapter 1 will give an introduction to imaging theory and recent methods of superresolution microscopy. After that, basic properties of the Nitrogen-vacancy center will be described, as well as its applications to measurements of magnetic fields and external spins outside the diamond (chapter 2).

The experimental part of this work presents a description of the configurations of the setup for the performed experiments in chapter 3. This is followed by a detailed discussion about the measurements and the results. Chapter 4 will present superresolution measurements on NV centers by GSD microscopy. With this nonlinear imaging technique, a resolution below 20 nm in the plane perpendicular to the optical axis have been achieved. In fact, we were able to resolve a pair of two NV centers as close as 14 nm The main work of this thesis consists of a second type of experiment. Fluorescence imaging with one-nanometer accuracy (FIONA) was applied and adapted, to determine the depth of implanted NV centers as described in chapter 5. The results can be found in chapter 6, where we report an achieved accuracy of about 2.6 nm along the optical axis for shallow emitters. Additionally, it was shown that the shift of a focal point in a high refractive index material is dependent on its distance to the surface. For this issue a theoretical model was calculated that matches the behavior of our experimental results. The last type of performed experiments uses shallow implanted single NV centers to combine the determination of depth to their sensitivity of external spins. This was done by measuring the effect of single spins in liquids near the surface of the diamond on the coherence times of NV centers (chapter 7). Hence, we show the realization of a microfluidic chamber and prove a sensitivity of the NV centers to a small number (< 100) of external spins.

The main results of the depth localization experiments have been published in [30].

1 – Optical Imaging and Resolution

This chapter covers the basic concepts of optical imaging and resolution. After a general introduction on imaging there will be a discussion about resolution and methods to improve the technical limits of optical microscopes. The emphasis of the following sections will be a description of the superresolution microscopy techniques of ground state depletion (GSD) and fluorescence imaging with one-nanometer accuracy (FIONA) that have been used in the experimental part of this thesis.

1.1 Fundamentals of Optical Imaging and Microscopy

This first section deals with the basic concepts that underlie the formation of an optical image in the far-field and the consequences for far-field-microscopy. Starting from a general point of view it will present the idea of imaging and resolution in microscopy. For a more detailed portrayal of imaging than given in this thesis the author recommends the *Handbook of Optical Systems (Vol.1-3)* [76] [77] [78], that provides one of the largest scopes on this topic of all textbook series.

1.1.1 Optical Far-Field-Imaging

In a general (mathematical) sense an image is the result of projecting one space (called the object space) onto a second space (called the image space) by a transfer function. In physics the object space is typically represented by the properties of interest of a system one wants to measure. The measurement then has to proceed as follows: i) The system interacts with a calibrated probe. ii) Due to this interaction physical properties of the probe will be altered and iii) this change can be measured by a detector which represents the image space.

This description occurs in optical imaging and is illustrated in figure 1.1. Here light represents the probe that interacts with structures of an object. To be more precise the visible light interacts with the electrons in the atomic shells of the molecules respectively the atoms. Depending on the properties of the object and the light a variety of processes can take place, e.g. scattering, diffraction, absorption or fluorescence - to name a few effects. The light waves propagating from the object contain information about both geometrical structure and energetic properties of the object. An imaging system then guides the light (typically using an assembly of lenses and apertures) to the image plane, where a detector converts the light into a measurable quantity (e.g. the blackness of a photographic film or the count of photons measured by an avalanche photodiode (APD)).
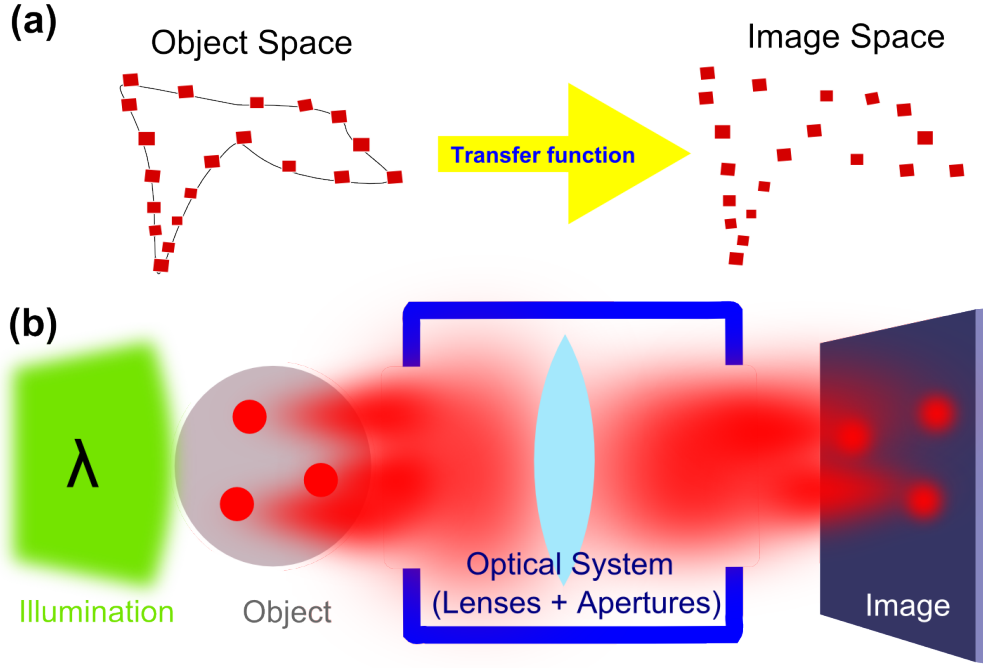
Figure 1.1: **General imaging and optical imaging.** (a) Information about an object is mapped onto an image by a transfer function. The red squares represent the fraction of the object's properties that can be measured. The amount of information gained in one single measurement is both limited by technical reasons (the transfer function) as well as by natural boundaries like Heisenberg's principle of uncertainty. (b) In case of an optical image, light interacts with the sample. Part of the collected light is then guided to a detector where the image is stored, typically in a two-dimensional pattern. Depending on the experiment this can contain spatial information as well as energetic properties of the object.

Now this consideration will be specifically applied to optical imaging in the far-field. Here the distances between the object, the imaging system and the image plane are much larger than the wavelengths of visible light. In diffraction theory this configuration is referred to as the Fraunhofer approximation. The fundamental approximation in the far-field is the description of these waves as planar waves that are given by a form of $\sim e^{i\left(\omega t - \vec{k} \cdot \vec{x}\right)}$. As stated above the spatial information is contained in all light propagating from the object. Note that this spatial information $I\left(\vec{x}\right)$ is transformed into a function of the direction of the propagating light $\tilde{I}\left(\vec{k}\right)$. This can be referred to the Fraunhofer diffraction pattern, that mathematically is defined as a Fourier transformation from real space to the spatial frequency domain of the structure of the object.

This is important for the description of the imaging process as shown in figure 1.2. An optical system e.g. a lens will collect all light within its aperture diameter and focus the

single waves to another image. On the assumption that the optical system just redirects every single wave the resulting image will be a superposition of all these waves. For an ideal lens all wavefronts with the same vector $\vec{k}$ will be directed to a certain point in the back focal plane wherefrom every single ray propagates on to the image plane. In an ideal case all light from one point of the object plane will finally reunify in one point in the image plane.
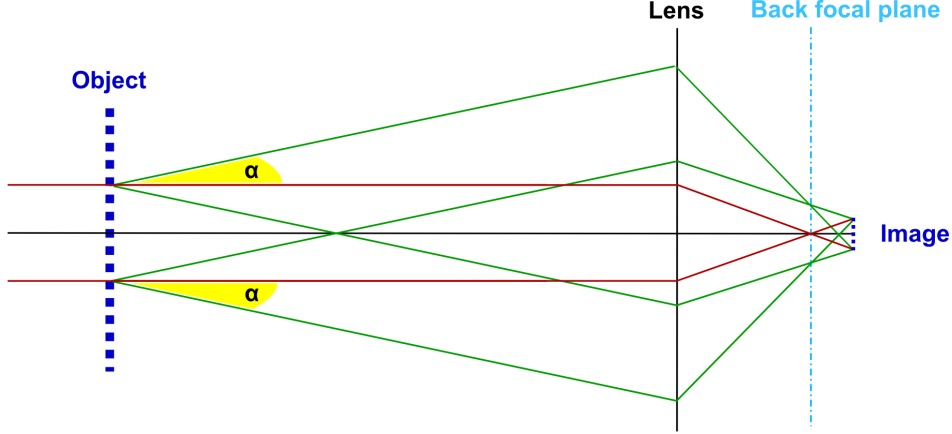

Figure 1.2: **Fourier transformation of a light signal by lenses into an image plane.** The information of the spatial frequency of the lattice is stored in the propagation direction α of the diffraction maximums. A lens projects the image of the Fraunhofer diffraction pattern from infinity to its back focal plane. The emerging light reunifies in the image plane. Since both operations are given by two serial Fourier transformations the image will occur upside down. In case of too small distances of the lattice the spatial frequencies will be related to angles too high to be imaged properly by the imaging system.

The position of the image plane is given by the well-known image formation equation

$$\frac{1}{g} + \frac{1}{b} = \frac{1}{f} \tag{1.1}$$

where g (resp. b) represents the distance from the object plane (resp. image plane) to the principal plane of the optical system and f denotes the focal length. Furthermore, the formation of the image can be calculated by two Fourier transformations in a row of the object's spatial information. Therefore, the reconstructed image $I_{image}(\vec{x})$ will emerge from the the diffraction pattern $\tilde{I}(\vec{k})$ as follows:

$$I_{image}(\vec{x}) = \frac{1}{\sqrt{2\pi}} \int_{-\infty}^{\infty} \tilde{I}(\vec{k}) \cdot e^{-i\vec{k}\cdot\vec{x}} d\vec{x} . \tag{1.2}$$

Note that this equation only holds in the case of an ideal measurement where the optical system is able to detect an unlimited range of spatial frequencies without any losses. In reality limitations of the system will lead to a loss of information and decrease the quality of the image. The next two sections will discuss these effects.

1.1.2 The Resolution Limit

Following the deliberations in the previous chapter, one consequently arrives at Abbe's conclusion for the resolution limit. At first, since the information is stored in the diffraction pattern, we know the imaged structure can not be much smaller than the wavelength. Second, small patterns in real space are related to high spatial frequencies. In case of our microscope that refers to a large angle of the propagating wavefront to the optical axis. Thus the entrance pupil of the microscope has to be large enough. Combining these two limiting constraints one arrives at Abbe's formula for a resolvable distance d [1]:

$$d = \frac{\lambda}{2 \cdot NA} \ .$$ (1.3)

Here, λ represents the wavelength of the light and $NA = n \cdot \sin \alpha$ denotes the numerical aperture of the microscope that is given by the refractive index n of the material between objective and focal spot and the half aperture angle α of the objective. Note that this is the most famous form of the equation that holds for the case of the same NA for the illumination system and the objective. For other circumstances the factor of $\frac{1}{2}$ will have to be slightly modified.

An important application of Abbe's resolution principle is the so called Rayleigh criterion (see figure 1.3) [79]. Here the illumination is neglected and one considers the image of a self-illuminated spot respectively the distinction between two spots that are positioned close to each other. For each spot the intensity $I(r)$ of the diffraction pattern in a distance r to the optical axis is given by

$$I(r) \sim \left(\frac{J_1 \left(2\pi r \right)}{\pi r} \right)^2$$ (1.4)

where J_1 is the first-order Bessel function. If the distance d between the maximums of both single diffraction patterns is larger than the distance between one maximum and the first null of the Bessel function then the two spots are defined as being resolvable, and they are separated at a contrast of about 74%. That relates to an resolution of

$$d = \frac{0.61 \cdot \lambda}{NA}$$ (1.5)

in the focal plane and

$$d_z = \frac{2\lambda \cdot n}{NA^2}$$ (1.6)

along the optical axis [80]. As can be seen in figure 1.3, the crucial factor to determine the resolution is the width of the distribution of imaged light of an illuminated point. This
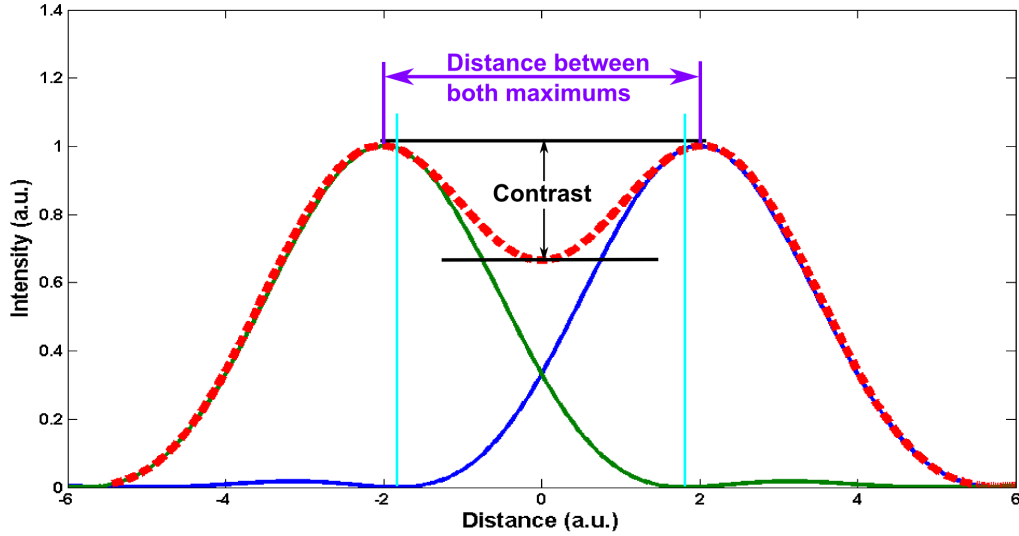
Figure 1.3: **The Rayleigh criterion.** Two nearby self-illuminated points can be distinguished if the contrast between the two maximums of the point spread functions (blue and green) is high enough. Here the total intensity pattern (red) shows a dip that drops below 74% of the maximum. According to Lord Rayleigh's suggestion to define the points to be resolved in case the distance of one maximum to the other (purple) is larger than the distance to the first minimum (light blue), our exemplary points are resolved.

distribution is called point spread function (PSF) as it describes the impulse response of the optical system to a δ-like light signal. By common definition the full width half maximum (FWHM) of this function characterizes the resolution of the optical system. A first approach to improve the resolution is the principle of confocal microscopy (see figure 1.4) [81] [82]. In this technique the objective of the microscope collects light from the diffraction limited volume in the focal plane (so called 'voxel'). This light is then focused through a small aperture in front of the image plane of the detector (the 'pinhole'). Hence, all light that is not originating from the focal plane will be canceled out and not detected. One can show the improvement of the resolution compared to a conventional microscope of a factor $\sqrt{2}$ [83]. However, the trade-off is the limited detection volume. If one wants to get information from different areas of the sample it is necessary to scan the specimen step by step.

Since the resolution of a confocal microscope of about 200 nanometers is convenient for most biological samples and lots of applications in microscopy, variations of this technique have become a common tool and widely used in research.
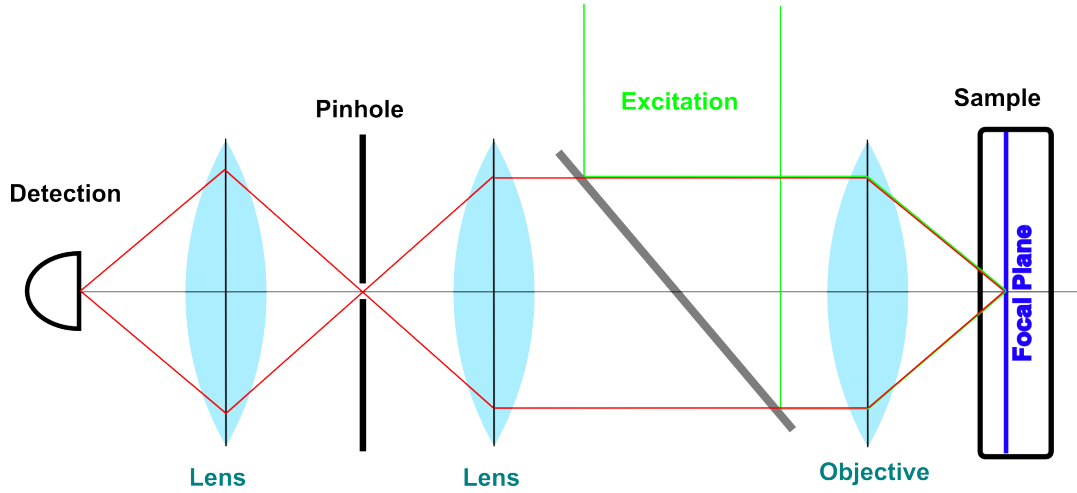
Figure 1.4: **Confocal Microscopy.** A pinhole is added to the detection path to prevent light from outside the image plane to pass to the detector. Light originating from the focal spot of the objective will be focused through this aperture to be imaged on the detector. As a consequence only the confocal spot can be imaged at one time, and thus, in case of several spots of interest, the sample the has to be scanned.

1.1.3 Aberrations

Diffraction is not the only limitation to achieve an ideal image. The optical system itself has intrinsic flaws, that lead to an imperfect imaging. These effects are called aberrations and are caused by unequal focal points of light rays depending on e.g. their incident angle on a lens or their distance to the optical axis. A description of the geometrical aberrations can be given by the Zernike polynomials that are defined on a unit circle [84] [85]. These errors can be classified in several types of errors, the so called Seidel aberrations [86], depending on the coordinates that are related to a wavefront and its distortion relatively to an ideal image [87] [88].

In this work, two aberrations play a major role that influence the results of the depth determination: spherical aberrations and chromatic aberrations. They are illustrated in figure 1.5. First the emitter is placed below a surface with different refractive index to the surrounding medium. Consequently this flat surface acts like a lens with an infinite curvature radius and shifts the focal points for different incident angles of light. In section 5.3 this effect will be discussed and calculated in detail to model the effective shift of the focal point. Second to determine the position of single emitters along the optical axis relative to the surface, two light signals have to be measured simultaneously. To distinguish the emitter's fluorescence from the reflected light, the excitation will be performed off-resonant with green light, whereas the fluorescence lies in the red. Consequently the relative position of both signals will be subject to chromatic aberration. Hence the relative position of the maxima will be shifted due to slightly displaced

focal points of both colors. This displacement error will be corrected by a calibration measurement, as discussed in detail in section 5.2.3.
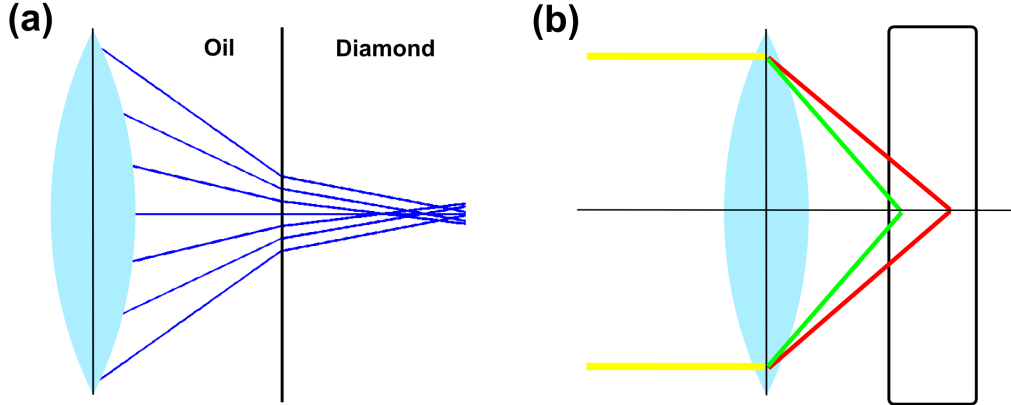

Figure 1.5: **Aberrations in the depth-localization experiment.** (a) The objective focuses the beam to image the emitter, that is placed inside the diamond. The diamond surface acts like a lens with high spherical aberrations that will lead to a different focal point of the parts of the beam, depending on the distance to the optical axis. Hence the refracted light will show a blurred focal region with a shifted effective focal point. (b) Fluorescent light of the emitter (red) will be simultaneously measured as the reflected light from the surface (green). Due to dispersion in the optical components of the microscope, both signals will show a deviation of the relative distance. In this depiction the additional refraction at the diamond surface has been neglected.

1.2 Superresolution Imaging by Depletion Microscopy

Since a focused light beam will always result in a blurred spot due to diffraction, this seems like an absolute barrier in far-field imaging. Mathematically this limit is defined by the linear imaging process, that is given by a Fourier transform (see equation 1.2). However this only holds in case of no additional knowledge about excitation or emission processes. If one already knows details about the system and its interaction this can be used to acquire additional information. This is the basic condition of all concepts that challenge the diffraction barrier: if there exists a nonlinear relation of the excitation to the imaged intensity, the system can be - in principle - resolved better than the diffraction limited spot.

First suggestions can be traced back to the middle of the 20th century with the suggestion of modulating the excitation process [89] [90]. More recent concepts suggested the use of

multi-photon absorption, a highly non-linear process, however requiring relatively high intensities and thus not feasible for sensitive specimens [91] [92]. The first two suitable concepts occurred in the 1990s and used saturable excitations of molecular states, namely ground state depletion (GSD) [14] and stimulated emission depletion (STED) [6]. This section illustrates the underlying principles of GSD and STED microscopy.

1.2.1 Basic Principle of Ground State Depletion (GSD)

Ground state depletion microscopy has the potential of achieving resolutions down to about 10 nanometers. The basic principle of GSD requires a fluorophore with an energy level scheme similar to the one depicted in figure 1.6. The 3 energy states consist of a ground state 0, an excited state 1 and a metastable state 2 that can be reached by intersystem crossing.
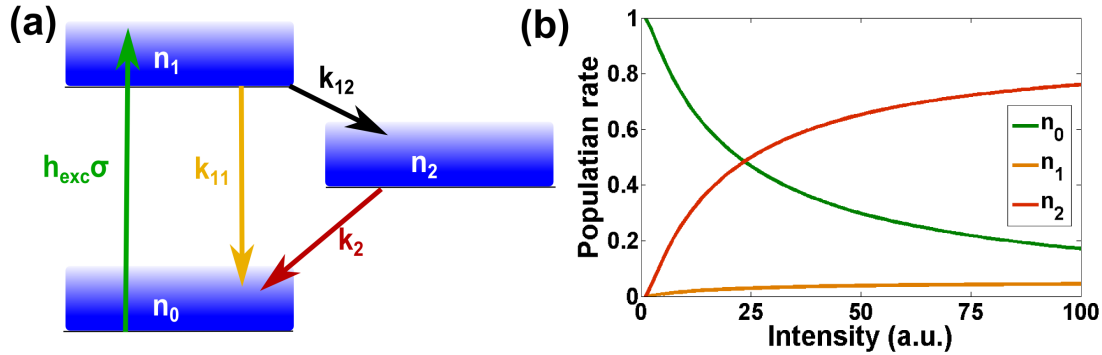

Figure 1.6: **3-level-system for GSD.** (a) A 3-level-system (the blue areas indicate vibronic energy levels related to the single states) of a typical fluorophore (e.g. a NV center) can be excited from the ground state 0 to the excited state 1. The excited state 1 shows two possible decay paths: a fast one directly back to the ground state and a second slow decay by intersystem crossing via state 2. (b) The graph shows an exemplary calculation of the expected behavior for all three states. The equilibrium of the population ratios is dependent on the excitation intensity and the decay rates. Since the decay rate from the metastable state 2 is much smaller than from state 1, higher excitation intensity will lead to a depletion of the ground state by a process quite similar to population inversion in laser excitation.

An excitation of the ground state by a photon flux h_{exc} will excite the system to state 1, depending on the effective cross section for absorption σ. In the excited state 1, the system has two opportunities to decay back to the ground state 0. One is the fast direct path by emission of a photon with the decay rate k_{11}, second is an intersystem crossing (ISC) with the rate k_{12}. In the latter case the decay back to state 0 takes much longer due to a second ISC from state 2 with the rate k_{02}. Thus the rate equations to determine

the individual populations of the states are given by

$$\frac{\mathrm{d}n_0}{\mathrm{d}t} = -h_{exc}\sigma n_0 + k_{11}n_1 + k_{02}n_2 \tag{1.7}$$

$$\frac{\mathrm{d}n_1}{\mathrm{d}t} = h_{exc}\sigma n_0 - k_{11}n_1 - k_{12}n_1 \tag{1.8}$$

$$\frac{\mathrm{d}n_2}{\mathrm{d}t} = k_{12}n_1 - k_{02}n_2 \tag{1.9}$$

Though the probability for ISC is much smaller than a direct decay, the long lifetime of the metastable state enables to reach population inversion just in a laser excitation process. The only requirement is a sufficient intensity as illustrated in figure 1.6. For higher intensities the final equilibrium of the population ratios of the ground state to the metastable state is then defined by the decay constants and the excitation intensity. By increasing the excitation intensity this equilibrium can be shifted to a higher population in the metastable state until there is barely any population left in the ground state. That is why this method is called ground state depletion.

Assuming saturation for a given intensity, a gradient in the excitation profile at the saturation limit consequently leads to steep gradients in the population of the ground state and thus the fluorescence. To use this effect in a experiment, it can be confined at the center of a focal spot with a so called doughnut mode. This laser mode consists of a superposition of two transversal electrical modes of order TEM_{0i} with $i \in \{1, 2, 3\}$ relatively rotated to each other [93] [94]. An excitation with this mode leads to a dark spot at the position of our emitter that becomes smaller with increasing excitation intensity as shown in figure 1.7.

The resulting resolution of the position of the emitter is then determined by the FWHM of the dark region Δr inside the bright saturated spot. Assuming a fluorescence wavelength λ and a refractive index n of the environment. The half aperture angle of the microscope can be characterized by the parameter β, which represents the steepness of the central minimum. In case of a non-ideal doughnut beam the minimum intensity in the center ϵ will be higher than zero. Additionally one can define $\zeta = \frac{I_m}{I_S}$, which gives the ratio of the maximal doughnut intensity I_m to the saturation intensity I_S. With all these parameters, one can derive a final resolution of GSD of [95]

$$\Delta r \cong \frac{\lambda}{\beta\pi n}\sqrt{\epsilon + \frac{1}{\zeta}} \; . \tag{1.10}$$

Hence the principal behavior of the resolution shows an $I_m^{-\frac{1}{2}}$ dependency and is theoretically unlimited. Applying this method a resolution below $10\,\mathrm{nm}$ is accessible, e.g. for defect centers in diamond a resolution down to even $7.6\,\mathrm{nm}$ has been reported [16]. In principle, the final resolution is of this technique is not limited. However, due to the requested high intensity for the laser beam, technical limitations (destruction threshold of optical components) and the photostability of fluorophores to bleaching are limiting factors.
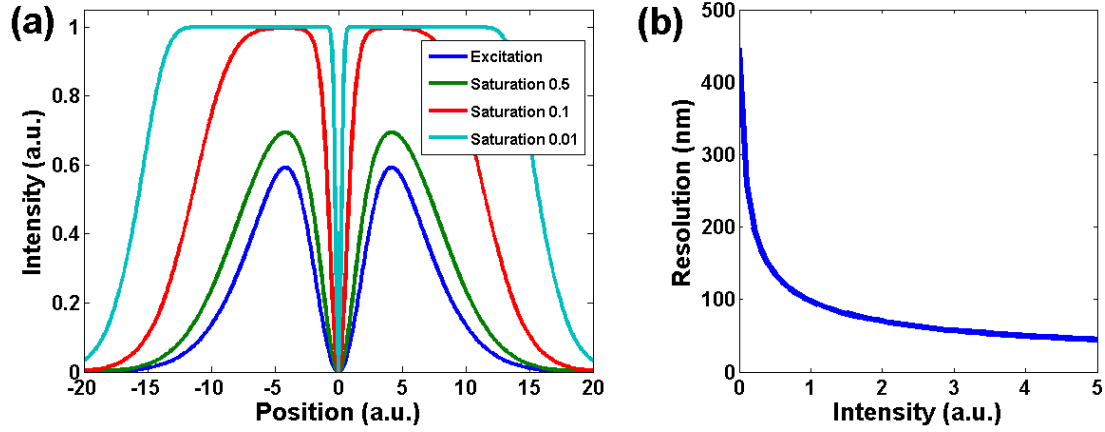
Figure 1.7: **Exemplary GSD excitation and fluorescence.** (a) A system is excited by an ideal doughnut laser mode (blue curve). However the resulting fluorescence profile is dependent on the ratio of the excitation intensity to the saturation. An increase in the intensity lowers the saturation threshold that is exemplary depicted for the green, red and light blue curves. One can clearly see the decreasing width of the central dark spot and the saturated broadening outside the center. Note that in reality the excitation intensity (blue) is higher than stated by the diagram and was virtually scaled down to emphasize the effect on the fluorescence. The numbers given in the key of the graphics refer to the ratio of the saturation intensity to the maximal intensity of the excitation. Thus the smaller numbers indicate a higher excitation intensity. (b) The theoretical resolution of GSD shows a reciprocal square-root behavior with respect to the intensity. Thus the final resolution is not limited by diffraction but by technical limitations like a threshold concerning the destruction of components due to high laser power.

1.2.2 Stimulated Emission Depletion Microscopy (STED)

Though not part of the experiments of this thesis a short description of STED microscopy shall be given for the sake of completeness. STED is closely related to GSD since it uses the same principles with an extra feature. One disadvantage of GSD is that the position of an emitter is characterized by a dark spot instead of an illuminated area. This can be overcome by adding a second excitation laser beam that is resonant with energy level difference between the metastable state and the ground state. Thus all population in the metastable state will be forced to perform stimulated emission and deplete the metastable state [6]. Whereas first realizations relied on pulsed lasing [7], nowadays also continuous wave excitation is common [96] [97].

The effect on the image, as displayed in figure 1.8, is an inversion of the GSD image from light to dark and vice versa. The real position of the emitter is now again given by the bright spot.
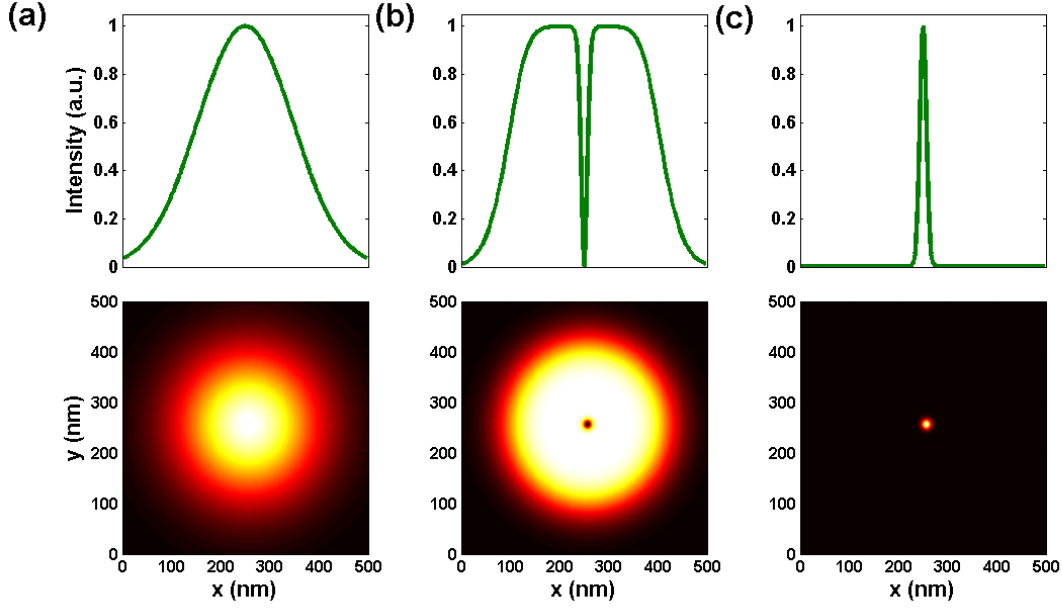
Figure 1.8: **Comparison of different microscopy techniques.** Intensity profile and image of an emitter by (a) confocal microscopy, (b) GSD and (c) STED. Whereas the confocal spot represents the diffraction limited image of the emitter, GSD even broadens the intensity profile. Nevertheless the dark spot in the center enables a resolution of the position in the range of about 20 nanometers. STED inverts the bright center of the GSD profile and successfully suppresses undesirable fluorescence. Since the underlying principle is the same for GSD and STED, both examples show the same resolution. However one can clearly see the advantage of STED, since this technique only enlightens the central spot.

This feature is a powerful tool with a manifold of applications since its resolution is just in the right order of magnitude to watch e.g. proteins or other macromolecules. In combination with a solid immersion lens a resolution of 2.4 nanometers lateral to the optical axis could be confirmed [98]. Though a STED image takes some time to record, first advances have been made towards some kind of real-time imaging with a time-resolution of 200 frames per second [99].

Nevertheless there has to be mentioned one downside of GSD and STED microscopy. As both methods are dependent on a high excitation beam intensity the fluorophores have to be very photostable against bleaching. In certain experiments that possibly limits the range of application. Valuable summaries of both methods in comparison to other superresolution techniques like PALM or STORM can be found in references [100] and [101].

1.3 Fluorescence Imaging with One-Nanometer Accuracy (FIONA)

Instead of using a sophisticated method to squeeze the PSF of our microscope one can take a different path by optimizing the amount of information one derives from an image. This section introduces fluorescence imaging with one-nanometer accuracy (FIONA) [21]. Here the position of an emitter is calculated from the diffraction limited spot with a much higher precision than its full width half maximum. In principle FIONA summarizes a variety of methods, where mathematical models or algorithms help to increase the calculated resolution.

1.3.1 Basic Concept

As stated before, in case of a common microscope a point-like source will be imaged as a diffraction limited spot. In a typical case the PSF will be given by an Airy pattern as the intensity derived from the Fourier transform of a circular aperture (see eq.1.4). For practical purposes this intensity profile is typically approximated as a Gaussian, since there is no notable difference between both functions around the region of interest (that is the maximum of the distribution) [102] [103].

Now, if one assumes that the precise position of the emitter has to be at the maximum of the PSF, the absolute resolution is defined by the ability to determine the position of the maximum. In principle the PSF is considered to be a probability distribution and each collected photon represents the outcome of one measurement. With the standard uncertainty of the PSF denoted as σ, the achieved resolution δx for N detected photons will be

$$\delta x = \frac{\sigma}{\sqrt{N}} \ . \tag{1.11}$$

This leads to a theoretically unlimited resolution if one is able to detect enough photons. Note that the acronym of FIONA technically is not correct, since the calculation increases the precision but not necessarily the accuracy of the localization measurement [104].

1.3.2 Noise and Uncertainty

Unlimited precision respectively accuracy will not be achieved if one believes in Heisenberg's principle of uncertainty. However - in most cases - much larger sources of error exist than the measurement accuracy on a quantum level. First, the emission of photons has to be taken into account. Photon emission is a process that due to its nature underlies Poissonian statistics [105]. Thus, there will always be photon shot noise that scales with an uncertainty of $\sqrt{N}$ where N is the total number of photons. Second, in case of finite steps resp. pixels to detect the photons, there will be an intrinsic grain in the measured image. Third imaged samples typically show a certain amount of background fluorescence. Putting all these effects together one arrives at a more general formula

than eq.1.11 [23]:

$$\delta x = \sqrt{\frac{\sigma^2}{\sqrt{N}} + \frac{a^2}{12N} + \frac{8\pi\sigma^4 b^2}{a^2 N}} \ , \tag{1.12}$$

where a denotes the pixel size and b the background noise. If one assumes shot noise to be the dominating source of uncertainty compared to other factors, equation 1.11 still holds for the behavior of the measured accuracy. Figure 1.9 illustrates the resolving power of FIONA. As it can be seen, even in case of relatively high fluctuations, the region of uncertainty to localize an exemplary emitter is much smaller than the FWHM of the distribution.
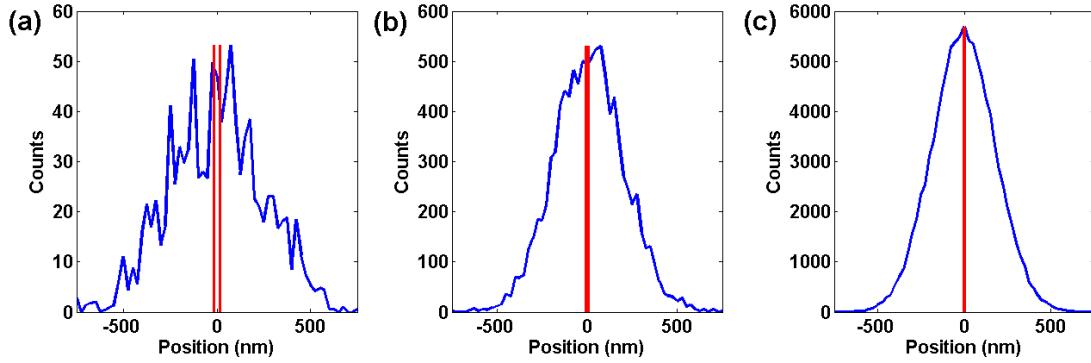

Figure 1.9: **Resolution of FIONA.** The figure exemplarily shows PSFs of an emitter with a number of (a) 1000, (b) 10000 and (c) 100000 collected photons. The red lines indicate the uncertainty of the maximum position of a fitted Gaussian function to the measurement data. Even with only 1000 counted photons the precision to determine the position of the emitter is only 16 nm and therefore much better than the FWHM of 500 nm of the PSF. In case of (c), the precision drops below 2 nm and scales down the theoretical resolution by a factor of more than 250 compared to the diffraction limit. However these figures neglect any background noise. Thus the real precision would be slightly worse, according to equation 1.12.

Nevertheless, in the end there will always be a limit that is mainly defined by the signal-to-noise-ratio of the experiment [102]. Next to systematic errors that arise from an imperfect measurement apparatus or calibration, there is also a spatial drift to consider. This leads to a relative movement of the detector to the PSF and will smear out the real position of the emitter. Depending on the extent of this drift the measurement time and therefore the achievable number of collected photons is limited and no more improvement of the accuracy can be expected.

1.3.3 Resolution Parallel to the Optical Axis

So far this section covered the basic ideas of FIONA. A variety of experiments have been performed using this concept to increase the accuracy of localization. Most of them were applied in the field of bio-imaging to localize fluorophores in an environment of more or less homogeneous optical density. In case of two-dimensional imaging sub-nanometer resolution has been confirmed [25].

Since three-dimensional imaging and tracking is an important task for many investigations in this field, several approaches have also dealt with the increase of the resolution along the optical axis. Theoretical treatises have investigated the effect of confocal imaging along the optical axis [106] as well as numerous experiments that used the imaging of multiple z-slices for axial resolution [27] of moving particles [107] [108] [109]. All in all, the basic application of the FIONA principle has been confirmed down to a three-dimensional accuracy in the order of 10 nm. Other techniques additionally use astigmatic effects to break the axial symmetry of the imaging system. These methods validate resolvable distances from 40 nm [110] down to 12 nm [111].

Valuable information can also be gained from defocused imaging. A confocal microscope with a combination of a charge coupled device (CCD) and an avalanche photodiode (APD) shows a fitted precision of 50 nm [112]. Even better results are made in the investigation of the diffraction patterns of small beads along the optical axis in a homogeneous environment. Using the size of off-focus interference rings, an axial resolution in the range of few nanometers is confirmed [113]. The order of magnitude of this resolution can also be accomplished by a fit to a three-dimensional PSF [114] as well as by splitting the image to relate the depth to the parallax [115].

In this thesis FIONA was applied to depth measurements of NV centers in diamond. The localization along the optical axis in addition to the refractive effect of the diamond surface issued a special challenge to achieve satisfying results. The approach to a proper application to the measurements that was developed during the experiments therefore is presented in chapter 5 right before the experimental results that have been published in [30].

2 – THE NV CENTER IN DIAMOND

This chapter covers the properties of the Nitrogen-vacancy center in diamond which was used for all the experiments presented in this thesis. After a description of its basic physical characteristics the quantum mechanical spin dynamics of the system will be treated as well as its experimental application to magnetometry.

2.1 Properties of the Nitrogen-Vacancy-Center in Diamond

The Nitrogen-Vacancy center is a color center in diamond, that was first reported in 1976 [116]. Since then manifold research has been performed to learn about the structure and qualities of this defect, from which some still wait to fully unravel their mysteries [40]. This section describes the basic properties of the NV center.
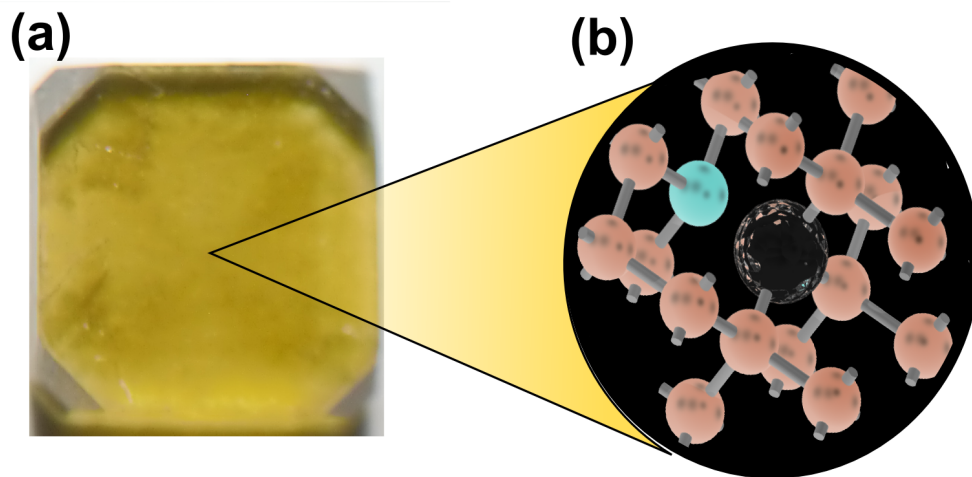

Figure 2.1: **The NV defect in diamond.** (a) The yellow color of the diamond indicates a high concentration of Nitrogen impurities. (b) A Nitrogen atom (blue) occasionally is placed right beside a vacancy (indicated dark sphere) in the lattice of Carbon atoms (red). This defect positioning is a remarkable stable configuration that can be treated as an atom-like system in the diamond lattice. Typically an additional electron is a attracted to the excess single electron of the Nitrogen that puts the center in a negative charge state.

2.1.1 Structure and Fabrication

The NV center in diamond is a lattice effect that consists of a Nitrogen atom and a neighboring vacancy which replace two Carbon atoms within the diamond lattice as shown in figure 2.1. Due to the fcc structure of the diamond lattice with two basic atoms, the defect shows a C_{3v} symmetry along its axis and can occur in four different directions in a random sample.

NV centers form a stable entity in the lattice and can be found in natural diamonds since Nitrogen impurities are the major defects in these gems. Since most of the properties of the NV center are very sensitive to the environment such as fluctuations of fields or irregularities in the lattice the NV centers commonly used in science are artificially created in factory-made diamond. Two different techniques are used for the creation of these ultrapure diamonds. One is the simulation of the natural creation process by the use of a high pressure and high temperature environment (HPHT) [117] [118]. Another possibility is chemical vapor deposition (CVD) in which a hydrocarbon gas will be floated in a pressure chamber and adsorb on a substrate to form one diamond layer after another [119] [120]. Both methods allow the creation of high quality diamonds with no practical impurity.

To bring NV centers into the diamonds, Nitrogen ions can be shot onto the sample. Typically a small percentage of Nitrogen atoms are able to replace Carbon atoms in the lattice. To increase the number of vacancies the sample can be exposed to high energy electron irradiation that create a distribution of vacancies in the lattice. By annealing the diamond at about $700\,°C$ the vacancies are able to migrate through the lattice until they arrive at a stable position next to a Nitrogen atom [121] [122]. Another method is called δ-doping where CVD-gas is enriched by N_2 gas during the process. Such technique enables the creation of thin layers of a high density of NV centers [123] [124].

2.1.2 Energy Scheme of the NV⁻-Center

The Nitrogen-Vacancy center exists in two stable charge states, the neutral state NV^0 and the negatively charged state NV^- [125]. They can be distinguished by their different zero phonon lines (ZPL) of $575\,nm$ for NV^0 [126] and $637\,nm$ for NV^- [127]. The neutral charged NV^0 consists of five electrons that are not part of a covalent bond to one of the neighboring carbon atoms with one unpaired electron. In case of the NV^-, the additional electron will cause the formation of two unpaired electrons with a resulting quantum number of $m_S \in \{-1; 0; +1\}$ for the angular momentum of the spin. Contrary to the doublet system of the NV^0, this triplet configuration enables several important experiments based on its spin dynamics. A view to this will be described in section 2.1.4. Since the experiments in chapter 7 deal with the application of this spin dynamics and the NV^- state is the prevailing state of the NV center, the NV^- will be just denoted as NV center without any further distinction.

Figure 2.2 depicts the energy level scheme of the NV center. Assuming no interaction to any perturbation the ground state of the system is separated in one parallel and one anti-parallel state of the total sum of the electron spins with a separation of $2.88\,GHz$

[128]. When excited to a higher energy level by light the spin will not be affected due to conservation of angular momentum. The decay back to the ground state is dependent on the spin state. For bulk diamond lifetimes of $12.0\,\text{ns}$ for $m_S = 0$ and $7.8\,\text{ns}$ for $m_S = \pm 1$ have been measured [129]. This difference originates in the possibility of spin-dependent intersystem crossing, since two possible decays exist back to the ground state: First the system stays in the triplet state and emits a photon to get back to the low energy level. Second there is intersystem crossing to a singlet state. For $m_S = 0$ there is only a very small probability for the crossing, however in case of $m_S = \pm 1$ one can measure a crossing rate of 30%. In the singlet state the energy decays on a longer timescale via a metastable state with a lifetime of about $250\,\text{ns}$ [130]. Since the system decaying from the singlet will likely end up in the $m_S = 0$ state, it is possible to polarize the NV center into the $m_S = 0$ state by successive cycles of optical excitation [48].
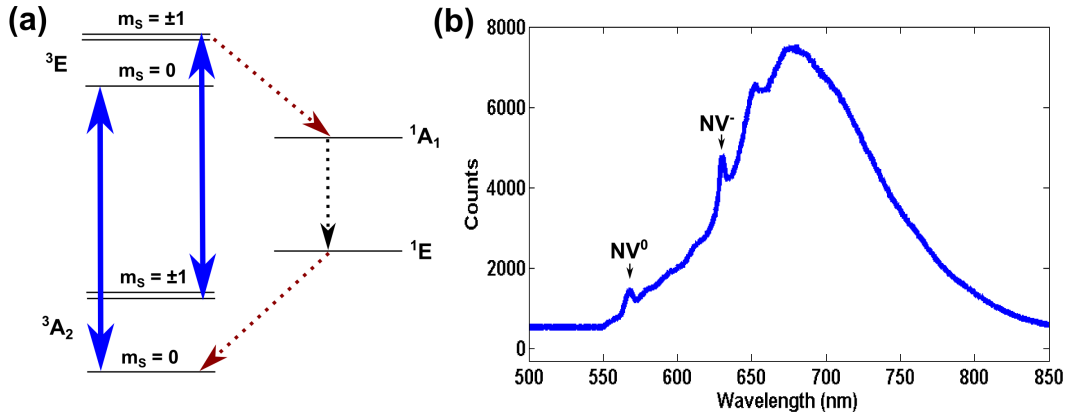

Figure 2.2: **Energy levels of the NV$^-$ center and spectrum.** (a) The basic energy scheme of the NV$^-$ center consists of a triplet ground state ^{3}A$_2$, a triplet excited state ^{3}E and a collective singlet dark state of energy levels. The picture shows the optical transitions (blue) and strong transitions of intersystem crossing (dashed red) as well as the decay in the dark state (dashed black). Other weak transitions (e.g. from the ^{1}E dark state to the $m_S = \pm 1$ ground state) are possible but neglected for our depiction. (b) The measured spectrum of the NV center shows a broad phonon sideband in the infrared. The zero phonon lines of the NV^0 and NV$^-$ state are clearly visible.

Figure 2.2 also shows the fluorescence spectrum of the NV center. A total amount of 4% of the photons is emitted at the peak of the zero phonon line (ZPL) at $637\,\text{nm}$ that is clearly visible even under ambient conditions. This ratio can be significantly increased by coupling the NV center to a resonator like a cavity [131]. The ZPL is followed by a broad phonon sideband with a width of about $120\,\text{nm}$ and a maximum at around $680\,\text{nm}$.

The different fluorescence of the $m_S = 0$ and $m_S = \pm 1$ spin states up to 30% [132] enable optical detection of magnetic resonance (ODMR) of the NV center [133] [46]:

Microwaves of varying frequencies interact with the NV center, that is polarized to the bright state. In case the frequency matches a resonant transition the NV center will be eventually transfered to the dark state and a drop of intensity will be measured. The resulting spectrum is shown in figure 2.3. In case of an apparent magnetic field parallel to the NV axis B, the $m_S = \pm 1$ state will split up due to the Zeeman effect by a frequency of $2\gamma_e B$ with the gyromagnetic ratio of the electron γ_e. The $m_S = -1$ level of the ground state will decrease for higher fields until it matches the $m_S = 0$ state at about $103\,\mathrm{mT}$. Here, level-anti-crossing of the two states can be observed in presence of small field perturbations [134], an effect that has also been studied for the excited state at around $50\,\mathrm{mT}$. The difference of the two values is due to a different zero-field splitting, that is $1.42\,\mathrm{GHz}$ for the excited state [135].
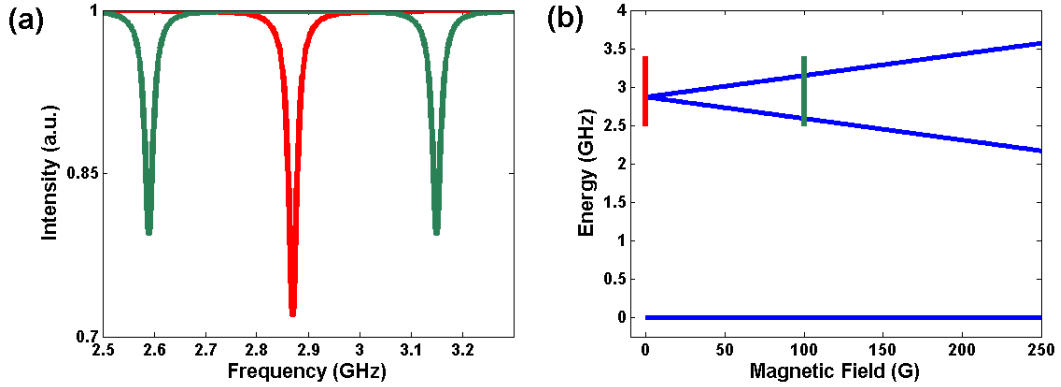

Figure 2.3: **Optically detected magnetic resonance (ODMR).** (a) Microwaves in the frequency range of $2.5\,\mathrm{GHz}$ to $3.3\,\mathrm{GHz}$ interact with a NV center at absent magnetic field (red) and at 100 Gauss (green). Due to differing fluorescence intensity of the spin states a dip is observed when the microwaves are in resonance with the gap between the energy levels. (b) The Zeeman effect splits up the $m_S = \pm 1$ state and enables the experimental determination of the magnetic field by ODMR.

2.1.3 Single Photon Source

The characteristics of light sources can be examined by their photon emission behavior. The underlying Poissonian statistics of light origin imply a correlation in the emission times of individual photons. Hanbury-Brown and Twiss used an interferometer in which incoming light passed a 50:50 beam splitter and was separated into two detection channels. A positive temporal correlation, that is called bunching, was shown [136] [137]. This effect can be explained quantum-mechanically by calculating the emission of two uncorrelated light sources, which show a constructive interference [138].

One can compare the photon arrival times in both detectors by the second order autocorrelation function $g^{(2)}$ which depends on the intensities I at a certain time t and a

delayed time $t + \tau$:

$$g^{(2)} = \frac{\langle I(t) \cdot I(t + \tau) \rangle}{\langle I(t) \rangle^2} \; . \tag{2.1}$$

For a classical light source, this function will show a value of $g^{(2)}(\tau) > 1$ respectively $g^{(2)}(\tau) = 1$ in case of perfectly coherent light. However if one imagines a single quantum system like the NV center, a correlation of $g^{(2)}(0) < 1$ is to be expected [139] [140]. After emitting one photon the system will have to be re-excited again to emit a subsequent photon. Thus there will be a delay in the emission between two photons, that can be measured as a drop in the autocorrelation function. Therefore the NV center is a single photon source.

Figure 2.4 shows an exemplary measurement of a single photon source. In an ideal case the $g^{(2)}$ function would drop to 0, in reality one observes higher value due to background fluorescence. If the dip stays below 50% a single photon source is confirmed. The antibunching measurement can be used to confirm single NV centers (respectively a pair of NV centers) that cannot be optically resolved by a confocal microscope image.
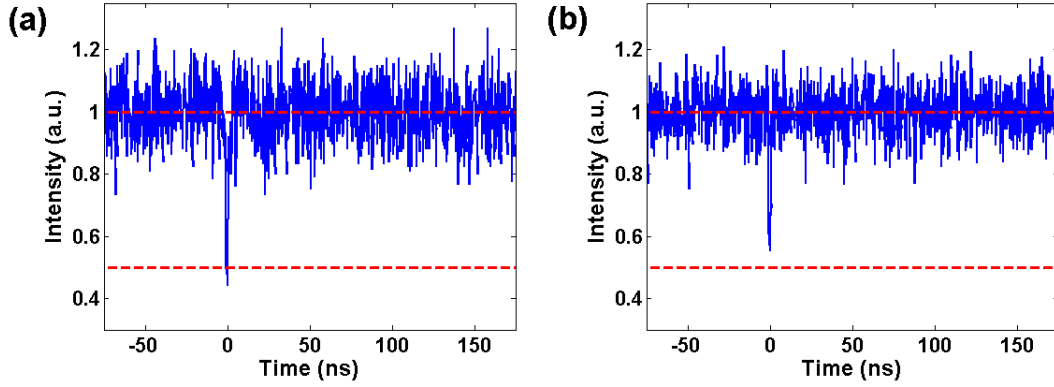

Figure 2.4: **Photon anti-bunching.** (a) In the experiment a dip below 50 % of the normalized intensity in the autocorrelation function confirms a single photon source. (b) If there are 2 emitters in one diffraction limited spot, the $g^{(2)}$ correlation function still shows antibunching, however the effect is weaker than in case of a single emitter with $\left(1 - \frac{1}{2}\right) < g^{(2)}(0) < \left(1 - \frac{1}{3}\right)$ and decreases for every additional emitter.

2.1.4 Spin Dynamics and Coherence

As previously stated the spin state m_S of the ground state can be experimentally distinguished by the brightness of fluorescence. Thus it becomes convenient to use the bright state $|0\rangle$ and one dark state $|\pm1\rangle$ as an atom-like two-level system according to the Jaynes-Cummings model [141]. Hence the Hamiltonian $\hat{H}$ of the spin $\vec{S}$ of a NV center

in the Ground State in an external magnetic field $\vec{B}$ can be stated as [142]

$$\hat{H} = D_{gs}\left(S_z^2 - \frac{1}{3}\left[S\left(S+1\right)\right]\right) + E\left(S_x^2 + S_y^2\right) + g\mu_B\vec{B}\cdot\vec{S} \tag{2.2}$$

with the zero field splitting of the ground state $D_{gs} = 2.88\,\text{GHz}$ and the strain E caused by symmetry breaking of the C_{3V} symmetry. $g \approx 2$ represents the Landé g-factor of the electron and μ_B the Bohr magneton. Depending on the environment other terms like an external electric field, other fluctuating fields or nuclear spin interaction can be added to the Hamiltonian. Typically, either the state $|+1\rangle$ or the state $|-1\rangle$ is chosen to create a two-level-subspace of the system together with the state $|0\rangle$. The state of the NV center $|\psi\rangle$ is then given by the linear combination

$$|\psi\rangle = \alpha\,|0\rangle + \beta\,|\pm1\rangle \tag{2.3}$$

with the population ratios defined by α and β under the constraint $\alpha^2 + \beta^2 = 1$. In this picture the dynamics of the spin in this two-level system can be illustrated by the Bloch sphere as depicted in figure 2.5 [143]. The Bloch sphere is intuitively accessible to describe the dynamics of the quantum state. The population of the states is given by the projection of the spin vector onto the z-axis, while superposition of both states is then referring to the xy-plane with $\alpha = \beta = 1/\sqrt{2}$.
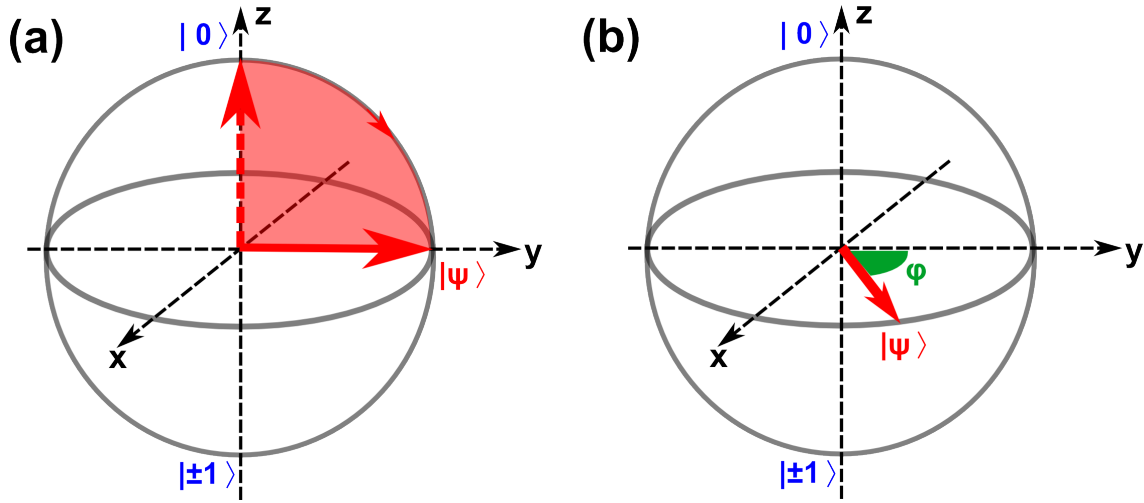

Figure 2.5: **Bloch sphere representation of the ground state.** The population of the bright state $|0\rangle$ and the dark state $|1\rangle$ is given by the projection of the vector $|\psi\rangle$ onto the z-axis. (a) The system is rotated by a $\frac{\pi}{2}$ flip around the x axis and thus brought into the superposition state. (b) In the superposition state the spin will precess in the external magnetic field according to its Larmor frequency. Thus a phase ϕ is collected. In case of perturbations the state vector $|\psi\rangle$ shortens due to decoherence, representing the dissipation of information.

One basic feature of the spin system is its coherence. This can be thought of the time-dependent stability of one state before dissipating. It is defined by the contrast between the bright state (respectively the dark state) and the equilibrium state. The coherence time is then defined as the time when the measured contrast drops below a value of $1/e$ of the initial intensity difference. Note that this definition is quite similar to the definition of coherence of light in optics, where the contrast is given by phase differences of different wave packages.

The decoherence effects of the environment can be separated in two parts: longitudinal and transversal relaxation. Longitudinal relaxation refers to a change of the state population towards the equilibrium. In the Bloch sphere representation this can be described as a combination of rotation around the x- or y-axis where the absolute value of z decreases. Physically this process is connected to energy dissipation from the excited spin system into the lattice. Thus this coherence time T_1 is also referred to as spin-lattice relaxation time or more generally lifetime of the spin state. For experimental applications this basic lifetime of a state is the absolute limit. It can be determined by an experiment as shown in figure 2.6. After initialization of the system into a defined state one observes the subsequent decay. NV centers in bulk diamonds typically show T_1 times of the electron spin on the timescale of several milliseconds at room temperature [144], whereas this time increases to timescale of seconds for low-temperature conditions [48].
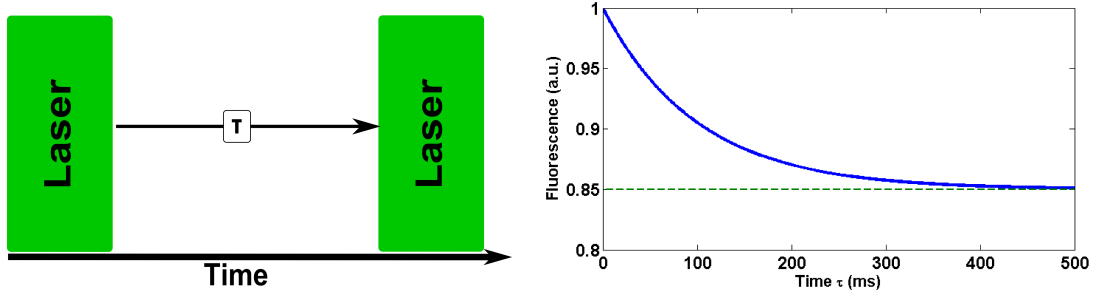

Figure 2.6: **Lifetime measurement.** A laser pulse initializes the NV center to the $m_S = 0$ state. After a varying waiting time τ the state is optically read out. Several repetitions of this sequence determine the state probabilities, that show a decay of the coherence as depicted in the graphics.

As seen, the T_1 time characterizes the coherence of the spin state parallel to the z-axis. In contrast to that the perpendicular dissipation of the state is characterized by the T_2 time respectively the T_2^* time. Cause of this decoherence process is an interaction to the environment, e.g. by fluctuating fields that slightly shift the energy levels of the system. One can separate inhomogeneous and homogeneous dephasing by two experiments. To determine inhomogeneous effects, one can measure the free induction decay (FID) in a so called Ramsey experiment that measures T_2^*. Here the spin state is rotated into the xy-plane and freely evolves to all fluctuations and random quasi-static perturbations.

Since the measurement is performed several times and the quasi-static perturbation randomly changes between these runs, this will lead to decoherence. In contrast to that, the Hahn echo sequence applies an additional π-pulse in the middle of the sequence. This reverses the spin state in the xy-axis and will lead to an inversion of any quasi-static fluctuations. Thus this sequence refocuses the state and measures only the homogeneous dephasing that is characterized by the coherence time T_2. Both sequences are illustrated in figure 2.7.
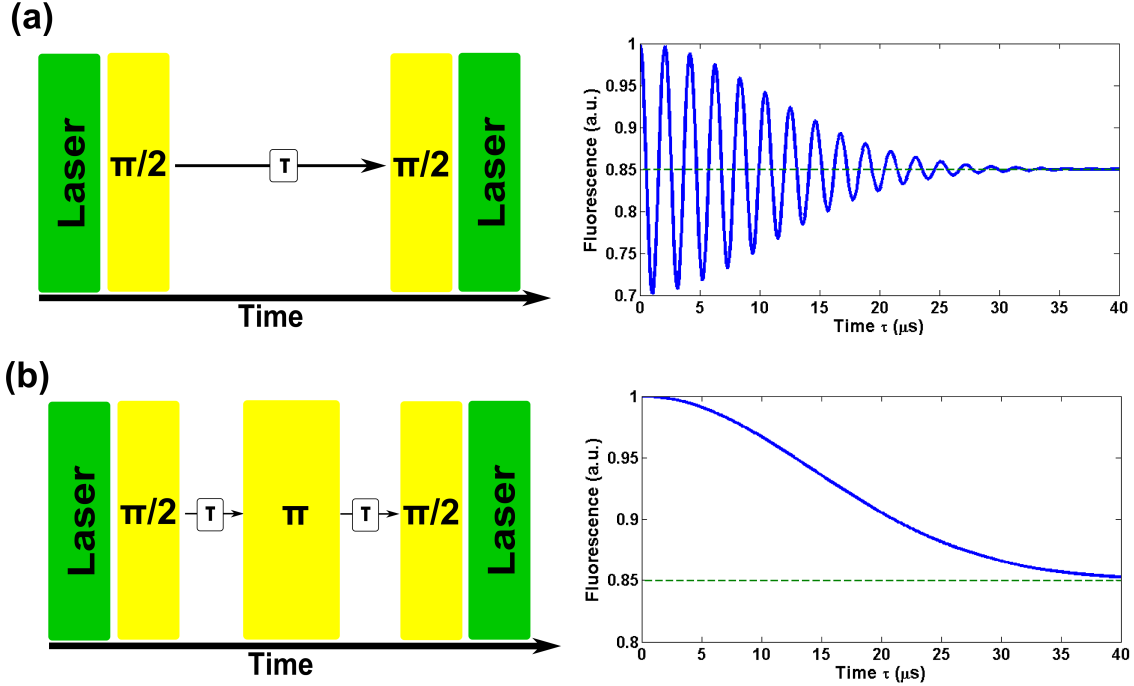
Figure 2.7: **Transversal spin relaxation measurements.** The dephasing of the spin state can be separated into a homogeneous and an inhomogeneous part. The yellow areas depict microwave pulses rotating the spin on the Bloch sphere. (a) Inhomogeneous dephasing is measured by the Ramsey sequence: The $\frac{\pi}{2}$-pulse rotates the spin state into the xy-plane. The spin precesses around the z-axis, while slightly dephasing, as it is shown by the enveloped decay of the oscillation, that gives the T_2^* time. (b) By applying an additional π-pulse in the middle of the sequence, the quasi-static dephasing is reversed and the spin shows the so called Hahn echo. Since some dephasing effects are cancelled, the T_2 coherence time given by the decay is typically longer than T_2^*.

The interaction of NV centers is typically connected to nuclear spins of ^{13}C, as was confirmed for ensembles of NVs [145] as well as for single centers [146] and can be theoretically modeled by cluster-expansion methods [147]. Typical T_2 times of NV centers occur on the timescale of μs, however a coherence time up to 1.8 ms has been measured,

that is the longest coherence time of an electronic spin ever observed [47]. In general, the dephasing times are highly dependent on spin-spin-interactions to impurities, such as nuclear spins of nitrogen in diamonds of type Ib [148] [149] and ^{13}C in type IIa [150] [151]. Furthermore, disturbances from outside the diamond will effect the coherence as well. As a consequence, the average coherence time of NV centers will decrease for a shorter distance to the surface [152] [153].

Up to now this section covered the interaction of the spin with the environment that limits the total measurement time. However it is not only possible but necessary for many applications like quantum information processing (QIP) to control the spin state and bring it in a determined position on the Bloch sphere. One basic experiment to demonstrate this is the so called Rabi oscillation. An oscillating field (e.g. a microwave) interacts with the spin and will cause a rotation on the Bloch sphere as illustrated in figure 2.8.
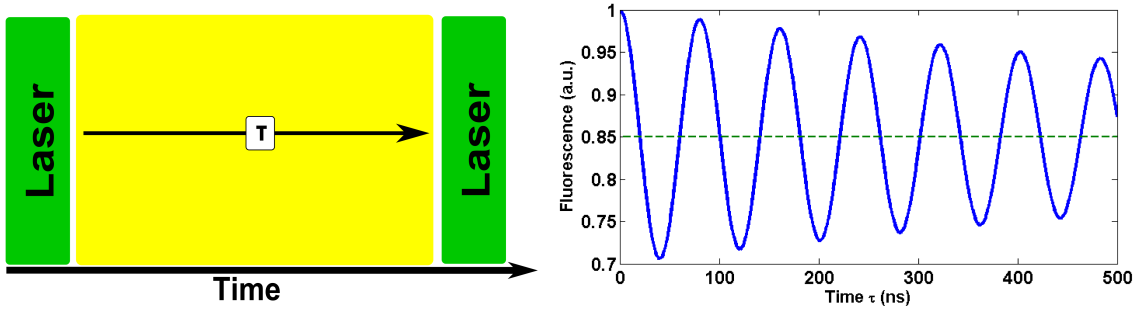

Figure 2.8: **Rabi oscillation.** A microwave field with a frequency resonant to the energy level gap of the ground state drives the population between both states. The observed Rabi frequency is effectively depending on the field strength e.g. the driving power. Due to dephasing, the T_2 time limits the application of Rabi oscillation as is suggested in the slow decay of the amplitude.

The rotation frequency Ω_{Rabi} between the states $\mid 0\rangle$ and $\mid \pm 1\rangle$ is determined by the Hamiltonian

$$\hat{H} = -\vec{\mu} \cdot \vec{B} \tag{2.4}$$

with the magnetic moment of the NV center $\vec{\mu}$ and the amplitude of the driving magnetic field $\vec{B}$.

As it can be seen, the Rabi oscillation is a simple possibility to shift populations between the two states. Note, that for strong driving fields the spin dynamics become highly anharmonic since the rotating fields interact with the spin on the same timescale as the Larmor precession. Nevertheless, this effect can be exploited to achieve sub-nanoseconds spin-flips that have been experimentally shown in strong driving regime. Hence, for NV centers at room temperature with their long coherence times, a number of about 10^6 Rabi cycles is possible [154]. So far the described experiments were always

limited by the coherence time of the NV electron spin, namely the T_2 time, that is highly dependent on the interaction with the environment. However, there have been great advances in pushing this limit by manipulating the coupling strength of these interactions (dynamical decoupling [155] [156]). With these sequences the influence of environmental fluctuations can be minimized. Other algorithms are able to calculate the optimal movement of the spin vector on the Bloch sphere under environmental constraints (optimal control [157] [158]). Section 2.2.3 will present one of such advanced sequences to measure magnetic field fluctuations.

2.2 Magnetometry with the NV Center

The last part of the performed experiments deals with magnetic sensing of spins by single NV centers. Thus this section highlights the state-of-the-art techniques for magnetic field measurements and explains the application of NV centers.

2.2.1 NV Centers as Magnetic Sensors

The measurements of weak magnetic fields on the scale of nT is an important challenge in physics as well as in life-sciences [75] [159] [160]. A variety of developments has been achieved in techniques for measuring magnetic fields and magnetic imaging. One famous example is the application of a Josephson junction in a superconducting quantum interference device (SQUID) [161] [162], others are Hall sensors [163] [164] and the combination of atomic force microscopy to a magnetic sensor in magnetic resonance force microscopy (MRFM) [75]. Typically one can compare their sensitivity to the scaling of the distance between sensor and sample as shown in figure 2.9.

When comparing different methods one has to consider that not every technique can be applied to any issue since some methods require e.g. cryogenic temperatures or vacuum [167]. Since NV centers have proven their diversity of usage, they are certainly the most promising candidate for further advances in magnetic sensing. Their sensitivity is crucially dependent on the coherence time of the system T_2 and the measurement time τ. The smallest field to be detected δB_{min} is then given by [61]

$$\delta B_{min} = \frac{1}{g\mu_B} \frac{\hbar}{\sqrt{\tau \cdot T_2}} \qquad (2.5)$$

As the accuracy of the measurement scales with $\tau^{-1/2}$, the unit to compare different methods is given by $\sqrt{Hz}$. Note that the dependence of the sensitivity on measurement time is similar to the one already stated in section 1.3, where the number of collected photons was proportional to the measurement time.

So far NV magnetometry has accomplished manifold progress. Magnetic fields in living cells [69] [168] and neural networks [169] have been investigated as well as atomic spins in metallo-proteins [170] and lipid bilayers [171]. Also the nanoscale formation and properties of magnetic vortices and domains in ferromagnets [172] [173] and superconductors [174] are penetrable by NV technology.
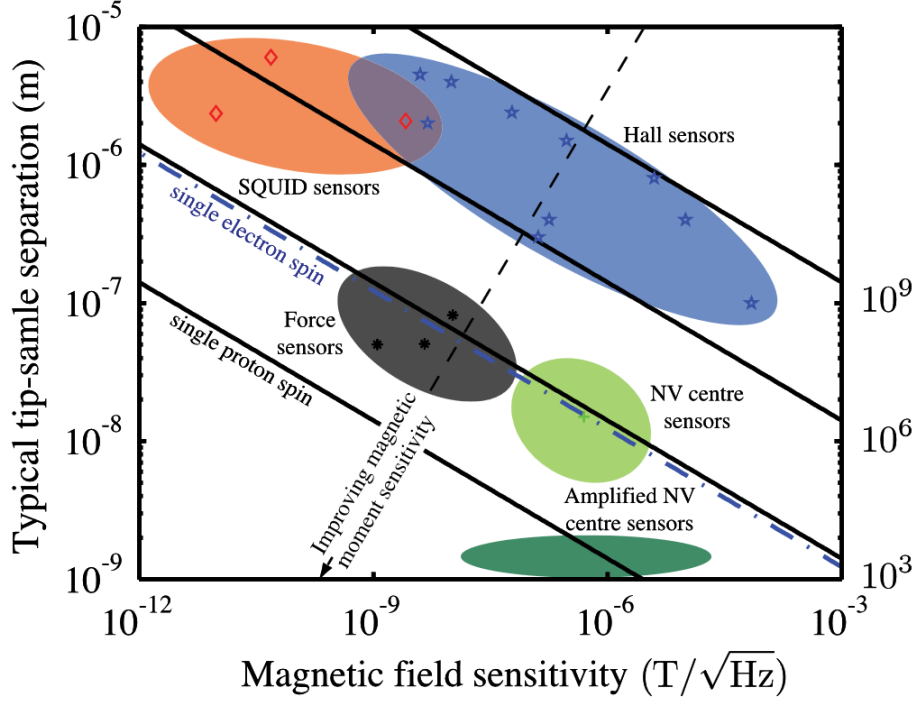
Figure 2.9: **Performance of magnetic sensors.** The diagram compares the sensitivity of different magnetometer types to their typical achieved probe-sample-separation. The diagonal lines (solid black) show the boundaries for the detection of 1, 10^3, 10^6 and 10^9 single proton spins as well as one single electron spin (dashed blue) in a measurement time of 1 s. The suggested technique of preamplified NV sensors [165] predicts a capability to cross the single proton spin line. (Picture taken from [165], adapted from [166])

The measurements of single electron spins has been achieved [72] and even further progress is to be awaited. Recently the successful measurement of a single proton spin has been claimed [175], however the paper was retracted due to uncertainties of perturbation of the measurements by ^{13}C nuclear spins. Nevertheless one reported event still seems to confirm a single proton spin [176]. All the same this shows the potential of NV centers as magnetometers. The next section explains the basic procedure of NV magnetometry.

2.2.2 DC and AC Field Measurements

As described in section 2.1.4 the coherence time of NV centers is dependent on fluctuations of the magnetic field environment. This can be exploited to detect small constant fields (DC fields) and fields of a certain frequency (AC fields) with measurement protocols that have been shown in figure 2.7 [61] [56].

A constant field will affect the NV center in a small Zeeman shift of the energy levels. If the NV center is in the superposition state of $1/\sqrt{2}\,(|\,0\rangle + |\,1\rangle)$ the spin accumulates a phase proportional to the external field B_{DC} and the free evolution time τ. Thus a readout with a Ramsey-experiment will measure this accumulation with a total sensitivity η_{DC} of [61]

$$\eta_{DC} \approx \frac{\hbar}{g\mu_B\sqrt{\eta_d c \cdot T_2^*}} \; , \; (\tau \sim T_2^*) \tag{2.6}$$

where η_d is the collection efficiency of about $2 - 3\%$ [177] and c the contrast in the Ramsey measurement.

In case of an external field of a certain frequency ν one wants to get rid of any constant field effects in the measurements. This is achieved by the Hahn echo sequence [56]. Another benefit is that slow noise effects will also partially be diminished. Here the sensitivity η_{DC} scales similar to equation 2.6 by [61]

$$\eta_{AC} \approx \frac{\pi\hbar}{2g\mu_B\sqrt{\eta_d c \cdot T_2}}. \tag{2.7}$$

Both methods have been successfully applied to the detection of weak magnetic fields. Experiments have confirmed a high sensitivity that is only limited by the coherence time down to the scale of $0.5\,\mu\text{T}/\sqrt{\text{Hz}}$ [56] to $4\,\text{nT}/\sqrt{\text{Hz}}$ [47]. Furthermore this sensitivity can be used to not only measure the magnetic field but for localization in magnetic resonance imaging (MRI) with sensitivities in the order of $10\,\mu\text{T}/\sqrt{\text{Hz}}$ for DC fields and $60\,\text{nT}/\sqrt{\text{Hz}}$ for AC fields [73]. Single NV centers can be imagined with high resolution [72] as well as electron spins, that have been localized with a resolution in the range of one nanometer [178].

2.2.3 Noise Spectroscopy

NV centers will be typically affected by field fluctuations with a variety of different frequencies instead of constant magnetic fields or defined alternating fields. This process creates a magnetic noise that influences the coherence of the NV states.

This noise can be characterized and measured by a series of complex pulse sequences. The principle of these sequences is always the same: they decouple the NV center to most fluctuations of the environment and leave only the interaction to a defined window of frequencies. One example is the Carr-Purcell-Meiboom-Gill (CPMG) sequence, that is represented by a Hahn echo like sequence with a multiple number of π-flips to refocus the spin state [179] [180] [181].

A slight variation of CPMG is the XY8-K sequence [182]. The measurement principle works as follows: The NV center is brought in the superposition state by a $\frac{\pi}{2}$-pulse. After that a series of alternating π-flips around the x-axis and the y-axis is applied with a waiting time τ between each flip. The overall effect is suppression of all field fluctuations except the ones for that holds $\omega = \frac{\pi}{m\tau}$ with $m \in \{1; 3; 5; ...\}$ that accumulate a phase shift $\Delta\varphi$ [63] [181] [183]. The sequence is illustrated in figure 2.10.
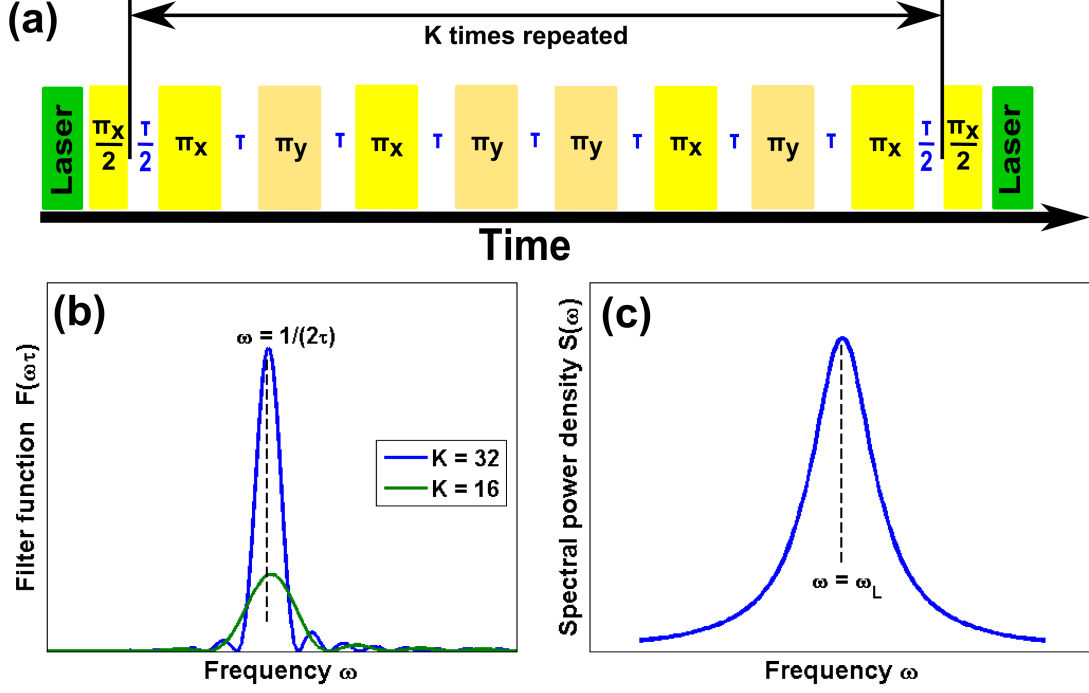
Figure 2.10: **XY8-K decoupling sequence.** (a) After rotating the state to the xy-plane, a series of π-pulses refocuses the spin state alternately around the x- and the y-axis. The basic sequence is a train of 8 π-pulses, that will be repeated K times. (b) The filter function $F(\omega\tau)$ is sensing only the frequencies at $\frac{1}{2\tau}$. The more often the pulse sequence is repeated, the more effective is the decoupling to other noise. A K time repetition will reduce the linewidth by a factor of $\frac{1}{K}$. (c) The figure shows an exemplary measurement result for the spectral power density $S(\omega)$ where external spins of a Larmor frequency ω_L interact to the NV center.

The application of the sequence eventually prolongates the dephasing time [184]. In the experiment an observable echo decay $W(\tau)$ will be given by an averaged random phase $\langle\Delta\varphi^2\rangle$ by

$$W(\tau) = \exp\left(-\frac{\langle\Delta\varphi^2\rangle}{2}\right) = \exp\left(-\chi(\tau)\right) \tag{2.8}$$

with the time evolution decoherence process $\chi(\tau)$ given by

$$\chi(\tau) = \gamma^2 \int_0^\infty \frac{S(\omega)F(\omega\tau)}{\pi\omega^2}\mathrm{d}\omega. \tag{2.9}$$

Here $S(\omega)$ represents the spectral power density of the magnetic field

$$S(\omega) = \int\limits_{-\infty}^{\infty} \langle B(t) B(0) \rangle e^{i\omega t} \mathrm{d}t \tag{2.10}$$

and $F(\omega\tau)$ the filter function of the XY8-K-sequence [184]

$$F(\omega\tau) = 8 \sin^4\left(\frac{\omega\tau}{4}\right) \sin^2\left(\frac{\omega K\tau}{2}\right) \cos^{-2}\left(\frac{\omega\tau}{2}\right). \tag{2.11}$$

In case of high orders K this filter function can be approximated as a stepwise discrete function with a linewidth of $\Delta\omega \approx \frac{2\pi}{K\tau}$.

Recent works have shown the promising sensitivity of this method to investigate magnetic environments by the measurement of the noise spectrum interacting with shallow implanted NV centers. Additionally to an interaction to surface electronic spins in the low frequency regime, faster fluctuations could be related to a surface-modified phonon coupling [181]. Other studies proved the sensing of a number of randomly polarized spins as low as 100 in a $5\,\mathrm{nm}^3$ detection volume under ambient conditions [63]. Moreover, since the calculated frequencies can be related to defined Larmor frequencies in a given magnetic field, it is possible to identify certain species of spins. In principle, this is possible for the sensing of nuclear spins (e.g. of ^{1}H or ^{13}C) as well as for the sensing of electron spins (e.g. free radicals). In this thesis, chapter 7 will present the application of XY8-K to proton spin sensing. As will be shown, one can then determine the depths of shallow NV centers based on these results.

3 – EXPERIMENTAL SETUP

This chapter presents the setup configuration for the experiments that are discussed in this thesis. The first section sketches the basic confocal microscope and optical components whereas the second section shows additional parts, that have been used in the spectroscopy experiments in chapter 7.

3.1 Confocal Microscopy

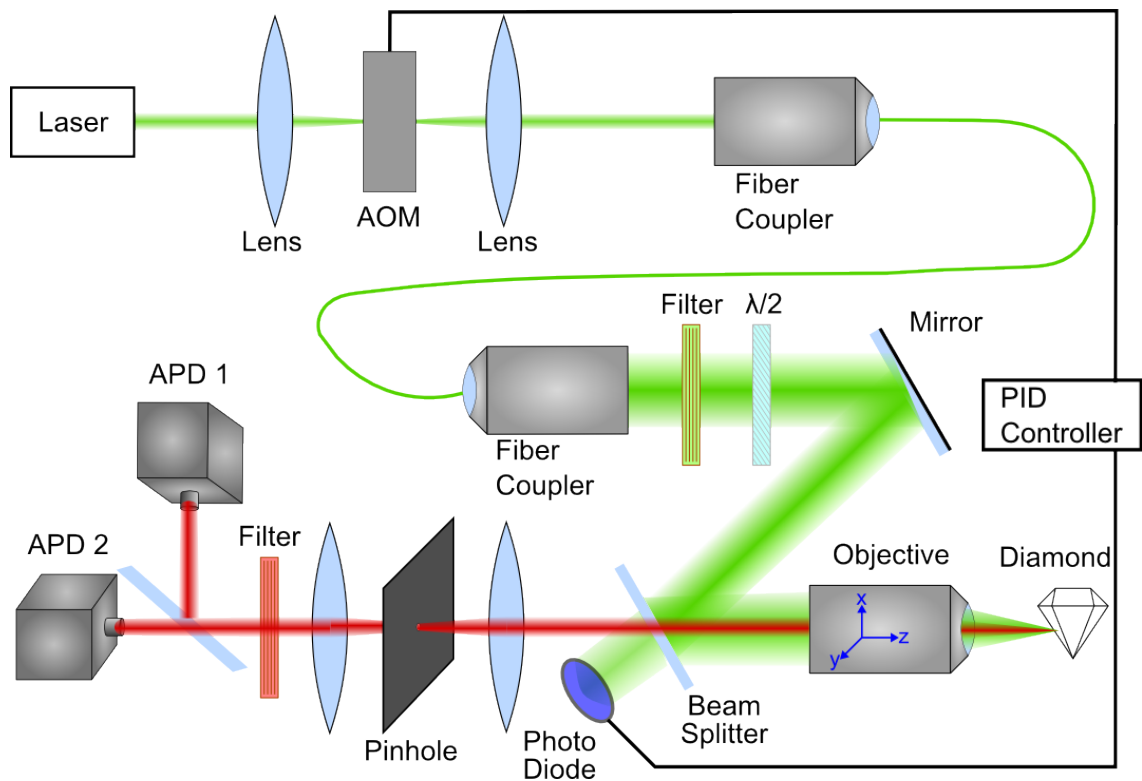The basic setup of the confocal microscope is illustrated in figure 3.1.

Figure 3.1: **Confocal Microscope.** The Gaussian mode of the green laser is guided to the objective, which is used for both excitation and detection of the emitters. The beam splitter is transparent for the major part of the red fluorescence of the NV centers. Behind the pinhole, an optional Hanbury-Brown and Twiss setup configuration can be used for the measurement of photon correlation.

A frequency-doubled Nd:YAG-laser (Laser Quantum Gem 532 nm) with a wavelength

of 532 nm is guided through an acousto-optic modulator (AOM) (Crystal Technology 3200-146) that enables pulsing of the laser light if necessary. The light is then coupled into an optical fiber (Thorlabs PM460-HP) that is optimized for the Gaussian TEM_{00} ground mode. The coupling and decoupling of the light is conducted by two objectives (PL10x/0.25 and Olympus PlanN 4x/0.1) in a configuration, that widens the laser to a parallel beam with a diameter of about 1 cm. An optical filter for wavelengths of 535 ± 15 nm (Chroma HQ535/30m) cancels all possible wavelengths that have not been affected by the frequency doubling in the laser as well as any additional luminescence from the fiber. The direction of the polarization can be changed by the $\lambda/2$-waveplate (Thorlabs WPH10M-532).

A silver mirror directs the laser beam onto a beam sampler (Thorlabs BSF20-B). This beam splitter selectively reflects the incoming light of the incident angle of about 30° towards the objective, whereas the light coming from the objective and propagating to the detection channel will pass merely unhindered. Furthermore, one part of the beam that is not reflected passes through the beam sampler. Here, its intensity is detected by a photodiode (Thorlabs DET10A/M), which is connected to the AOM via a home-made proportional-integral-derivative (PID) controller (see figure 3.2). Hence, the intensity, that is coupled into the fiber, is controlled by an active feedback and the effective laser power fluctuations additional to intrinsic shot noise are reduced to 0.2% of the intensity.
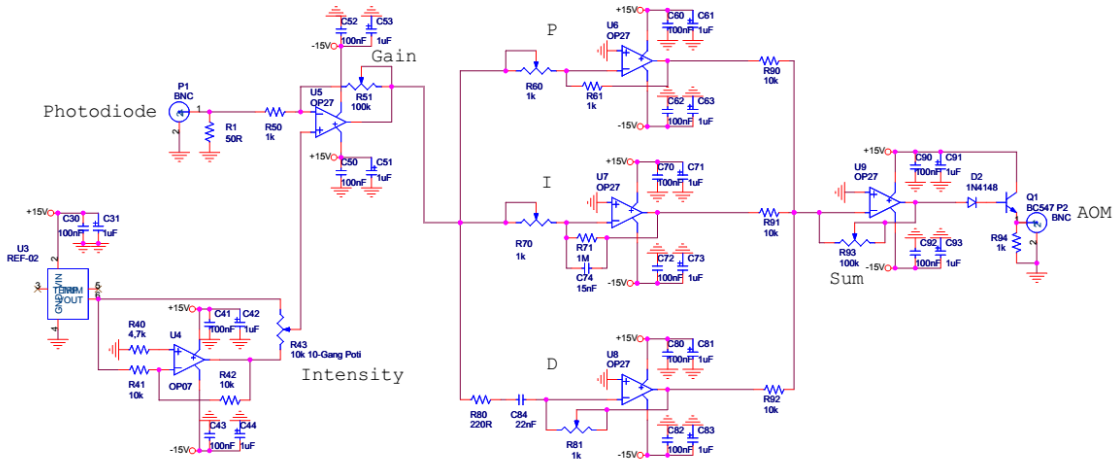

Figure 3.2: **Circuit diagram of the home-made PID Controller.** The voltage signal of the photodiode is stabilized by an active feedback to the AOM (Design by Manfred Bürzele, Institute for Quantum Optics). Thus, the effective laser power fluctuations additional to intrinsic shot noise are reduced to 0.2% of the intensity.

Typical experiments are performed with an oil objective of 60 times magnification and a numerical aperture of 1.35 (Olympus UPLSAPO 60XO), whereas the oil has a refractive

index of 1.517 (Fluka 10976). The objective is fixed to a piezo scanner (NPXY100Z25-102), that enables the relative movement of the sample to the objective. As the objective is used for both excitation and emission, the chosen beam sampler is transparent for most of the red fluorescence one expects from NV centers. Hence the fluorescent light passes into the detection channel, where it is bundled by a lens with a focal length of 10 cm (Thorlabs AC254-100-B-ML) and focused through a pinhole of size 30 μm (Thorlabs P30S). The light passes a longpass color filter (Chroma HQ655LP) that blocks all wavelengths below 650 nm. Thus nearly all fluorescent photons of the NV center can be detected by the avalanche photo diodes (APD) (Excelitas Technologies SPCM-AQRH-15) on which the remaining light rays are focused. At this place an optional 50:50 beam splitter (Thorlabs BSW10) can be inserted to add a second APD as a detector for a Hanbury-Twiss and Brown setup configuration [137].

3.1.1 Variation for GSD Microscopy

The GSD experiments, that are presented in chapter 4, were performed with slight variations of the confocal microscope. A beam sampler (Thorlabs BSF20-B) could be selectively installed right after the laser output to create a second light path. To prevent the loss of intensity, the guiding of the beam through the AOM and the fiber was skipped and substituted by a telescope system of two lenses with a ratio of 4:50 for the focal lengths (Thorlabs AC254-040-B-ML and Thorlabs AC254-500-B-ML) to widen the beam. After that, the beam path went through a vortex phase plate (VPP) (RPC Photonics VPP-1c) to create the doughnut-shaped intensity profile as shown in figure 3.3. This phase plate is a circular ramp whose steepness is calibrated for a certain wavelength (in this case 532nm). Opposing positions relative to the center feature a phase difference of the optical wavelength of π. Thus the central spot will show an interference minimum and the resulting total beam will be the desired doughnut mode [185] [186].

Furthermore a $\lambda/4$-waveplate (Thorlabs WPQ10M-532) is introduced to the beam path just behind the VPP to create circular polarized light. The necessity of this is caused by the focusing of the beam into the objective. In case of linear polarized light the focusing would lead to an effective field-component parallel to the optical axis which would counter the aim of an approximately neglectable field in the center of the focal spot. In case of circular polarized light this effect is canceled [187] [188].

The GSD beam path could be activated by a flip mirror in front of the first filter. In this configuration, a fast switch between the two measurement modes of the basic confocal microscope and GSD was possible.
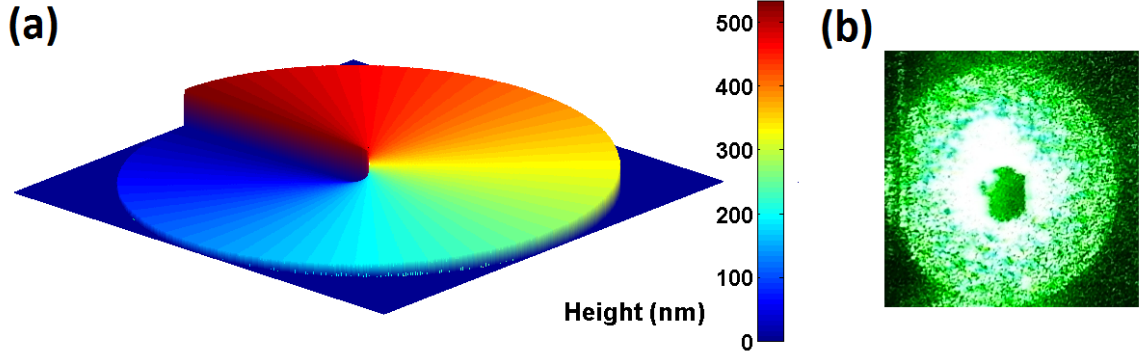
Figure 3.3: **Doughnut mode creation by a vortex phase plate.** (a) The vortex phase plate (VPP) is a helical ramp, whose steepness is adjusted to the wavelength (in this case 532 nm). Due to a phase difference of π of opposing parts of the beam, an optical vortex will be created in its center. (b) Picture of the blocked laser beam after passing through the VPP. The speckles and the noisy beam profile occur due to roughness of the surface of the beam blocker as well as the imperfect imaging of the sensor of the digital camera.

3.1.2 Detection Channel for Depth Localization

The depth localization experiments that are stated in chapter 5 and 6 require the simultaneous detection of two different wavelengths. Note that a large fraction of the reflected green light from the surface will also pass the beam sampler due to the nearly lateral incidence from the objective. Consequently just the spectral filters had to be arranged differently, as shown in figure 3.4.

The 650 nm longpass filter was placed directly before the in-line APD. In case of the other APD, a laserline filter for a wavelength of 532 ± 1 nm (Thorlabs FL532-1) was used to block any fluorescent light but just the reflection at the surface. Since the intensity of the green light still exceeded the limit of damaging the detector further gray filters of an optical density of 6 (that relates to a reduction of a factor 10^6) (Thorlabs NE40A /2x NE10A) were introduced to reduce the photon counts to a feasible amount. Since the signals of the two APDs could be separately evaluated, a confocal scan of the sample to identify NV centers was still possible without perturbations of the green light.
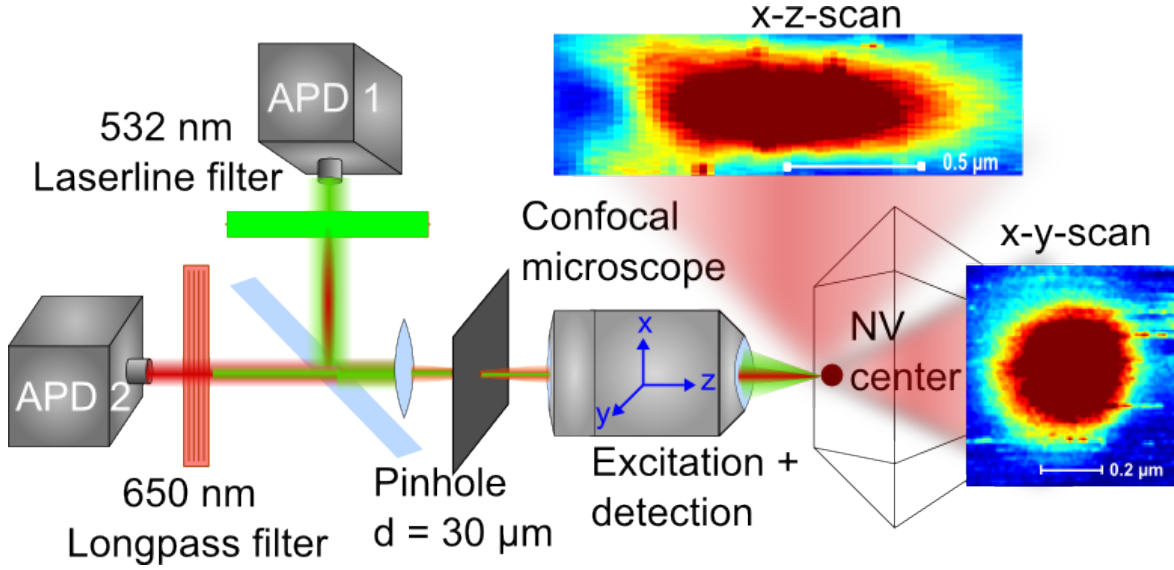
Figure 3.4: **Detection Channel for Depth Localization.** The detection channel was split up into one APD for green light and one APD for red light by putting different filters in front of each detector. A confocal scan to search for NV centers was still possible by only measuring the counts of APD 2. Exemplary scans of a NV center in x-y and x-z direction are depicted. (Figure published in [30])

3.2 Spectroscopy Experiments

This section presents the additional components used for the spin sensing experiments of chapter 7. Since NV centers imaged in these experiments were located underneath an aqueous liquid the objective was changed to a water objective with a 60 times magnification and a numerical aperture of 1.2 (Olympus UPLSAPO 60XW).

3.2.1 Supply of Microwaves and Magnetic Field

Figure 3.5 shows the configuration of the spectroscopy experiments. Microwaves in the frequency range of about 1000 MHz to 3500 MHz were generated by a vector signal generator (SMIQ) (Rohde & Schwarz SMIQ06ATE) and split up into two components with a phase shift of $\frac{\pi}{2}$ relative to each other by a microwave splitter (Mini-Circuits ZX10Q-2-34-S+ // 25-S // 19-S+). Both signals could be turned on and off by microwave switches (Mini-Circuits ZASWA-2-50DR+). The switches were controlled by the data timing generator (DTG) (Tektronix DTG5274) as well as the AOM for the laser to implement the desired pulse sequences. The resulting microwave signals were combined and amplified (Mini-Circuits ZHL-16W-43-S+). They were guided to a copper wire with a diameter of $25\,\mu$m (Goodfellow CU005171), that served as an antenna and was placed right on the surface of the diamond.
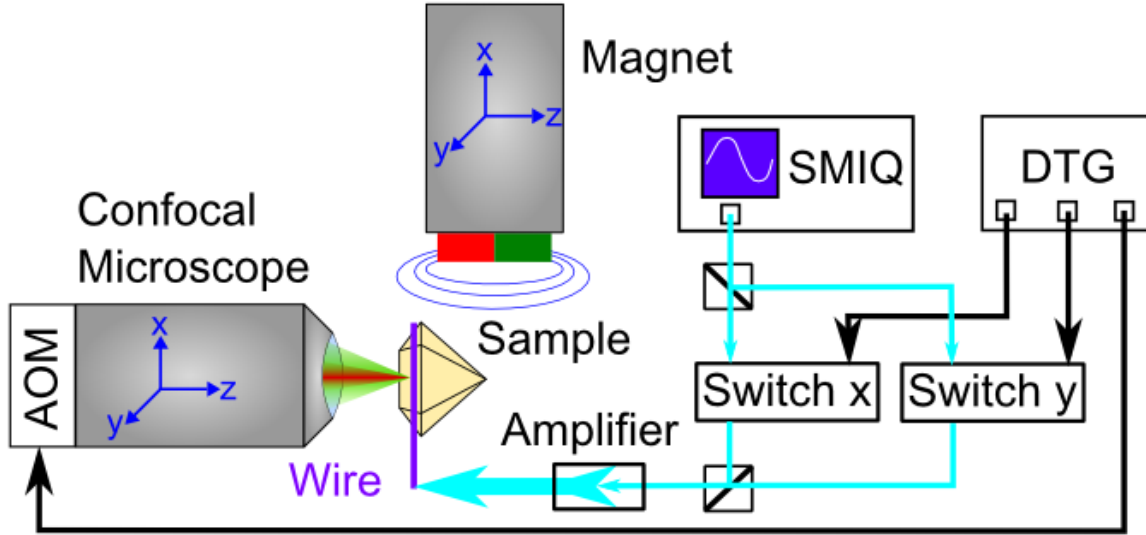
Figure 3.5: **Spectroscopy setup.** The signal generator (SMIQ) creates microwaves of the desired frequency that are split up into two components shifted by a phase of $\frac{\pi}{2}$. The data timing generator (DTG) operates the sequence of laser pulses (controlled by AOM) and microwave signals (controlled by switches). The combined microwave signal is amplified and guided to a wire located directly at the diamond surface. The magnetic field can be adjusted by a permanent magnet, that is placed on a combined translation and rotation stage.

The magnetic field, that was required for the measurements ($\sim 500\,\text{Gauss}$) was created by a permanent neodymium magnet (Magnetportal N52 D50-H15mm). The magnet was fixed to a stage and could be moved in 3 spatial dimensions. Additionally it was possible to rotate the orientation of the field to align it with respect to the NV axis.

3.2.2 Microfluidic Chamber

The spin sensing experiments included a special diamond sample containing created NV centers in a custom, lasercut microfluidic channel with a width of $90\,\mu\text{m}$ and a height of $35\,\mu\text{m}$. For the experiments a custom built transportation system for liquids was built as depicted in figure 3.6.

A polydimethylsiloxane (PDMS) block with carved channels with a diameter of about $1\,\text{mm}$ and a notch for the diamond enclosed the whole system by adhesive gluing to a cover slip. Liquid was stored in a reservoir and connected to the chamber by tubes (Idex Tygon LMT-55 SC0031T) of a diameter of $0.6\,\text{mm}$ and custom built metal tubes as connectors. The other side of the channel was connected to a syringe (B.Braun Omnifix 4616025V) by a canula (B.Braun Sterican 4657667). Hence, the liquid could then be sucked through this sealed system by negative pressure which was created by manually

pulling the syringe. An applied force in the order of $10\,\mathrm{N}$ could thereby create a flow of about $70\,\frac{\mu l}{s}$. However, this was only used to suck new liquid into the channel, since the experiments were performed on the investigation of static fluids.

A more detailed characterization of the sample and the assembly of the channel will be given in chapter 7.
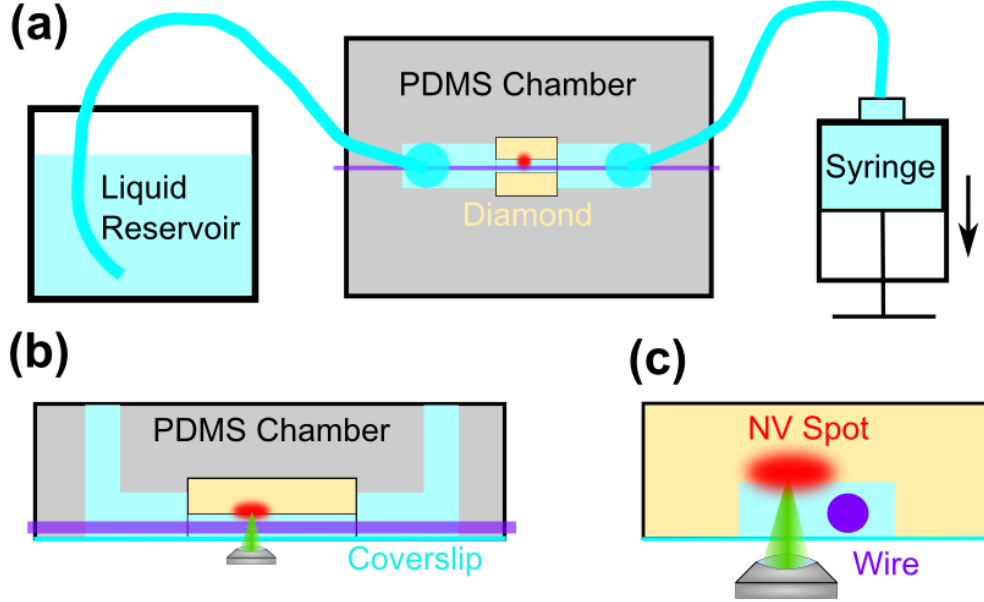

Figure 3.6: **Microfluidic Chamber.** (a) Topview of the diamond sample embedded in a PDMS chamber with the wire (purple) laid in the channel. The red spot indicates the region of interest with implanted NV centers. The liquid can be floated through the channel by negative pressure induced by pulling at the syringe. (b) A longitudinal cross-section parallel to the channel shows the channel in the diamond, that is the bottleneck of the whole liquid transportation system. The objective can focus on the NV centers through the coverslip, since the wire is placed shifted in the channel as depicted in (c) the lateral cross-section.

4 – Superresolution of NV Centers by GSD Microscopy

This chapter covers the results of the ground state depletion experiments on NV centers. The goal was to explore the capability of the method to resolve close NV centers within one diffraction limited spot of the confocal microscope, since such pairs are a valuable resource for applications like Quantum Information Processing (QIP) [189].

The first section describes the experimental determination of the resolution of a single NV center, whereas the second section investigates the differentiation of several close NV centers in one spot.

4.1 Determination of the Resolution

The presented measurements were taken out on an ultrapure CVD diamond sample with an enhanced ratio of C_{12} ratio of 99.99% of the total atoms. NV centers were created via implantation of $^{15}N^+$ ions with energies of $3\,\mathrm{MeV}$ and $10\,\mathrm{MeV}$ in defined areas. Figure 4.1 shows an overview of one square area of implanted NV centers with a side length of $10\,\mu\mathrm{m}$. It compares the basic confocal image to a GSD measurement. As expected from
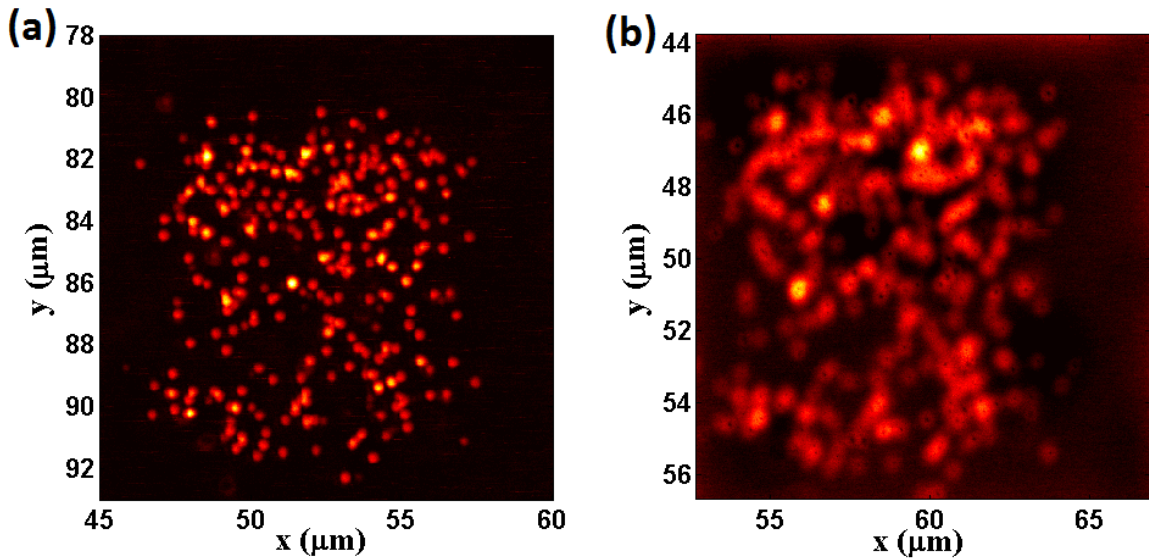
Figure 4.1: **Confocal picture and GSD.** (a) Confocal image of an implanted area of NV centers. (b) The same area viewed by ground state depletion microscopy. The NV spots get brighter, however the positions of the NV centers can be determined by the small dark spots in their middle.

theory (see section 1.2) the illuminated spots in the GSD picture are larger, however, the locations of the emitters can be determined by the small dark areas in the illuminated regions.

The first task was to test the resolution limit that can be achieved with the setup. Therefore single NV centers were imaged with different laser powers and the effective PSF function was analyzed. Note that in these experiments the central positioning of the VPP in relation to the laser beam is crucial as well as the rotation angle of the $\lambda/4$-waveplate. The quality of a proper GSD image and thus its total resolution is very sensitive to both aspects. Hence, the right alignment was achieved by iteratively measuring the PSF of a spot and adjusting both the VPP and the $\lambda/4$-waveplate.

A series of selected powers is illustrated in figure 4.2. The shrinking diameter of the GSD spot can clearly be seen, especially for the first images presented. As expected from equation 1.10 and its $\Delta r \sim I_m^{-\frac{1}{2}}$ behavior, the improvement of the resolution slows down for higher powers.
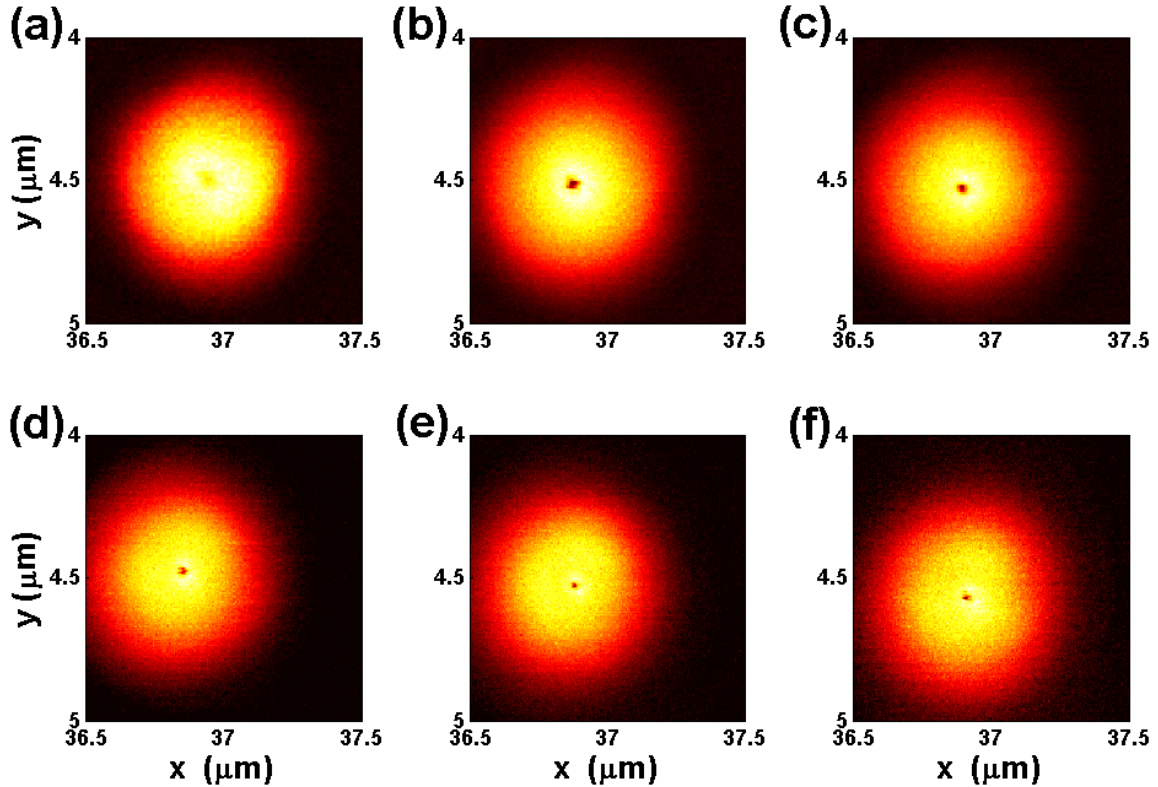
Figure 4.2: **Size of GSD spot for different powers.** Image of the GSD spot of an exemplary NV emitter for a laser output power of (a) 6 mW,(b) 15 mW, (C) 22 mW, (d) 40 mW, (e) 70 mW and (f) 100 mW. The sizes of the dark spots continues on shrinking by a $\Delta r \sim I_m^{-\frac{1}{2}}$ dependency.

The resolution is defined as the full width half maximum (FWHM) of the central dip

with respect to the maximum intensity that encircles the dark spot. Due to measurement imperfections, e.g. small inclinations of the surface, the images are not perfectly symmetric. Therefore, the center of the spot is calculated by a weighted center of mass of the intensity. From this point the intensity will be averaged azimuthally to show an average longitudinal intersection of the intensity profile.

The calculation of the FWHM will be a fit of the measurement data of the central peak to a Gaussian function $f(r)$ (compare [190] for STED) such as

$$f(x) = a_1 \cdot \exp\left(\frac{r^2}{a_2^2}\right) + a_3 \tag{4.1}$$

with the fitted coefficients a_1, a_2 and a_3, whereas the full width half maximum is given by $FWHM = 2\sqrt{\ln 2} \cdot a_2$. The Gaussian shows a good agreement to the behavior of the central dip as is depicted in figure 4.3. Even though background fluorescence from
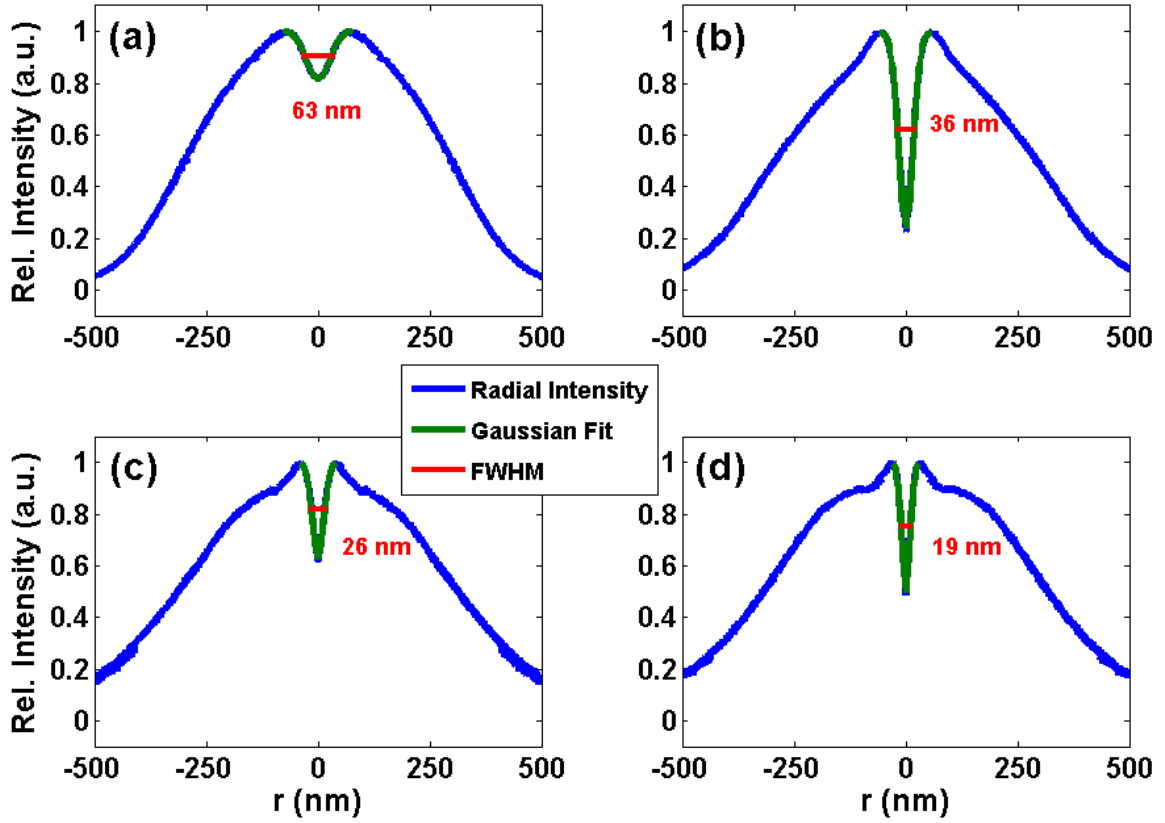
Figure 4.3: **Gaussian fit of GSD resolution.** Exemplary radial GSD intensity profiles (blue) for a laser output power of (a) 6 mW,(b) 15 mW, (C) 40 mW and (d) 70 mW. The intensity has been azimuthally averaged. A Gaussian function (green) was fitted to each central dip to determine the FWHM (red) as a criterion for the resolution.

the diamond and the immersion oil increases the intensity of the central dip, a relative improvement of the resolution by a narrowing central dip is still achieved for higher intensities.

To determine the resolution of the microscope, several images of a single NV center with different excitation powers have been recorded. The measurements have been carried out until a total laser power of $100\,\text{mW}$ that refers to an effective power of about $60\,\text{mW}$ passing through the microscope objective. At this point a further increase of the excitation power showed marginal to none improvement, whereas the fluorescence of the immersion oil rapidly increased as well as the danger of hitting the damage power threshold of the objective. The results are shown in the diagram in figure 4.4. As it can be seen the resolution matches the expected behavior to the intensity which drops as $I_m^{-1/2}$ as predicted by theory and similar to STED [190].
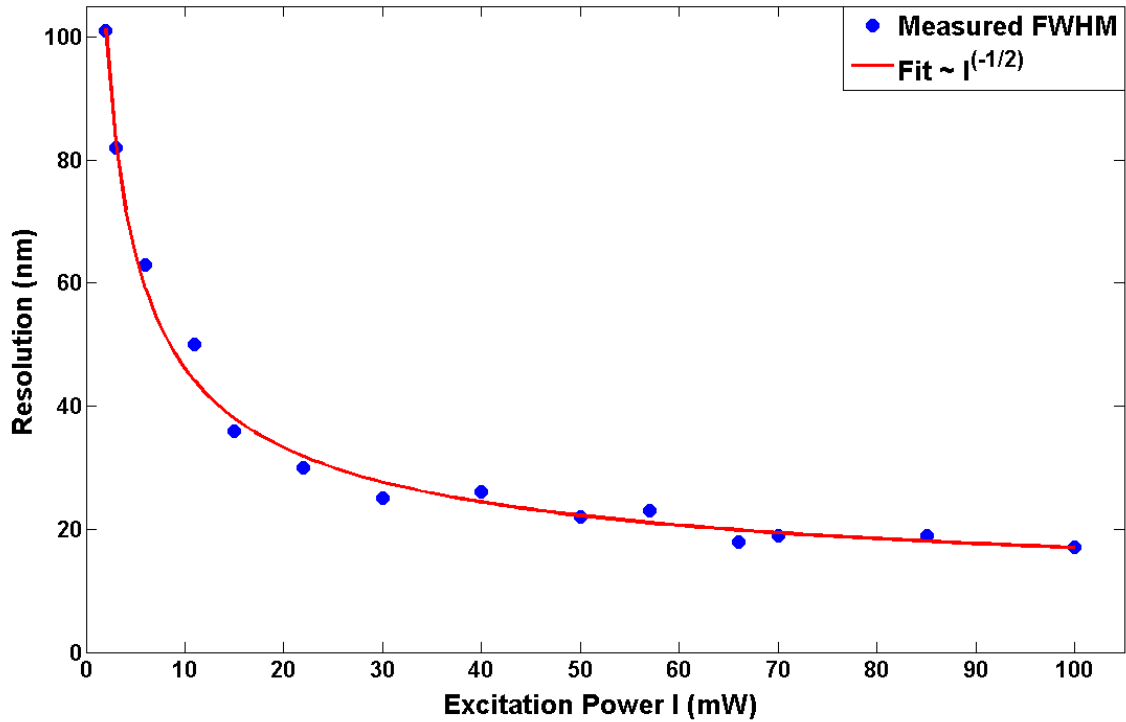
Figure 4.4: **GSD resolution depends on the exictation power.** The increasing excitation power leads to an improvement of the resolution, that matches the expected $I_m^{-1/2}$ behavior. The resolution limit of $17\,\text{nm}$ is achieved for an excitation power of $100\,\text{mW}$. No error bars are indicated, since the uncertainty of the fit is smaller than the shown dots.

The achieved resolution of $17\,\text{nm}$ is more than double the size as reported in literature with $7.6\,\text{nm}$ [16]. Since our setup was already at the technical limit without harming any components we were not able to push the resolution any further. However the results

showed to be sufficient to analyze several spots of close NV centers and measure their distance far below the diffraction limit.

4.2 Resolution of Single NV Centers in one Diffraction Limited Spot by GSD

With an achieved resolution below 20 nm experiments were performed to demonstrate the power of ground state depletion to resolve close emitters which are located within one single diffraction limited spot. Figure 4.5 zooms into two different regions of the area shown in figure 4.1. It shows the effect of GSD at a sample spot of several NVs. Small points occur in the illuminated areas to confirm the exact position of the NV centers.
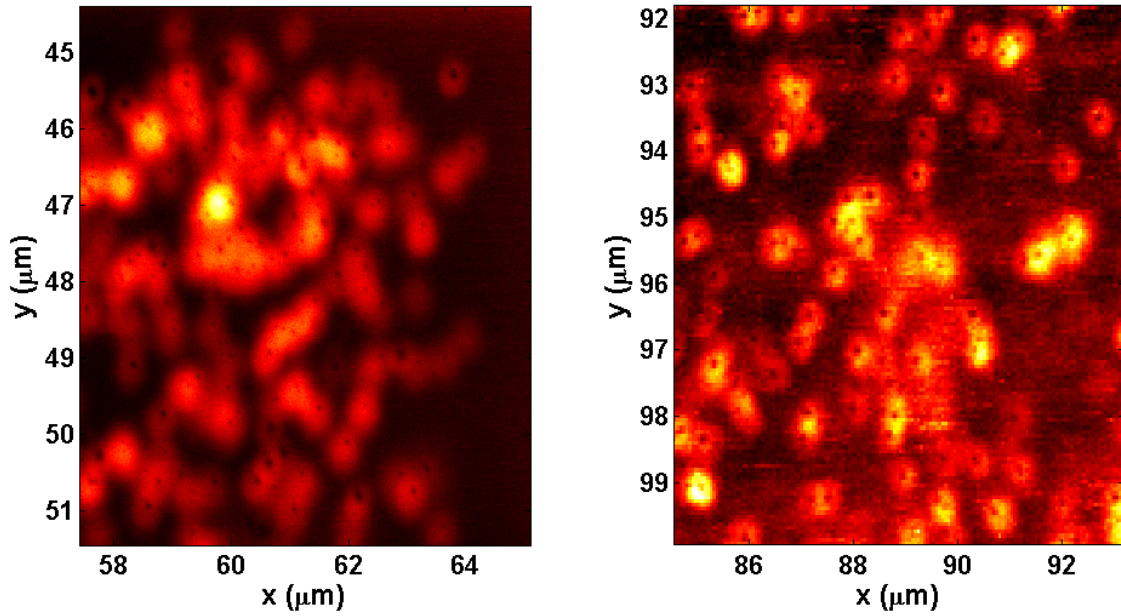
Figure 4.5: **Zoom into figure 4.1.** The two images zoom into different regions of the implanted area of figure 4.1. The pictures clearly resolve densely packed NV centers, that are closer than one diffraction limited spot.

The capability of resolution was then tested on merely isolated spots of several NV centers. Figure 4.6 shows two exemplary pictures of resolved NV centers. Their typical distance is in the order of 100 nm and, thus, way below the resolvable limit of the microscope as determined in the previous section. However, since the overlap of several emitters creates a quite inhomogeneous intensity spot compared to a single NV center, the exact number of emitters may not be obvious at first sight. Furthermore, the expected intensity dips can be partially absorbed by the high intensity areas of nearby emitters. For an exact determination of the positions, the image needs to be convoluted
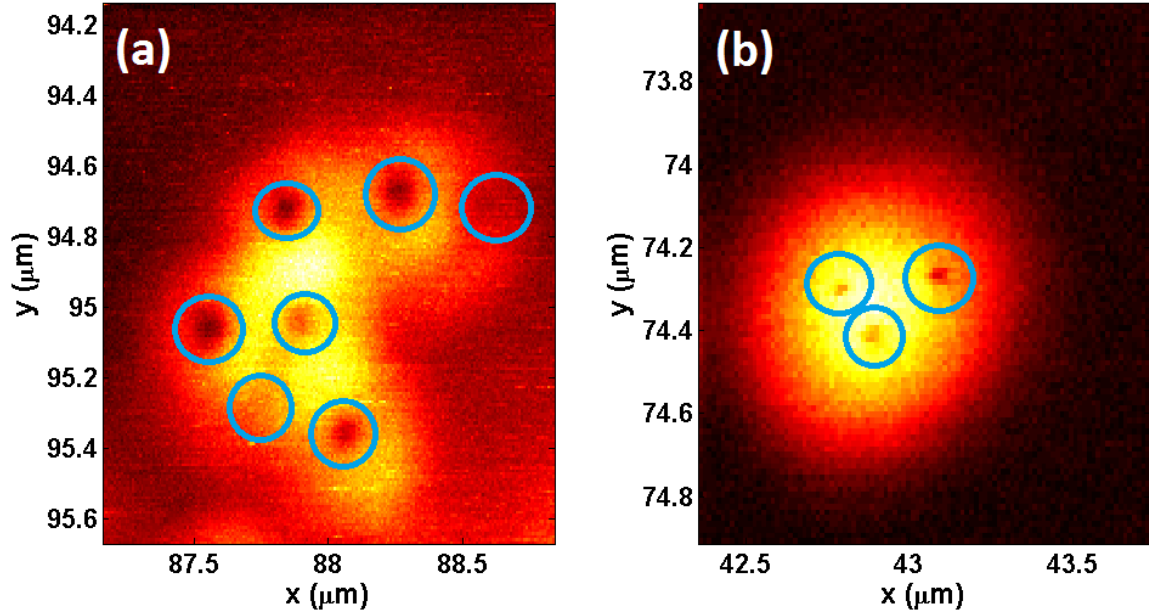
by the PSF of the microscope [16] [191].

Figure 4.6: **Isolated spots of several NV centers.** Though positioned in a bunch of several emitters, the locations of single NV centers can still be resolved. Here (a) 7 and (b) 3 different defects are placed in close proximity to each other. Some dark spots can only hardly be determined, since there is an overlap of all PSFs from the emitters. If an exact resolution is required, the pictures will need to be deconvoluted by the PSF first.

An important application of GSD microscopy was the investigation of custom-created NV pairs. The measurements were performed on a defined area with separated spots of implanted nitrogen. For each spot, 5 ^{15}N ions were implanted close to each other, whereas the distance between individual implantation sites has been 7.4 μm. The isotope ^{15}N has been used to confirm the artificial creation of the center, since it can be distinguished from the isotope ^{14}N. Before investigating the created NV centers by GSD microscopy, ODMR measurements confirmed the existence of ^{15}N in a certain spot by the characteristic hyperfine splitting. Since the natural abundance of ^{15}N is only 0.36%, the investigated NV center is likely artificially created (see also [122]). An antibunching measurement validated the existence of several NV centers in one spot. Typical distances of NV centers were comparable to 100 nm as shown in figure 4.6. However, one measured NV pair showed a much shorter distance, that could be hardly resolved as depicted in figure 4.7. The asymmetry of the darker region in relation to the illuminated spot stems from a slightly inclined surface of the diamond.

The lateral displacement of both emitters could be determined by a center of mass calculation for the region of each individual emitter (compare e.g. [22]). The resulting distance was evaluated to be 14 ± 2 nm. This is even better than the determined reso-
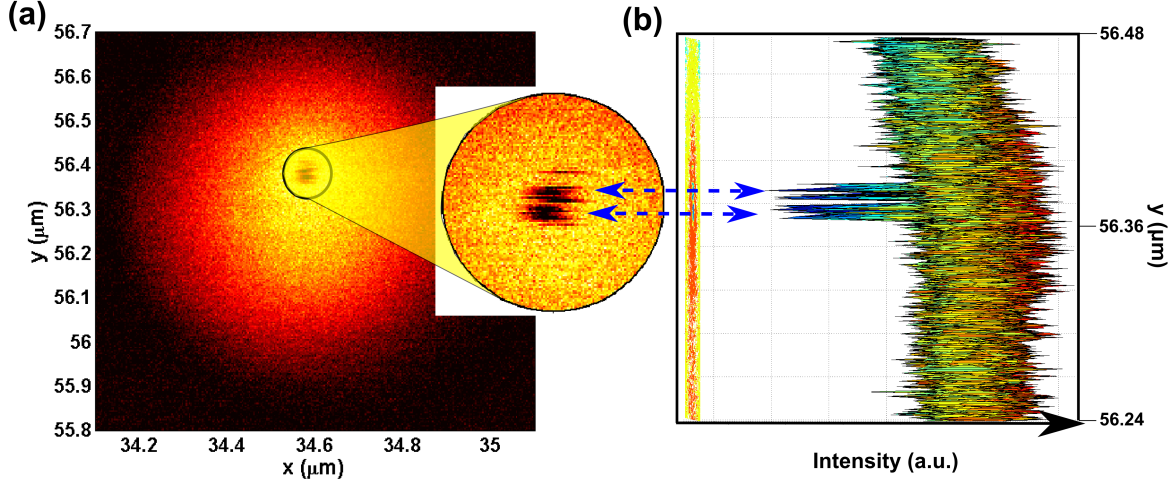
Figure 4.7: **GSD image of a resolved NV pair with a distance of 14 nm.** (a) GSD image of a NV pair with a distance of 14 nm. The asymmetry of the image is due to a slightly inclined surface of the diamond. The existence of two NV centers can be confirmed by antibunching measurements. (b) The separation of the two NV centers gets obvious in a side view of a three-dimensional intensity plot. The trench between the two emitters can clearly be seen in this depiction.

lution of 17 nm for our microscope. However, this is no contradiction, as the resolution of 17 nm only refers to the full width half maximum of the contrast, but not to the achievable precision. The principle is the same as the evaluation in the FIONA method (see section 1.3).

All in all, the measurements prove the successful application of our GSD microscope, that can assist in the optical characterization of close NV centers. This is a promising result, since the resolved distance is in the right order of magnitude to use dipole-dipole coupling of the NV centers [189]. Though our microscope could not match the resolution of 7.6 nm, we were able to distinguish a NV pair twice as close as the reported 27 nm for GSD [16] and approximately in the same distance as the 16 nm for STED in bulk diamond [192], as well as 10 nm for STED in nanodiamonds [193].

Note: The construction of the GSD setup and the measurements have been performed by the author together with diploma student Pascal Heller. Parts of the impressions of the experiments and results of the measurements have already been presented in the student's diploma thesis. The mentioned sample was provided by the company Element 6. The implantation of the NV centers was done in Tsukuba, Japan by Takashi Yamamoto, with whom the investigations have been carried out in Ulm.

5 — Depth Determination - An Optical Approach

This chapter lays out the foundations to optically determine the depth of NV centers in diamond. As already stated, this is of great interest for several experiments, e.g. when using the NV center as a magnetic sensor (see chapter 7). The first section states fundamental considerations about the method, followed by the second section, which discusses the experimental parameters that will influence the accuracy. The last section gives a theoretical approach to model the focal shift and compare it to the measurement results in chapter 6.

5.1 Fundamental Considerations

5.1.1 Assumptions

The aim of this method is the depth localization of single emitters by pure optical measurements of a confocal microscope. It shall enable a quite fast and easy determination of the position of an emitter below an optical interface with an accuracy that is far better than the diffraction limit along the optical axis. Our considerations specifically refer to the measurements of NV centers in diamond. However, the measurement principle certainly is applicable to other experiments as well.

For the sake of completeness it is important to begin with the two basic assumptions that - though seemingly trivial - underlie the whole method and evaluation principle. At first, the depth of a NV center is assumed to be fixed and not to change with time. The second assumption implies, that if one could perform an ideal measurement, with enough counts (resp. measurement time) and without any drift of the sample related to the objective and scanner, the difference between the two signals of reflected and fluorescent light would be only defined by the real depth of the NV center and a constant offset defined by the measurement conditions (due to e.g. chromatic aberration).

Note that if one of these two assumptions did not hold true, the whole measurement principle presented in this chapter would not be valid and reliable. The first assumption can be considered to be obviously true. As NV centers are often called trapped atoms in a solid state environment they show a stable position that does not change under standard ambient conditions. However, if the presented method is applied to moving fluorophores, the results will have to be treated differently and the evaluation will have to be adjusted, particularly concerning shorter measurement times. The second assumption, furthermore, is considered to be - trivially - true, as every known optical localization method in a more or less obvious sense is based on this assumption.

5.1.2 The Virtual Depth

According to general theory the position of the single emitter is exactly given by the maximum of the PSF of the fluorescent light (see section 1.3). However, in case of depth measurements along the optical axis below a refractive surface, it is obvious that the position of the maximum, that is measured with a scanning microscope, is not the real position of the PSF. Due to a - in this case - much higher refractive index in diamond, the position of the focal point is shifted by an unknown factor s. In fact, the real focal point of the microscope will be deeper than it occurs when just scanning the distance. This effect is illustrated in figure 5.1 for the boundaries of a focused beam in geometrical approximation. Consequently, any movement by the piezo scanner will be converted to a larger shift inside the diamond.
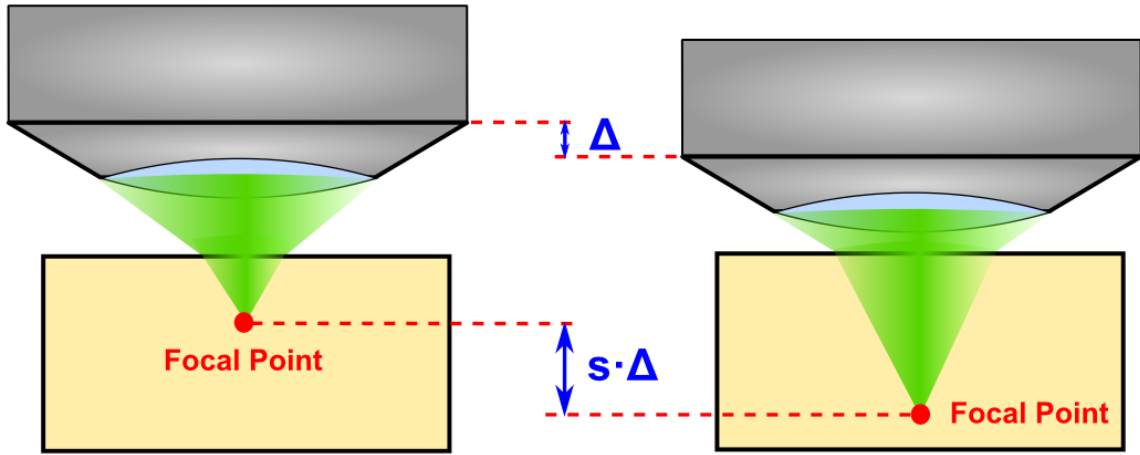
Figure 5.1: **Illustration of focal shift.** (a) The focused beam of light is refracted at the surface of the diamond to a deeper focal point. (b) This transfers to any movement of the objective in relation to the surface. A measured shift outside the diamond of Δ will be translated to a larger shift of $s \cdot \Delta$ inside the diamond. Obviously, this effect is highly dependent on the incident angle of the light. Hence, it will be stronger for objectives of a high numerical aperture.

If one wants to measure the depth of a single emitter by a pure optical method, the positions of the reflected surface and the emitter will have to be determined respectively the distance of both positions. This is realized by the simultaneous recording of two detection channels as presented in section 3.1.2, that distinguishes the wavelengths of the reflected and fluorescent light. One can assume the reflection of the incoming light occurs exactly at the surface plus a small possible shift e.g. due to evanescent waves of the Goos-Hänchen-Shift [194] [195] [196]. Since the incident beam is reflected at every point of the surface within the beam diameter, the measured signal of the reflected light in the detector will be called cumulated point spread function (cPSF) in order to

distinguish it from the PSF of a point-like light source. Hence, the maximum of the cPSF of the reflected light will give a position near the surface. All the same, the precise value of the shift remains unknown and has still to be determined (see section 5.2.3).
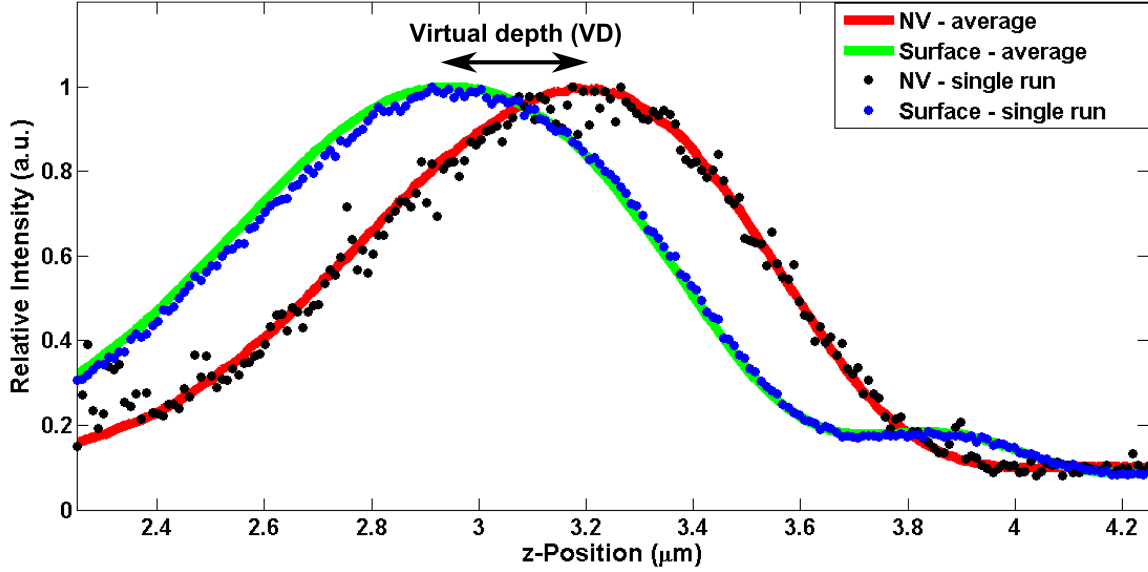

Figure 5.2: **The virtual depth (VD).** The figure compares the intensity profiles of a single measurement run of the fluorescence of the NV center (black spots) and the reflection at the surface of the diamond (blue spots). Moreover, the averaged intensity of 500 consecutive recordings are presented by the red (NV center) and green (surface) lines, that show a small perceptible displacement due to a drift of the sample during the course of the measurements. Since the difference between the positions of the maximums of both intensity profiles would be naively retrieved as the depth of the emitter, this value is called the virtual depth (VD).

The measurements are executed by a simultaneous detection of the reflected light (green) and the fluorescent light (red). Figure 5.2 shows a typical measurement recording. The difference of the maximums of both signals will then be called the virtual depth (VD) since it is the distance between surface and emitter one would naively retrieve out of this diagram. However as stated before, there is a focal shift (denoted as s) due to the different optical path lengths inside and outside the diamond. Second, the position of the surface is not necessarily represented by the maximum of the cPSF as mentioned in the previous section. And third the green and red light will be subject to a chromatic aberration in the optical components of the setup. The total value of all the effects that shift the cPSF to its true position if measured with red light is a constant denoted as c. If the real depth is called z_0, the virtual depth will be given by

$$VD = \frac{z_0}{s} + c. \tag{5.1}$$

The accuracy to which the real depth can be determined will be defined by the ability to determine the three values of VD, s and c for a certain NV center. The next section covers considerations about the measurement methods.

5.1.3 A Note about Polarization

Since reflection and refraction are dependent on the polarization of light, one has to consider effects that could influence the measurements of the virtual depth.

In case of reflection of the linear polarized excitation beam, one would expect no change of the position of the maximum of the cPSF due to rotational symmetry. This holds as long as surface roughness and tilt is neglectable. However, the optical components of the microscope e.g. beam splitters and filter are expected to show polarization dependence that likely influence precise measurements.

In case of the NV center, the polarization of the excitation affects the number of emitted photons. If the NV axis does not match the excitation, the total intensity, and thus the precision of the localization, will be distinctly decreased. Furthermore, the orientation of the NV axis can lead to different emission patterns. This is due to an interaction of the NV center with the light field close to the diamond surface, where part of the emitted light will be back-reflected [197]. Consequently, the dipole orientation is capable of changing the precision of the localization [198].

Nevertheless, changing the polarization of the excitation was experimentally tested. The measurements showed an unequally variation of both maximum positions (of cPSF and PSF) when changing the polarization. Consequently, to keep results comparable, all evaluated measurements of this thesis have been performed with the same configuration of excitation polarization that matched the axis of the selected NV centers.

5.2 Measuring the Experimental Parameters

This section specifies the experimental determination of the three parameters VD, s and c, that is necessary to calculate the real depth of a NV center according to equation 5.1.

5.2.1 Calculation of the Virtual Depth

The crucial step to determine the virtual depth is the determination of the maximum position of the reflected and the fluorescent light as precise as possible. In an ideal case the intensity distribution of the confocal microscope along the optical axis will be given by the Airy distribution. Since this function can be approximated as a Gaussian with adequate accuracy, many works in literature use a calculation based on a normal distributed light spot, though this is not necessarily the ideal method to localize an emitter [102] [199]. The precision of the determination of the maximum is then defined by two factors. First, the PSF width defines the probability to collect a photon in a certain position. Second, the more photons one collects as an ensemble, the more accurate the position estimation gets $(\sim \sqrt{N}^{-1})$. Thus, the precision is dependent on the measure-

ment time (see section 1.3).

Figure 5.2 illustrates the problem for the specific measurements, that have been performed. As it can be seen, the pattern itself is not symmetric. The local maxima beside the main distribution do not show up on both sides of the distribution as well as the skewness of the distribution. The asymmetry is in total agreement with theoretical works on the detection of a reflected beam by a confocal microscope [106]. There are two graphic reasons to explain this effect: First, the effective aperture of the objective increases for a closer position to the diamond: The visual angle of the aperture of the objective as seen from the position of the emitter increases. That relates to a greater potential fraction of the emitted light, that can be detected. Second, the optical path length in the diamond is different to the one in the immersion oil. This is represented by the focal shift, that has already been mentioned in section 5.1.2.

Consequently, the first task to solve is the finding of a proper evaluation algorithm respectively a fitting function. To minimize the influence of any deviations that lie outside the main maximum of the distribution we will only fit the maximum region of the intensity distribution. A feasible proceeding is the calculation of the moving average for 100 nm in both directions at each point. The maximum of this smoothed distribution is then determined and all points, where the intensity drops below 85% of the maximum, will be skipped, as it is illustrated in figure 5.3.
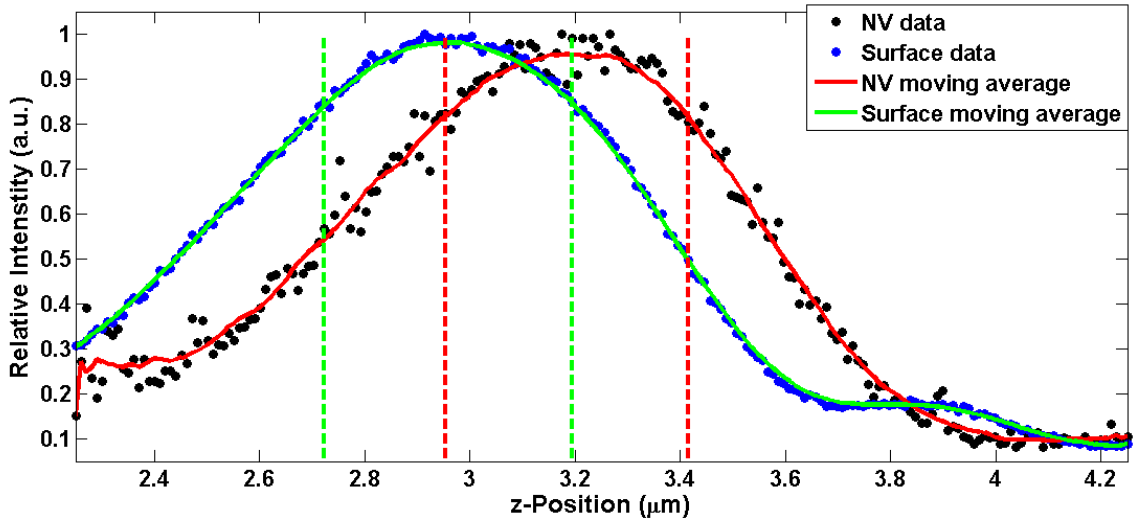

Figure 5.3: **Moving average of the intensity profiles.** A moving average of the measured intensity profiles (red and green lines) for the NV center (black dots) and the reflection (blue dots) can be calculated to get the average region of the maximum. The dashed lines represent the boundaries, where the intensity profiles drop below 85% of the main maximum. Only the measurement data in between these regions will be used for calculating a fitting function to the maximum.
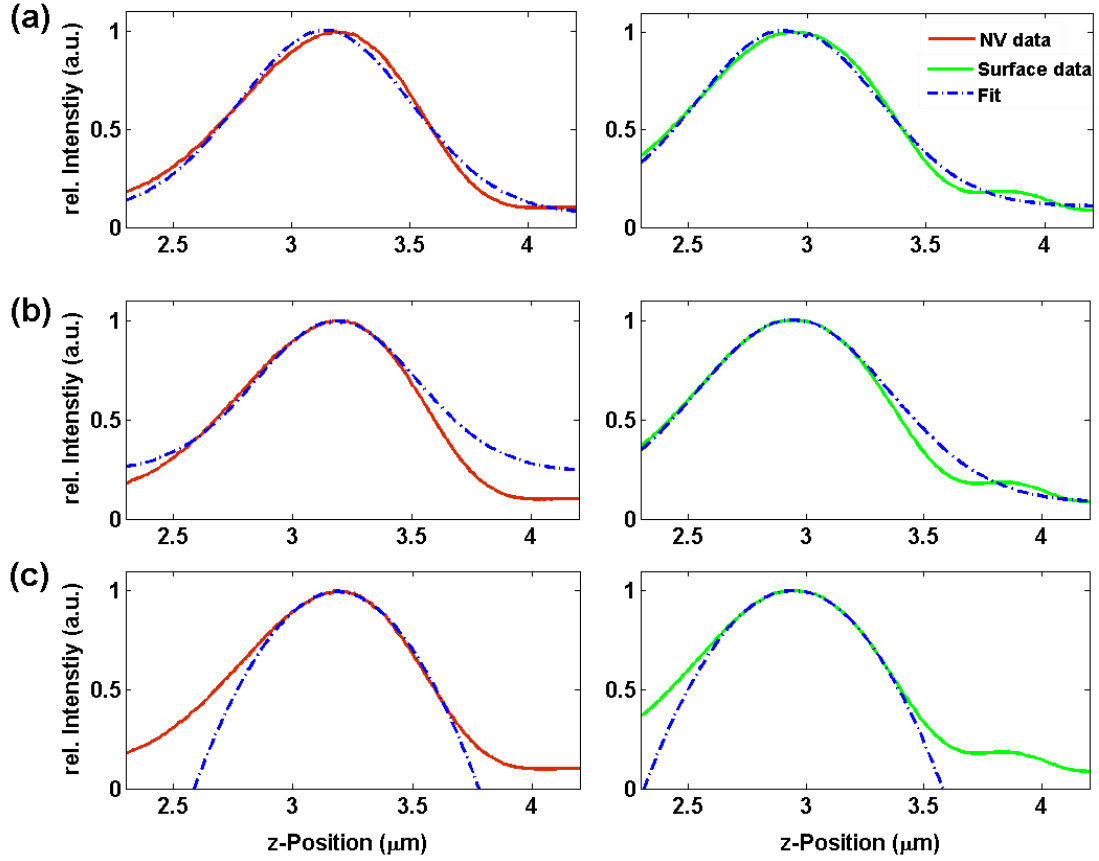
Figure 5.4: **Fitting of the maximum positions.** The expected intensity profiles of NV center and surface have been retrieved by a summation over 500 recorded measurements. Due to the asymmetry the fits have been calculated for functions separated in two parts by the Heaviside distribution. (a) The Gaussian fit to the complete profile shows a strong deviation of the fitted maximum to the obvious position. (b) A much better agreement to the measured data is achieved by fitting the Gaussian to only the maximum region. (c) In this region the results for a parabolic fit show no difference to the Gaussian, both giving calculated values of the maximums of 3.197 μm for the NV center and 2.946 μm for the surface.

The original measurement data is used for the fitting calculations. Since now we only have to fit a function to the middle of the maximum, it is possible to approximate this with a simple parabolic function instead of a commonly used Gaussian. One can calculate, that in the regime of our fitted values the difference at the boundaries of both functions is about 1%. Furthermore we need to consider the asymmetry of the measured distribution. This is done by separating the fitting function into two parts with

independent curvature. The effective fitting function is then given by

$$y_i(z) = a_i z^2 + b_i z + c_i \tag{5.2}$$

where $i \in \{1; 2\}$ is an integer and a_i, b_i and c_i represent our fitting parameters. Using the Heaviside distribution H and the boundary condition $y_1(h) = y_2(h)$, all calculations are then performed under the constraint

$$F(z) = H(h - z) \cdot y_1 + H(z - h) \cdot y_2 \ . \tag{5.3}$$

Figure 5.4 compares this evaluation method to the fitting of a Gaussian to the whole intensity profile as well as only to the chosen area. In terms of uncertainty considering the fitting of the maximum position calculations show a deviation at the scale of few picometers when choosing a Gaussian or a parabolic fit. Since this is much smaller than the extension of the wave function the parabolic fit proves to provide reliable results. Furthermore, the parabolic function has one degree of freedom less to fit than the Gaussian, that is an advantage considering calculation time.

One great benefit of the averaging is the better signal-to-noise ratio (SNR) for the fitted data points. Since there is always constant background fluorescence from the diamond, the low intensity values far from the maximum of the distribution are much more unreliable measurement points than the ones in the center. Hence, the selective fitting decreases the effective SNR that leads to a more precise localization [23].

5.2.2 The Focal Shift Correlation

The focal shift s is the second parameter to determine. Here, the focal shift is defined as the displacement of the maximum of the PSF of the NV center compared to its virtual position measured in the experiment. As mentioned, the occurrence of this shift has its roots in two phenomena. At first the optical pathlength in the diamond is longer than in the immersion oil due to a higher refractive index. Second, the diamond surface acts as an effective lens when interacting with the focused light beam. Thus the effect can be thought of similar to a spherical aberration.

From a naive point of view, one could argue that the total shift is given by the ratio of the refractive indices of diamond to immersion oil, as is suggested in figure 5.1 for the boundaries of the beam. However, if one takes into account the different incident angles of all rays closer to the optical axis, different focal points will occur and the simple assumption will not hold. Furthermore, the laser beam is not a geometrical bundle of rays but can be better described as a Gaussian beam, that leads to a different calculation. A more detailed model based on these considerations for the focal shift s will be discussed in section 5.3.

Since the theoretical calculation of s is non-trivial, one wants to think of an experimental method to measure s. Indeed, the simultaneous measurements of the cPSF of the surface and the PSF of the emitter provide an excellent resource to the solution of this problem. Assuming a defined uncertainty Δ of the maximum positions of the surface z_{surf} and

the emitter z_{em}, one can state:

$$z_{surf} = z_{surf,ideal} \pm \Delta_{surf} \, , \tag{5.4}$$

$$z_{em} = z_{em,ideal} \pm \Delta_{em} \, . \tag{5.5}$$

Typically, one will expect $\Delta_{surf} < \Delta_{em}$, as the reflected light has a smaller wavelength than the fluorescent light, and thus a smaller distribution width. Moreover, in a typical measurement setup, the number of reflected photons is larger than the number of fluorescent photons. This increases the ratio of accuracy even more. Consequently, z_{surf} can be determined more accurate than z_{em}.

Nevertheless, there is an important fact to point out: The ratio of the uncertainties does not depend on the measurement time, as the ratio of the wavelengths stays the same as well as the ratio of the measured counts. Now take into account a small drift of the sample, that occurs during the measurement time around its average position. If one assumes the sample to drift as a whole, the position of the surface will change by a small displacement δ. Since the optical path length in diamond is stretched, and thus is the focal spot, the virtual displacement of the emitter will be reduced to δ/s. Consequently, this leads to a slight correlation when comparing the measured maximums, as can be seen in figure 5.5.
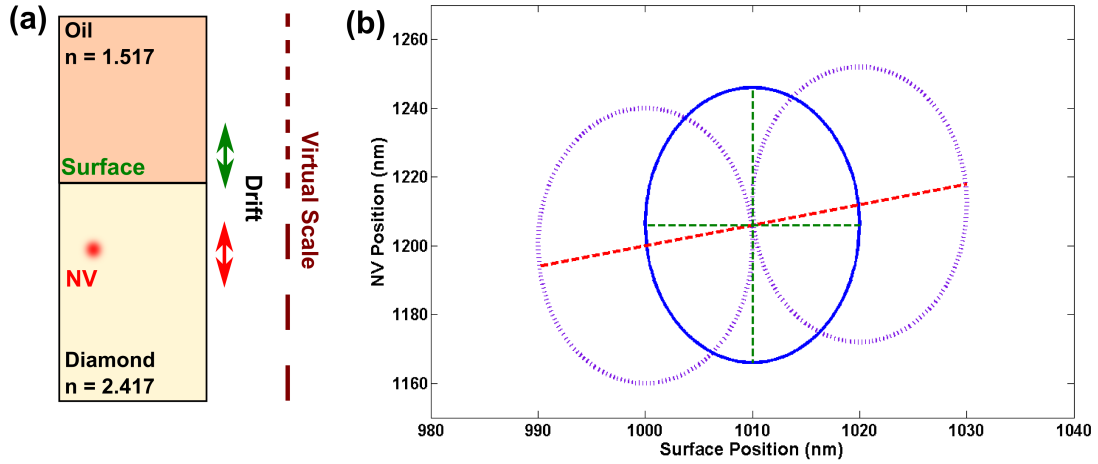
Figure 5.5: **The focal shift correlation.** (a) The drift of the sample will be the same for the surface and the NV center. However, since the virtual scale (red) is stretched due to different optical pathlengths, the measured drift of the NV center is shortened. (b) Consequently the measured positions will show a correlation. The diagram relates to a random drift around the central position (dashed red line). The basic measurement uncertainties of the maximum positions are indicated as ellipses (blue and purple) around the drift line.

Using the sample drift as an advantage to gain information about s is a nice feature. To increase the precision of the calculation of s the drift has to be high enough compared

to the uncertainties of the maximum positions. However, it is important to note, that this only works for slight drift oscillations at the averaged position. If the drift is too high and leads to a permanent displacement of the sample, this, on the contrary, will reduce the precision of the method. Therefore, measurement time and speed have to be synchronized in the right way to all occurring noise effects. Then, it is possible to get meaningful data for all parameters as presented in chapter 6.

5.2.3 The Calibration Constant

The displacement constant c is the last experimental parameter that has to be determined. As stated before, this constant is mainly influenced by chromatic aberrations of the optical components, as well as a shift of the maximum of the cPSF to the real position of the surface. Since it is not only a chromatic shift in the microscope, c cannot be determined by a change of the excitation wavelength to red color.

Hence, a calibration measurement is needed. In this case, the measurement of the position distribution of shallow implanted NV centers was chosen. These emitters had been created by Nitrogen implantation of an ion energy of 2.4 keV. It is known, that this implantation energy creates shallow implanted NV centers very close to the surface with the closest NV centers at about 1 to 2 nm below the surface [152]. Therefore, if one measures the virtual depths of enough of these NV centers, the measured distribution should show a lower boundary. At this limit one can expect to be at the surface with an uncertainty of about 1 nm.

In this work 101 shallow implanted NV centers have been measured and evaluated to determine the calibration constant c. Since these measurements are very time consuming, an easier calibration is suggested for further applications of this method. As noise spectroscopy on shallow implanted NV centers is now a well established tool [63] [181], this method can provide accurate depth measurements of the NV center (see also section 6.3.4).

5.3 Modeling the Focal Shift in Diamond

In this last section of our preliminary considerations to the depth determination we will calculate the expected behavior of the focal shift s. All in all, this is a two-sided problem. On the one hand, one has to take into account the refraction of the excitation beam. On the other hand the detection of the emitter will lead to an additional shift.

The refraction of a focused beam at a planar surface has been widely discussed [200] [201] [202]. It can be stated, that both, geometrical and wave-like approximations for the light propagation, principally lead to similar results, that is, especially, the already discussed focal shift s [203]. In this treatment, we use a hybrid model (as presented in [30]), that covers geometrical ray tracing as well as wave-like characteristics for a Gaussian beam. We separate the detection process into two parts: first an excitation by a Gaussian beam and second the following detection of the light from a point source (NV center).
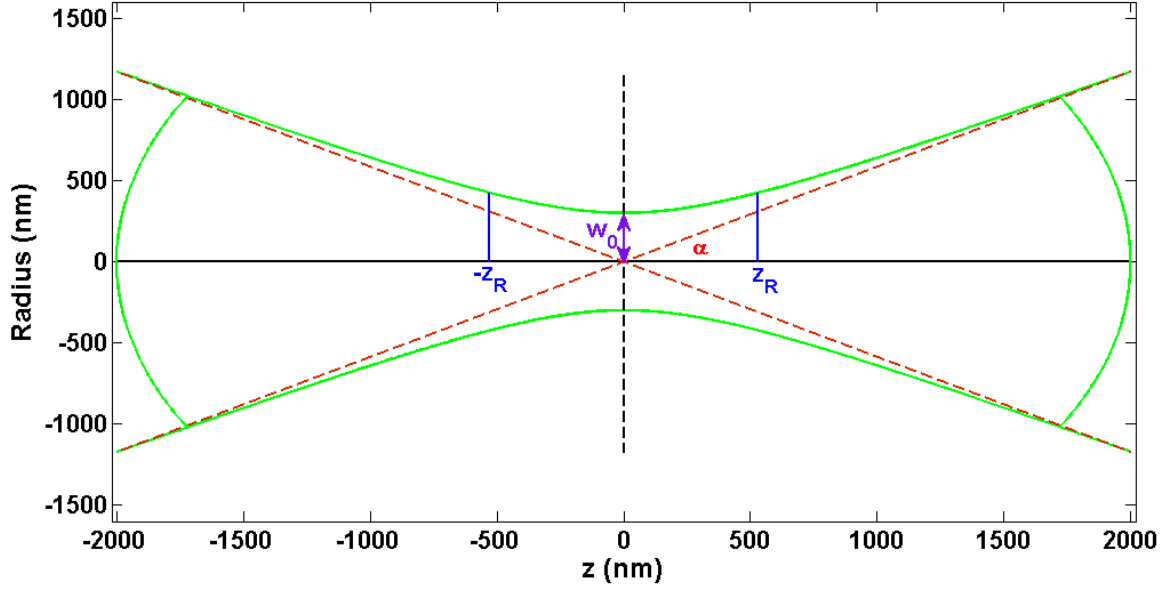
Figure 5.6: **Focal region of a Gaussian beam.** The objective focuses the Gaussian mode of the laser. The resulting focal beam waist w_0 is determined by the wavelength λ and the incident angle of the boundary $\alpha = \arcsin\left(\frac{NA}{n_1}\right)$. The Rayleigh range z_R is defined as the distance to the focal point, where the beam waist shows the value of $w\left(z_R\right) = \sqrt{2} \cdot w_0$ and, thus, refers to a doubled cross-section of the laser beam.

We approximate the Gaussian beam by its boundaries near the the focus. The quantities used in this model are illustrated in figure 5.6. Considering a distance z to the focal point, the laser beam waist $w(z)$ is then given by

$$w(z) = w_0 \left(1 + \left(\frac{z}{z_R}\right)^2\right)^{1/2} \tag{5.6}$$

with the waist size w_0 and the Rayleigh range $z_R = \pi w_0^2 / \lambda$. The waist size is determined by the objective with a numerical aperture $NA = n_1 \sin \alpha$ by

$$w_0 = \frac{\lambda}{\pi \alpha} = \frac{\lambda}{\pi \arcsin\left(NA/n_1\right)} \ . \tag{5.7}$$

To derive the incident angle of the beam boundary one has to calculate the derivative $w'(z) = \tan \alpha$. It holds

$$w'(z) = \frac{w_0 z}{z_0^2} \cdot \left(1 + \left(\frac{z}{z_0}\right)^2\right)^{-1/2} \ . \tag{5.8}$$

To trace the ray at the boundary we apply Snell's law of refraction for the refractive indices of two media n_1 and n_2. This gives the focal shift s_{exc} of the excitation. We obtain

$$s_{exc}(z) = \frac{w'(z)}{\tan \arcsin \left(\frac{n_1}{n_2} \sin \left(\arctan w'(z) \right) \right)} \ . \tag{5.9}$$

So far only the excitation beam has been considered. Furthermore we have a look at the detection of the emitter. We assume the detection to be defined by the PSF of the emitter, that is approximately given by a Gaussian distribution

$$f(z) = f_0 \exp \left(\frac{-z^2}{2\sigma^2} \right) . \tag{5.10}$$

Now, the value of s_{exc} can be integrated into this detection as follows: Assume a certain distance z from the focal point. Here, we partially weight the calculated focal shift due to excitation s_{exc} with the cumulated distribution function of a normalized Gaussian $CDF(z, 0, \sigma)$ with the mean 0 and the standard deviation σ. The other part of the PSF is weighted as 1, since it is outside the diamond and therefore not shifted. The total shift s then denotes as

$$s = CDF(z, 0, \sigma) \cdot s_{exc}(z) + (1 - CDF(z, 0, \sigma)) \ . \tag{5.11}$$

A numerical calculation with the initial values of the excitation wavelength $\lambda = 532\,\mathrm{nm}$, the standard deviation of the distribution $\sigma = 0.5\,\mu\mathrm{m}$ and the refractive index of diamond $n_2 = 2.417$ was performed for several types of objectives (oil ($n_1 = 1.517$), water ($n_1 = 1.33$) and air ($n_1 = 1$)). The results are illustrated in figure 5.7.

The total focal shift shows to be highly dependent on the numerical aperture. High NA objectives as $NA = 0.95$ for air or $NA = 1.2$ for water display a significantly higher shift than their counterparts with lower NA. Furthermore, according to this model, one expects the focal shift to increase for deeper emitters due to a change of the incident angle and a larger part of the PSF inside the diamond. In all cases, this increase continues until a depth of about $1.5\,\mu\mathrm{m}$ is reached. There, the focal shift asymptotically reaches a limit.

Referring to the increase for the less deep NV centers, the experimental results, that are presented in the next chapter are in good agreement to this prediction.
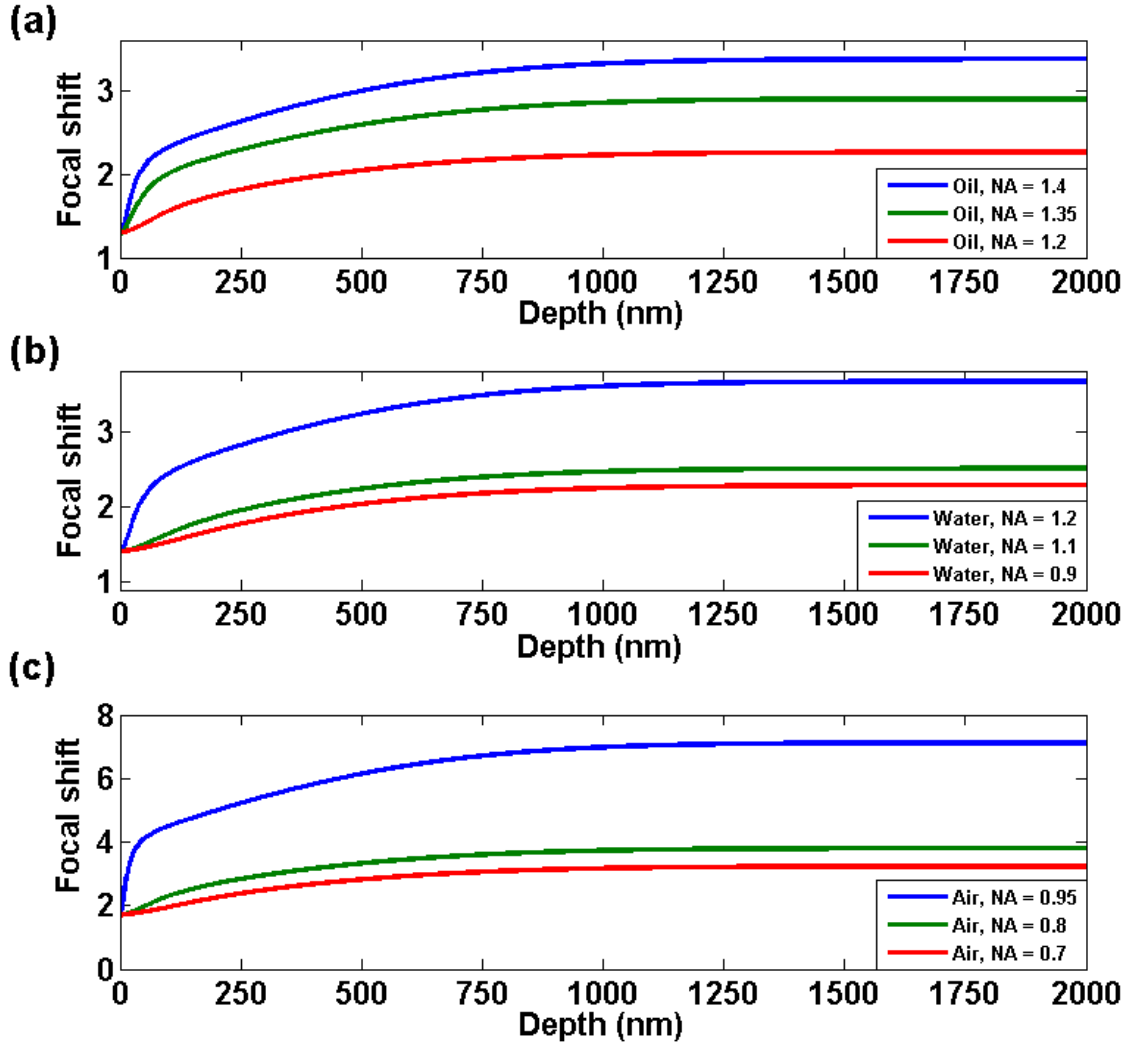
(a)

(b)

(c)

Figure 5.7: **Modeling of the focal shift.** The calculations are performed for different objectives of type (a) oil, (b) water and (c) air. The total focal shift is highly dependent on the numerical aperture of the objective and rapidly increases for high NA. Furthermore, the shift asymptotically reaches a limit for emitters deeper than $1.5\,\mu$m.

6 – Optical Measurements of the Depth of NV Centers

This chapter presents the performed measurements and results under the assumptions of chapter 5. The first two sections review the determination of the virtual depth and the correlation of the focal shift. Using this, the last section then shows the calibration of the measurements by an investigation of a shallow implanted spot of NV centers and discusses the total resolution of the experiment. The results have been published in [30].

6.1 Examination of Drift Effects and Noise

The first section deals with an analysis of occurring drift effects and noises. These effects naturally limit the absolute accuracy to which the virtual depth respectively the real depth of the NV centers can be determined.

6.1.1 Surface Roughness
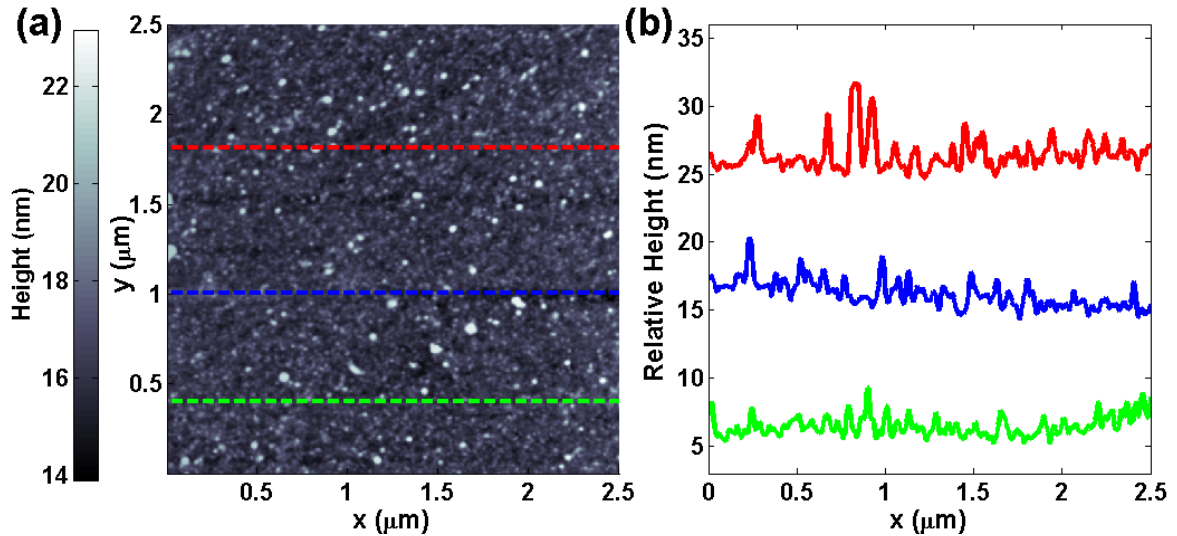
Figure 6.1: **Surface Roughness.** The roughness of the diamond can be determined by atomic force microscopy (AFM). (a) The surface of $2.5 \times 2.5\,\mu\text{m}^2$ at the implantation area shows a merely flat profile with occasional elevations in the order of few nanometers. (b) Three lines, that have been relatively shifted to each other show linear sections at the indicated positions. The average roughness over a region of size $1\,\mu\text{m}^2$ is determined to be below $0.93\,\text{nm}$.

One of the first things to consider, when measuring the depth of a NV center, is the roughness of the surface of the sample. Obviously the precision of depth only makes sense to the same order of magnitude as the surface roughness.

Atomic force microscopy (AFM) measurements have been performed to investigate the two samples used for the measurements. Both samples showed a flat surface with an average roughness below $0.93\,\mathrm{nm}$ over a surface area of $1\,\mu\mathrm{m}^2$ around the implantation area, where the later NV measurements would take place. Figure 6.1 illustrates an exemplary surface profile. As one can see, only small deviations from a virtually flat surface can be reported.

Furthermore, the surface should be aligned perpendicular with respect to the optical axis. Otherwise, all position values would be subject to a projection error. Additionally, the roughness could be virtually increased. Both effects can be estimated with a behavior of the cosine of the tilt angle α, that represents the difference to the ideal perpendicular orientation. The total tilt of the samples could be determined by the count signal of the surface in a x-z-scan. It showed to be less than $1°$. This results in an estimated relative error of less than 0.02% for all length measurements along the optical axis. Thus, we confidently neglect any error of tilt.

6.1.2 Shot Noise and Drift Analysis

As stated in section 1.3, the limiting factor of accuracy in FIONA measurements is the number of collected photons, respectively the measurements time. One of the great advantages of the NV center is its photostability to bleaching [44]. Thus, one is not limited by the measurement time, but by the drift of the sample position with respect to the setup.

The total drift effects occurring in the experiments can be evaluated. Figure 6.2 shows typical drift behavior of the diamond surface, determined by the fitted maximum position of the reflection signal. The graph corresponds to an exemplary behavior of the sample and results in a precision of the virtual depth below one nanometer (see below).

While measuring, the samples typically showed an absolute movement of about 20 nm perpendicular to the optical axis and about $40\,\mathrm{nm}$ along the optical axis. Since the depth measurements rely on a relative distance measurement, one has to note that any drift along the optical axis does not necessarily reduce the precision. However, this only holds true in a certain regime. Due to thermal fluctuations, oil drag on the sample caused by the relative movement to the objective, or other vibrations, sudden jumps of the position of the sample by tenths of nanometers are possible. These effects show to come along with unstable perpendicular positioning, that worsens the achieved precision significantly (typically by a factor of 2 to 5). Such results have not been used in our final analysis in section 6.3. In this context, it is interesting to mention that some NV centers showed an intrinsic higher uncertainty as others. It can be assumed, that specific surface roughness at particular emitter positions might play a role.

To gain basic information about the precision of the virtual depth, we performed several consecutive scans of one NV center along the optical axis, and calculated the virtual
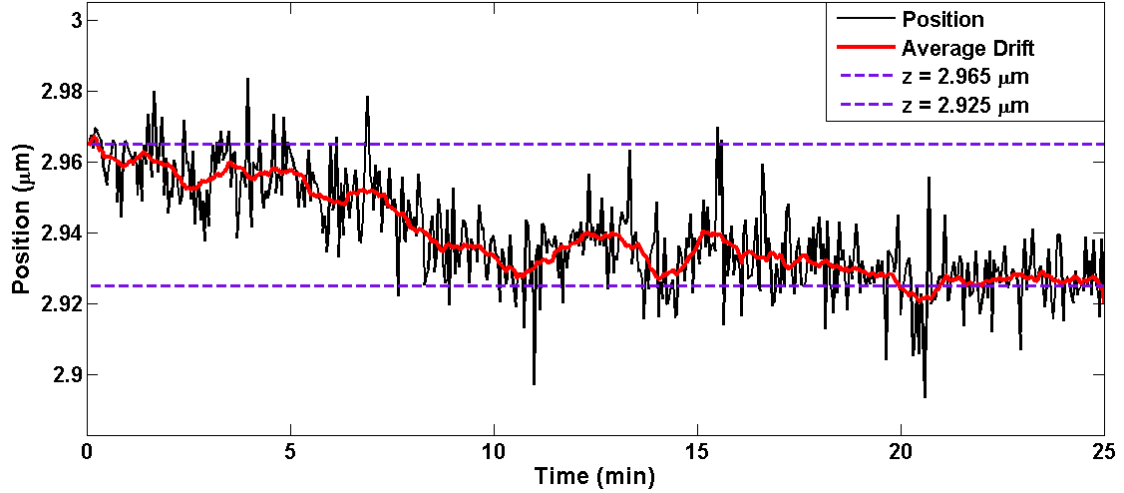
Figure 6.2: **Sample drift.** Exemplary drift of the sample as determined by the position of the surface. The motion is indicated by a moving average over 20 consecutive measurements (red line), that relates to 30 s. A stable measurement, as presented, typically relates to a movement in z direction of about 40 nm in 22 minutes. However, as it can be seen, (thermal) fluctuations randomly cause faster and slower moving of the sample.

depth from the data by fitting (see section 5.1.2). Each measurement run was performed along the z-axis over a total distance of $2\,\mu$m with a step size of 10 ± 0.2 nm between each pixel, and a count time of 10 ms. The improvement of the precision can then be illustrated by averaging adjacent measurement runs into one binned measurement and recalculating the standard deviation. The analysis of exemplary measurements is shown in figure 6.3.

One can see a steadily improving precision (that is a smaller standard deviation). The fitting procedure shows a standard deviation of about 18.0 nm for a single measurement. This value drops for increasing measurement time with a square root behavior till a binning of 500 measurements. At this time an optimal precision of about 0.9 nm is achieved. For longer measurement times any further improvement is suppressed by drift effects and noise.

Concerning the noise sources, one can estimate the error for the fitting procedure. The collection of about 60000 photons (at a SNR of about 6), after subtraction of the background fluorescence, gives an expected precision of 4 nm that can be solely related to photon shot noise (under the assumption of an uncertainty of the PSF of $1\,\mu$m along the optical axis). As a consequence we can assume that discussed drift effects are responsible for a more than three-times higher error than the photon shot noise. As we see in the data as presented in figure 6.3 the results still show statistical behavior of the precision until the limit at 500 measurements is reached. For that reason, one can assume, that until this point, the drifts occur random-like around a certain position.
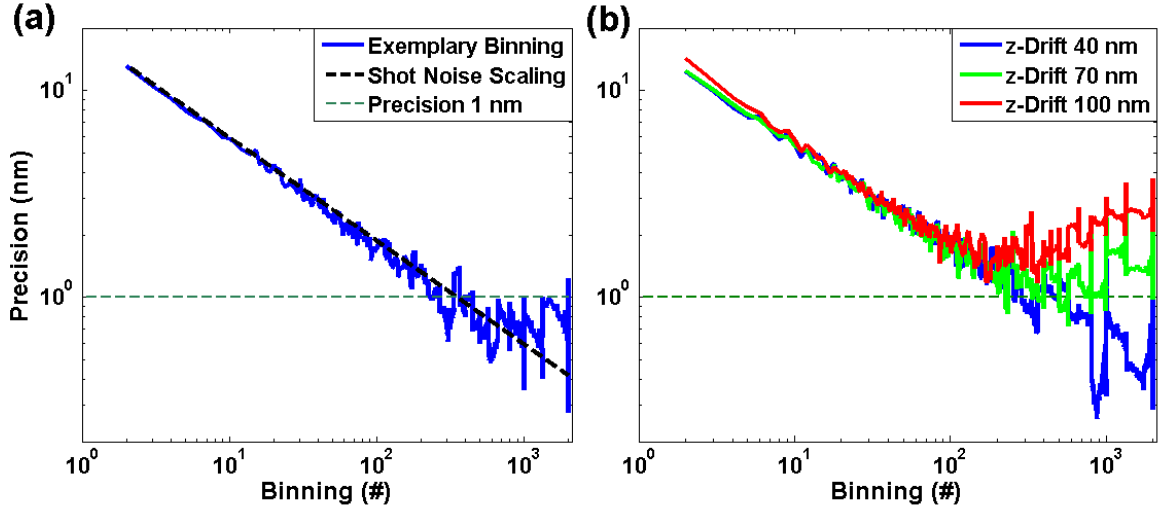
Figure 6.3: **Determination of the shot noise limit of the measurements.** (a) The binning of the measurements of the virtual depth shows a steadily decreasing standard deviation with shot noise scaling. The limit is reached at about 0.9 nm for 500 measurements. The highly wavering behavior of the standard deviation for high binning numbers can be explained by the limited amount of measurements as the total number of measurements is not perfectly divisible by the binning number. The volatility is exaggerated due to logarithmic scaling. (b) Higher drift effectively reduces the achieved precision. Here, three exemplary measurement runs compare a typically stable measurement with a total drift of 40 nm (blue) to occurred higher drifts of 70 nm (green) and 100 nm (red).

6.2 Measuring the Effective Focal Shift

The measurements of the virtual depth show a high precision, as stated in the previous section. Consequently, one expects a strong linear dependence of the maximum positions of the fluorescent PSF and the reflected cPSF since these are the two values of which the virtual depth VD is calculated. As already discussed in section 5.2.2, the measured values should show a correlation different from the factor 1 due to the high optical pathlength in diamond. This behavior can be experimentally confirmed. Figure 6.4 presents two exemplary correlations of the two maximum signals.

The slope can be calculated by a linear regression. In this representation the focal shift s is then given by the reciprocal value of the slope. However there is a relatively high uncertainty in the calculation of s since the initial uncertainties of our measurement values are in the same order of magnitude as the random drift effects that cause the correlation. The total error of s for our measurements typically shows values between 0.3 to 0.4 respectively a relative error around 20%. As it will be shown in section 6.3,
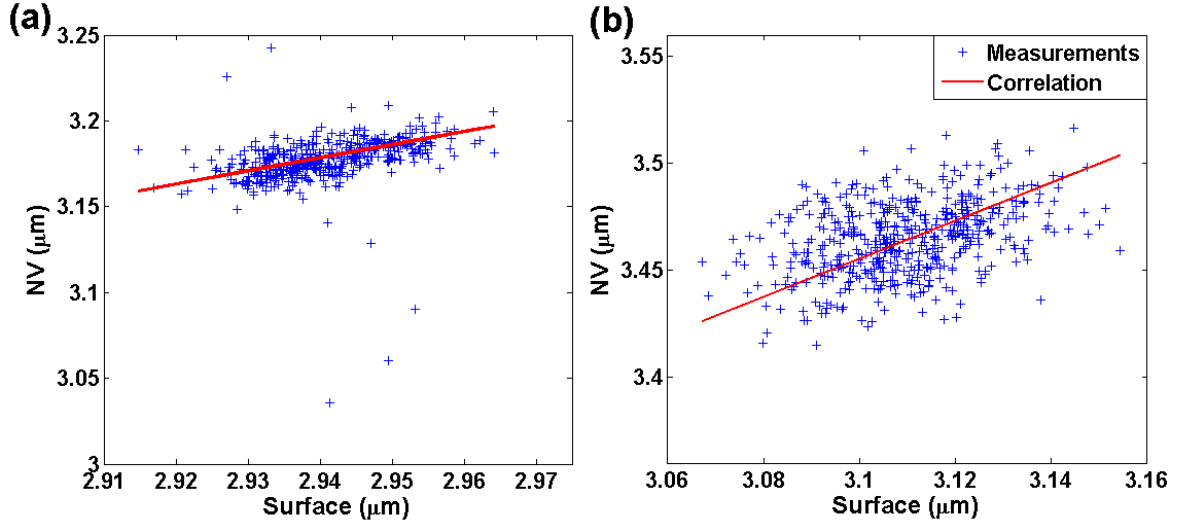
Figure 6.4: **Measured focal shift correlation.** The maximum positions of the reflected light from the surface and the fluorescent light of the NV center show a strong linear correlation that differs from 1. Here, two exemplary NV centers are presented, that show a slope of (a) 0.76 at an average position difference of $236 \pm 1\,\text{nm}$ and (b) 0.45 at an average position difference of $355 \pm 1\,\text{nm}$. In this depiction, the focal shift s is then given by the reciprocal value of the slope.

this uncertainty plays a major role for the accuracy of the depth determination for deep NV centers.

The calculated shift factors of the single NV centers can then be compared to their virtual depths. Referring to the discussions in section 5.3, we expect an increasing shift for deeper emitters. Figure 6.5 illustrates the results that confirm the theoretical expectation. A tendency of a steadily increasing focal shift for deeper NV centers can be seen. This corroborates the assumption of the depth dependency of the focal shift.

The calculated model from section 5.3, which is based on a combination of raytracing and wave optics, seems to predict the focal shift of our measurements in good agreement and has been added to the diagram. Note that the calibration c (see section 6.3.1) and the calculated values of the focal shift s have been used for the graph, to provide a good comparability to the virtual depth. As shown, the behavior of the curve starts at a value around 1.3 for shallow implanted NV centers and steadily increases. For deep NV centers, one expects a modeled boundary value for the focal shift of 2.9 as an upper limit in this experimental configuration. These results are in agreement with basic geometrical optics models such as presented in [202]. As already discussed in section 5.3, it is important to note that the effective focal shift is mainly dependent on the numerical aperture of the microscope.
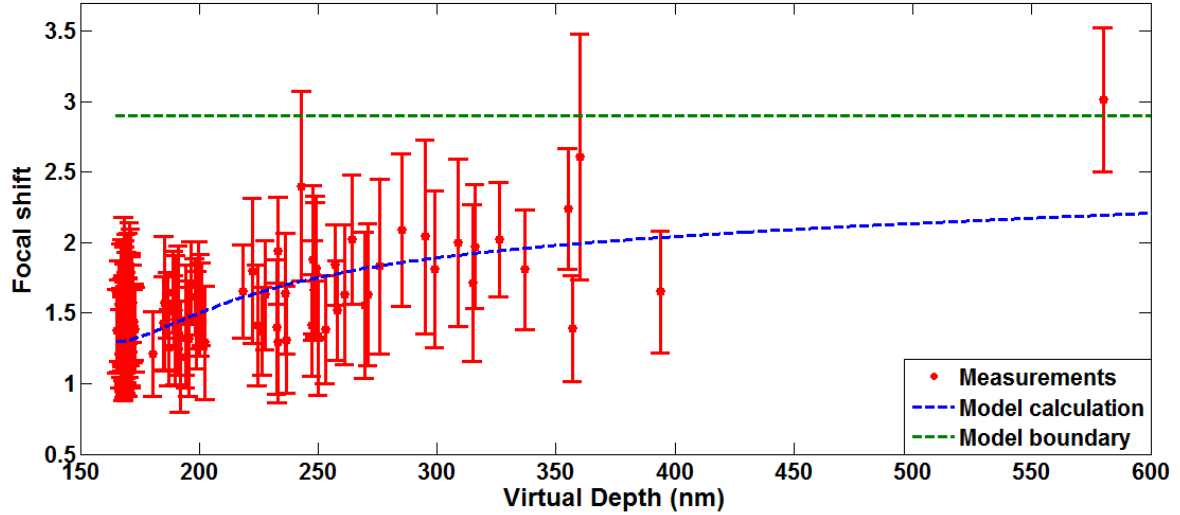
Figure 6.5: **Focal shift and virtual depth.** Shallow implanted NV centers show a position difference of about $170 \pm 3\,\text{nm}$ at a minimal shift factor of 1.3 ± 0.3, whereas deeper NV centers show the tendency of a steadily increasing focal shift. This is in good agreement to the theoretical prediction. The dashed lines compare the evaluated values to the calculated model in section 5.3 (blue) and its predicted boundary value of 2.9 for deep emitters (green).

6.3 Total Resolution of the Experiment

This section closes this chapter with the final results of the depth measurements. Using the shallow emitters for calibration, it is possible to determine the depth of deeper NV centers, as well as giving an estimation of the achieved accuracy of the measurements.

6.3.1 Calibration with Shallow Emitters

As discussed in section 5.2.3, the value of c was calibrated by finding the lower limit of the virtual depths in a sample of shallow implanted NV centers. The calibration was done with a type IIa, chemical vapor deposition (CVD) grown diamond. The NV centers were produced by nitrogen implantation with an energy of $2.4\,\text{keV}$. It can be confirmed by NMR measurements that such NV centers are in fact placed only few nanometers deep from the surface [63] [181]. The investigated NV centers were located in one single implantation spot as shown in figure 6.6.

In total, 101 NV centers have been evaluated with a sufficient precision of about $1\,\text{nm}$. The distribution of virtual depths of this ensemble shows a lower boundary at $165.3 \pm 1\,\text{nm}$. As a consequence, we take the value of $165\,\text{nm}$ as the calibration shift c. Using the determination of the focal shift s, we can then calculate the real depth z_0 of the NV centers from equation 5.1. The resulting depth distribution of the shallow NV centers is shown in figure 6.7.
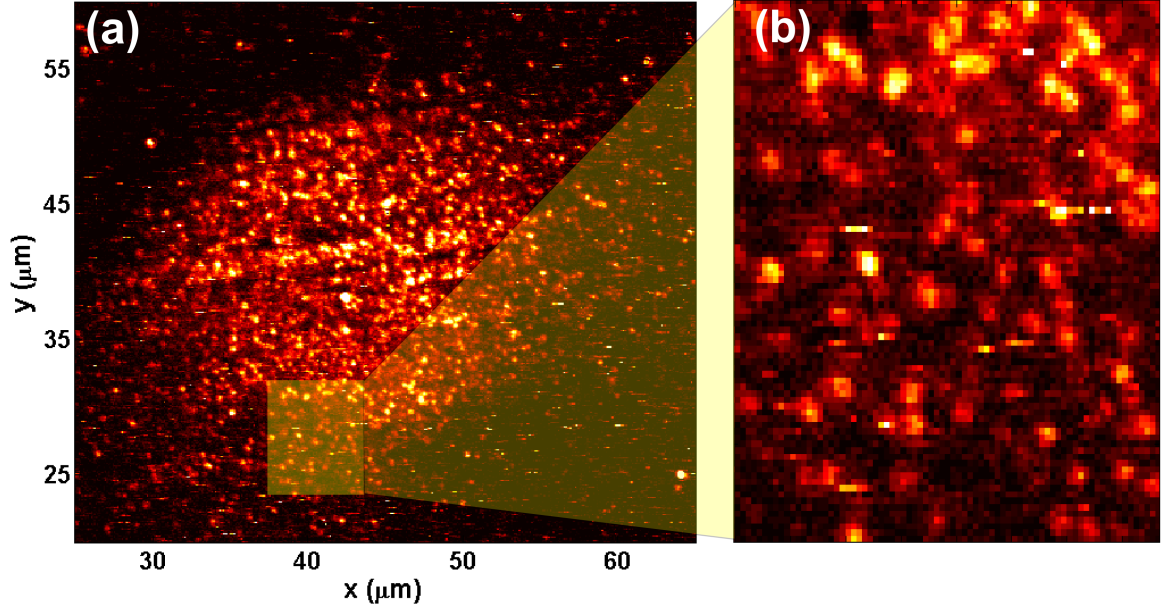
Figure 6.6: **Implantation spot of shallow NV centers.** (a) Calibration measurements were performed on an implantation spot of shallow NV centers with a nitrogen implantation energy of 2.4 keV. (b) A zoom shows single NV centers, that are clearly separated from their neighbors and could be addressed by individual measurements.

Additionally, the results of a stopping and range of ions in matter (SRIM) simulation [204] have been included to the diagram of the measured depths. As it can be seen, both experimental and simulated values show a good agreement. The peak of the measured depth distribution at 6.3 ± 2.9 nm is slightly shifted to deeper values in relation to the simulated values, that lie around 4.7 ± 1.9 nm. The uncertainties of the estimated calibration c and the shift factor s, which are both used to calculate z_0, are one thinkable reason for this difference. Other reasons are statistical effects since 101 NV centers might not be enough to accurately determine the whole distribution, or the reliability of the SRIM calculations, which does not necessarily calculate the exact depths.

6.3.2 Results for 50 keV Implantation

As a second sample, we used a type IIa, high-pressure high-temperature (HPHT) grown diamond and NV centers with a nitrogen implantation energy of 50 keV. 49 NV centers have been evaluated with the determined calibration constant c and their focal shift s. The results for these deeper emitters, as well as the corresponding SRIM calculation, are depicted in figure 6.8.

Here, the SRIM calculation shows a depth distribution of 63 ± 15 nm and matches the peak of the measured depth distribution, which averages around 72 ± 23 nm. In
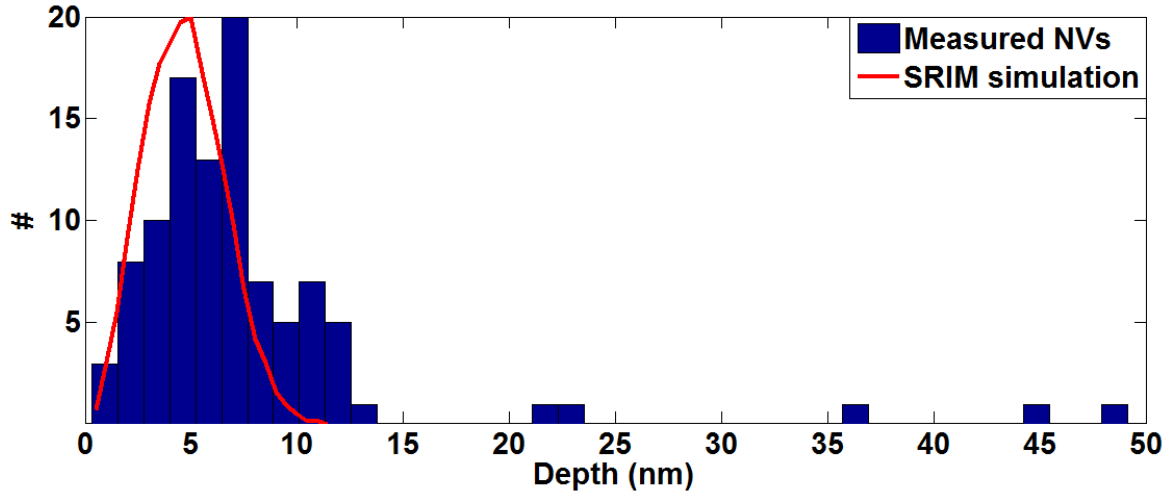
Figure 6.7: **Depth distribution of 101 shallow implanted NV centers.** The distribution for an implantation energy of $2.4\,\mathrm{keV}$ shows a peak at $6.3 \pm 2.9\,\mathrm{nm}$. It follows the SRIM simulation for implanted nitrogen (red line), that shows slightly lower depths with an average of $4.7 \pm 1.9\,\mathrm{nm}$.
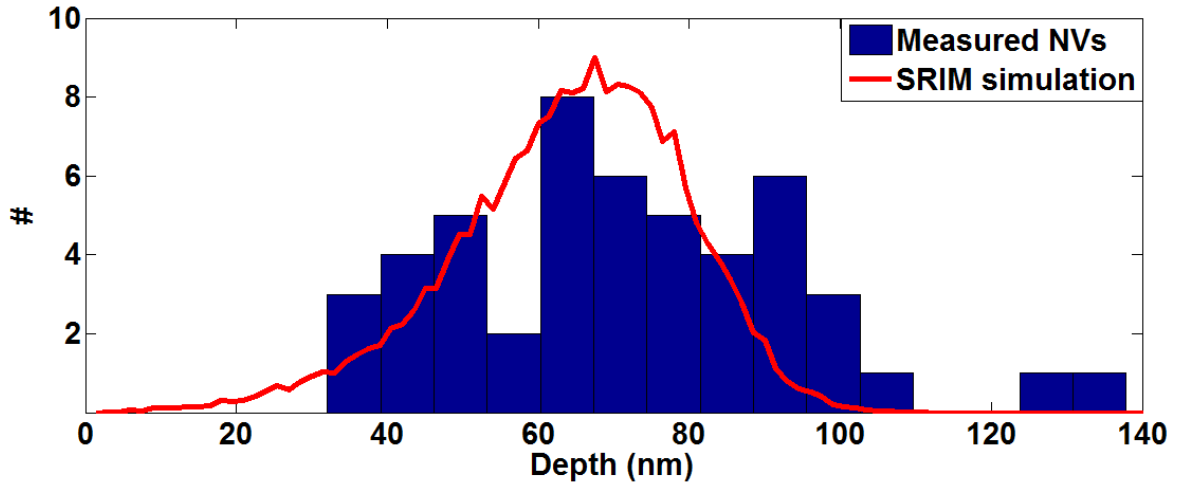

Figure 6.8: **Depth distribution of 49 NV centers with an implantation energy of $50\,\mathrm{keV}$.** The distribution around $72 \pm 23\,\mathrm{nm}$ is in good agreement to the SRIM simulation, that shows a peak around $63 \pm 15\,\mathrm{nm}$ for implanted nitrogen. The measured shift towards deeper values might indicate channeling effects.

comparison to the simulation, the measured depths show a slightly broader distribution which can be assumed to be partially dependent on the error of our measurements.

Moreover, a significant proportion of deeper outliers measured in the depth profiles can be noticed. This effect possibly indicates the effect of channeling [205], that is assumed to occur during ion implantation and produce a higher ratio of deeper NV centers than expected.

6.3.3 Estimation of Accuracy
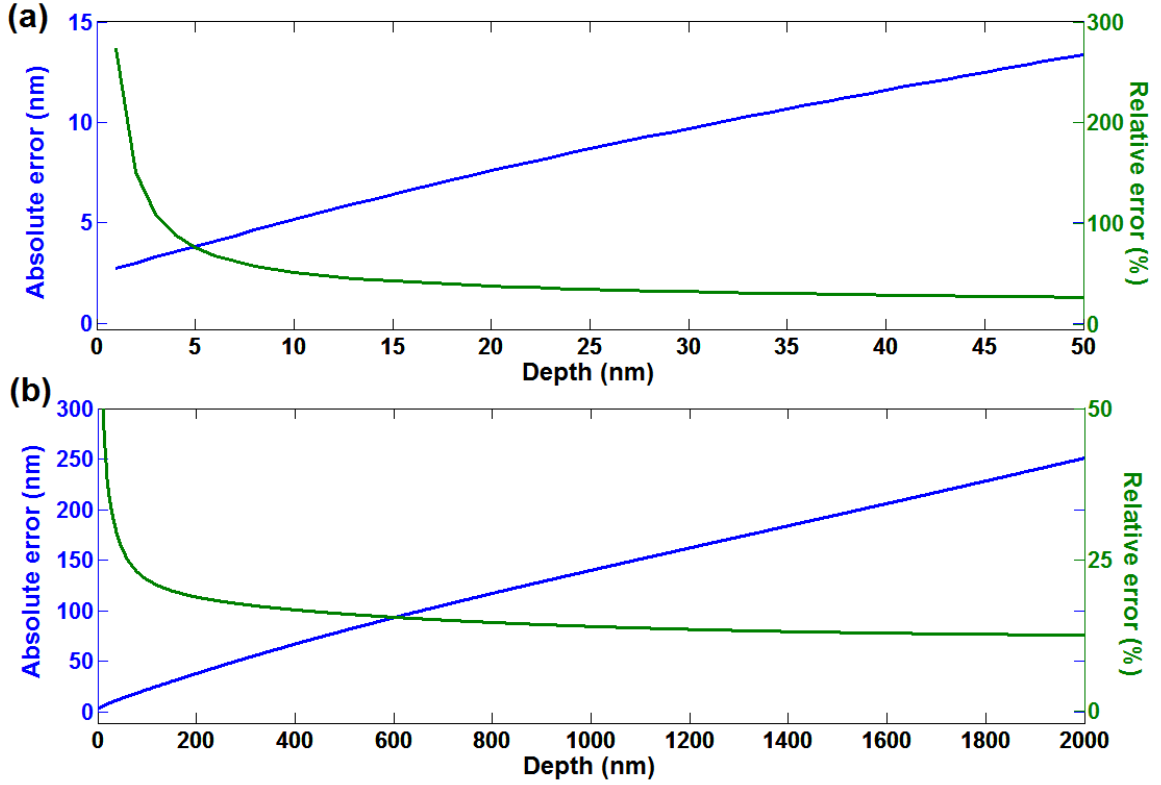
Figure 6.9: **Absolute and relative error of depth measurements.** The calculation of the total maximum error for (a) shallow and (b) deeper NV centers shows a total accuracy significantly better than the diffraction limit. Though measurements for emitters close to the surface suffer from a high relative error, this value keeps constantly decreasing for larger depths.

The performed experiments, both on shallow NV centers near the surface and NV centers with a depth in the range of about 70 nm, show a good agreement to the theoretical expectations given by SRIM calculations for implanted Nitrogen. All the same, the final question to be resolved addresses the accuracy, that can be assigned to our experimental data.

A feasible approach is a simple error calculation. Referring to equation 5.1, which was

used to calculate the real depth z_0, we can calculate the total maximum error Δz_0 by

$$\Delta z_0 = s \cdot \Delta VD + s \cdot \Delta c + \Delta s \, (VD - c) \ . \tag{6.1}$$

As it can be seen, the uncertainties of the experimental parameters ΔVD, Δc and Δs have a different impact on the total uncertainty in relation to the measured values VD, c and s. According to our given values, this results in an estimated error of about 2.6 nm for shallow NV centers. Though this value looks very promising compared to the diffraction limit, one has to take into account, that this relates to a relative error of about 100%. A comparison of absolute and relative error referring to equation 6.1 is given in figure 6.9.

For deeper NV centers, the absolute error increases, however, the relative error keeps steadily decreasing. This can be explained, since for deeper NVs the error of the depth localization becomes more sensitive to the uncertainty in the shift factor s, but not to ΔVD and Δc. According to our model, the latter two parameters show no depth dependence. Nevertheless, we can conclude that we have demonstrated the absolute accuracy of our localization technique in the regime of few nanometers by a purely optical approach.

6.3.4 Measuring under Unfavorable Constraints

The final part of this section is dedicated to a fast application of the presented method with sufficient accuracy. For some experiments, like coupling the NV center to a cavity [206] or the application of solid immersion lenses [207], the determination of the position of an emitter is sufficient with the accuracy of only about a hundred nanometers. Hence, it is not necessary to push all uncertainties to the minimum. Here we will sketch the influence of a lack of precision in the measurements due to, what we call, unfavorable constraints.

As already seen in equation 6.1, the uncertainties of the three experimental parameters play a very different role in affecting the accuracy of the experiment. This trait is graphically captured in figure 6.10. Here, the behavior of the total uncertainty for an increase in ΔVD, Δc and Δs is illustrated, depending on the depth of the emitter.

One can state the following observation: The deeper the NV center one intends to measure, the less important are uncertainties in c and VD. Thus, any noise effects that influence e.g. the quality of the fitting, do not play a major role. In this regime, one can wisely take longer measurement times and accept a certain averaging effect for the estimation of the virtual depth. Even an increase of the uncertainty up to 10 or more nanometers is not necessarily a problem - of course depending on the required total accuracy. Concerning the calibration constant c, the estimation of error is less easy. A calibration measurement as performed in this work takes a lot of time and effort to gain enough statistical data. One could think of markers at the surface like fluorescing nanodiamonds or quantum dots to calibrate the surface position at least in a regime of tens to hundred nanometers. Even better is the possibility to use shallow NV centers for spin sensing. These NMR technique will provide a very accurate option to calibrate
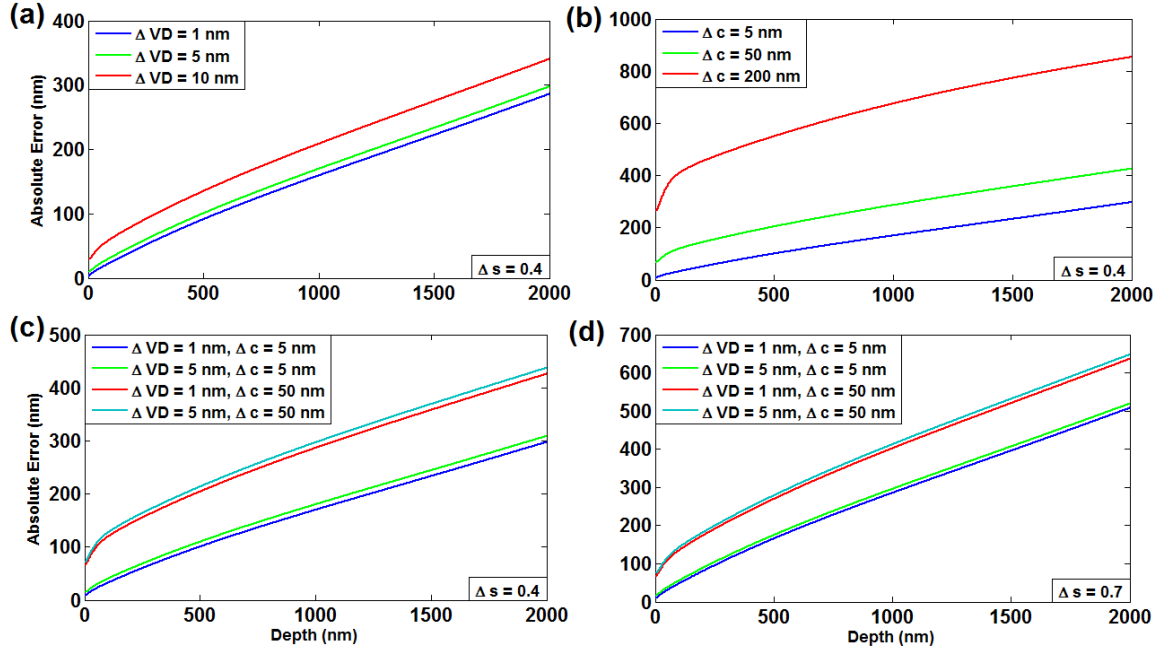
Figure 6.10: **Error in case of unfavorable constraints.** A higher error of the experimental parameters affects the total error in different ways. A variation of (a) ΔVD (with $\Delta c = 1\,\text{nm}$) or (b) Δc (with $\Delta VD = 1\,\text{nm}$) gives a different basic offset for the accuracy. On the contrary, the uncertainty of the focal shift Δs relates to the rapidity of increase for the absolute error. This can be seen, when comparing different error evolutions in case of (c) $\Delta s = 0.4$ to (d) $\Delta s = 0.7$.

the surface position (see also the next chapter) [63].

However, deep NV centers are much more sensitive to the uncertainty of the focal shift Δs. Our measurements have shown that it is possible to experimentally determine the value of s to an accuracy of about $\Delta s = 0.4$. However, these measurements require long measurement runs and still show a pretty high error confined in the data, since it overlaps with the uncertainties of the position estimation. In this case, we suggest to take the model calculations performed for s in section 5.3. The model seems to achieve a sufficient precision compared to the measurements. Even if one expects slight errors, we are confident, that our theory predicts the value of s with at least the same quality of uncertainty as our performed measurements.

7 – Magnetic Sensing in Liquids by Single NV Centers

NV centers, that are located near the surface, have been proven to be a valuable resource to measure magnetic field fluctuations [62] [208] [209]. Therefore, this last chapter entwines the determination of depth with an exemplary application of single NV centers to magnetometry. This is an important task, e.g. for nanoscale biology, where the investigation of magnetic field fluctuations could give insight into fundamental mechanisms of biochemical reactions and processes [171] [210]. So far, ensembles of NV centers have successfully shown their capability of detecting dissolved spins in a liquid [211] [212]. Here, we prove the principal applicability to single NV centers.

The overall objective of the experiment was not limited to the localization, but to develop a functional method for the utilization of single NV centers to physiological spin detection. Therefore, the first section of this chapter will give a description of the diamond and the microfluidic device, that have been specifically created for the experiments. The second section then covers the proof of principle experiments, that precisely confirm the shallow position of the NV centers by their interaction to the environment. Concretely, this is done by the detection of proton spin noise in oil, as well as by measuring the coherence times of single NV centers, that interact with manganese spins in an aqueous solution.

7.1 Preparation of the Microfluidic Channel with NV Centers

For the experiments we used a 99.99% ^{12}C diamond layer, homoepitaxially grown with a thickness of $\sim 70\,\mu$m on a high purity, single crystal substrate. The microfluidic channel was fabricated in the overgrown diamond layer with a high power, pulsed, frequency doubled Nd:YAG laser. In order to seed the fabrication process, a 10 nm thick layer of absorptive gold was first evaporated on the diamond surface, since gold absorbs the 532 nm laser more efficiently than pure diamond, thereby nucleating graphitisation of the underlying diamond. After boiling the diamond in triacid (1:1:1 mixture of H_2SO_4:$HClO_4$:HNO_3) at $180\,°$C for 10 hours, the diamond was treated with a hydrogen plasma at $800\,°$C under a pressure of 30 mbar and a flow rate of 30 sccm for 20 minutes. Figure 7.1 shows a scanning electron microscope image of the resulting channel, directly after laser cutting, with a width of $90\,\mu$m and a depth of $35\,\mu$m. Furthermore a brightfield microscope image of the diamond is shown, taken before and after plasma treatment, showing removal of dark graphitised diamond after plasma treatment.

To create shallow NV centers for nanoscale magnetometry applications, and in order to characterise the diamond surface, ^{15}N$^+$ ions were implanted into the laser-cut channel. Two implantation energies of 2.5 keV and 5 keV were chosen [213] resulting in a depth
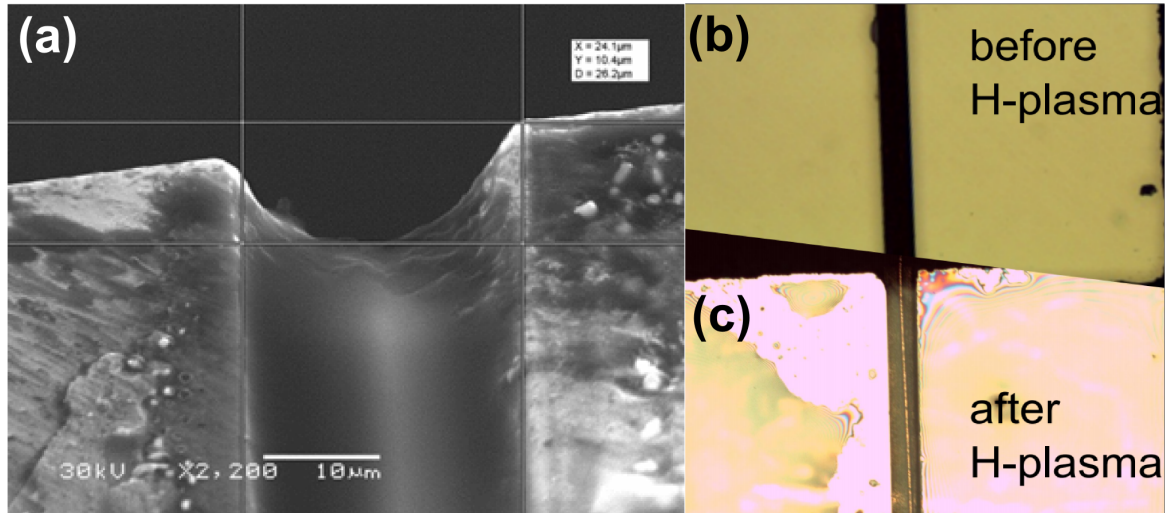
Figure 7.1: **Diamond sample with channel.** (a) Scanning electron microscope image of the sample directly after laser cutting. The measurements of the channel show a width of $90\,\mu$m and a depth of $35\,\mu$m. (b) The dark surface of the diamond in the brightfield microscope image indicates graphitisation. (c) The layer of graphite can be successfully removed by plasma cleaning and leave a clean diamond surface.

range of 2–5 nm and 7–10 nm respectively below the surface. The diamond was then annealed at $800\,°$C for 1 hour in a vacuum of 5×10^{-6} mbar, and subsequently acid boiled for a second time under the previous conditions. As shown by imaging in an area near the edge of the high dose region, single implanted NV centers could be observed (see figure 7.2). To confirm the observed NVs indeed are due to shallow implanted NV centers, we observed the ^{15}N hyperfine spectrum by optically detected magnetic resonance spectroscopy.

For the proper delivery of the liquid to the implanted NV centers, the diamond sample was glued onto a microscope slide, with two solid polydimethylsiloxane (PDMS) strings to close the channel to the diamond and serve as future space for liquid transportation. The whole construction was put into liquid PDMS and heated at $60\,°$ C for 12 hours. The process leaves an imprint of the diamond and the strings in the now solid PDMS with two entrances to push liquid through the channel. The size was cut to fit on a cover slip and two holes on each side have been drilled through the PDMS from the top.

Now, the whole chamber could be put together to form a microfluidic transport system as mentioned in section 3.2.2. First, a copper wire with a diameter of $25\,\mu$m was placed on a cover slip and the diamond was put onto the wire such that the wire was lying in the etched channel. After that, the PDMS imprint was put on top to fix all. The whole device was pressed together by a metal weight and heated to $60\,°$C for 10 min. The holes at the edge of the imprint, that have been left by the strings, were sealed with a two-component adhesive. Thin steal tubes of a diameter of 0.5 mm were plugged into
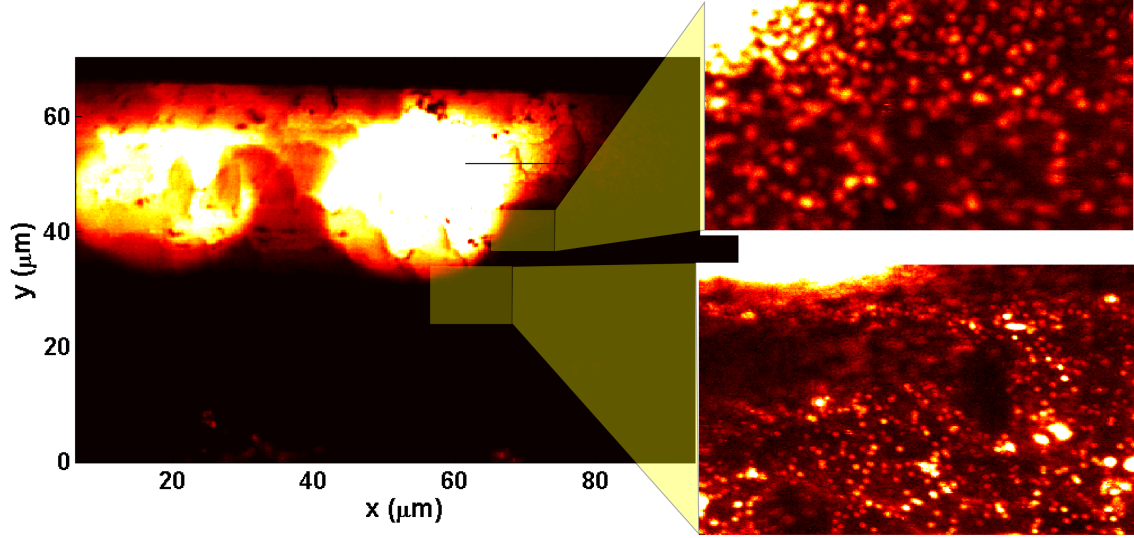
Figure 7.2: **Region of implanted NV centers.** The confocal scan shows 2 of 4 implantation spots. The high fluorescence indicates an ensemble of densely packed NV centers in these areas. Since all measurements were intended to be performed on single NV centers, a region near the implanted spot was investigated. The two zoomed pictures shows the location of single NV centers that lay scattered around the main area of the implantation circles and can be addressed by individual measurements.

the drilled holes on the top and connected to tubes. The resulting device can be seen in figure 7.3.

To float the channel with liquid, the needle of a syringe was connected to the end of one tube, whereas the end piece of the second tube was placed into liquid. By slowly pulling at the syringe, liquid was floating through the channel. To prevent unnecessary losses of fluorescence due to the liquid in the channel the sample was imaged with a water objective (see section 3.2.2).

An additional magnet stage was placed above the setup to enable proper alignment of the external magnetic field. With this configuration it was possible to measure the effect of spins in the liquid on the coherence times of NV centers. The results are shown in section 7.2.
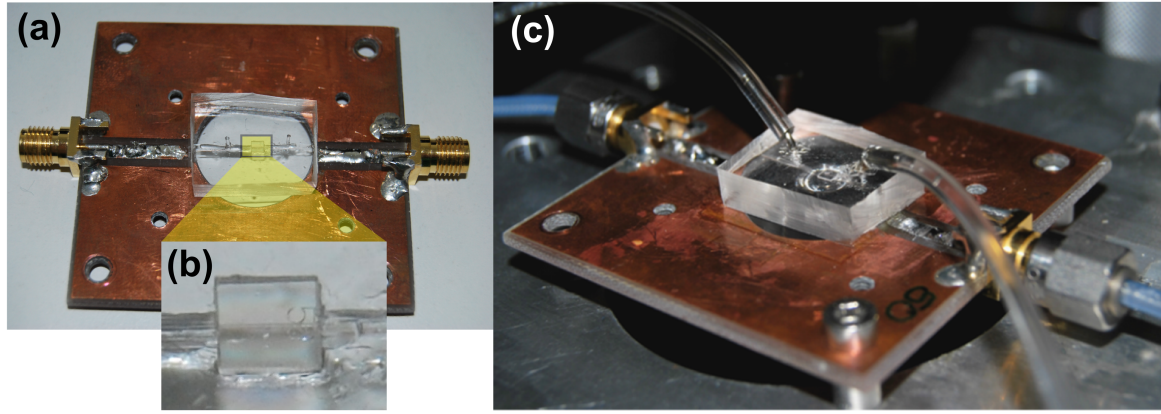
Figure 7.3: **Complete microfluidic transport system.** (a) The prepared microfluidic device can be glued on top of a sample holder. (b) The diamond sample was sealed in the PDMS by adhesive forces. Drilled channels provided the possible supply of liquid to the diamond, whereas the wire for the microwave signals had been placed directly in the resulting canal. (c) The sample holder could be fixed to the stage of the home-built confocal microscope, directly above a water objective. The plastic tubes for the liquid transport are fixed by small metal plugs to the whole construction.

7.2 Spin Sensing Experiments

7.2.1 Proton Spin Noise in Oil and Depth Determination

A first characterization of the implanted NV centers was performed by noise spectroscopy measurements (see section 2.2.3). The xy8-K pulse sequence enables to determine fluctuating fields that interact with the NV center. By this method, it is possible to determine the depth of the NV centers for implantation depths up to 20 nm [63] [181]. Furthermore, successful measurements will prove, that the NV centers can be potentially applied to different noise sources, like radicals in the liquid.

For these preliminary measurements, the sample was imaged by an oil objective without the microfluidic chamber. The immersion oil contains hydrogen atoms, that give a high proton density ρ of $50\,\mathrm{nm}^{-3}$ on the diamond surface. First, an applied magnetic field of about 500 Gauss can be determined by an ODMR measurement of the NV center. Then, the microwave power can be adjusted by a Rabi experiment, to calibrate the right timing for the required π respectively $\frac{\pi}{2}$ flips of the pulse sequence. An exemplary measurement is shown in figure 7.4.

The magnetic field will lead to a defined Larmor frequency of the protons, that interact with the defect. Since this interaction takes place in the weak coupling regime, where the coupling is dominated by interaction between individual hydrogen spins, the resulting magnetic signal originates from magnetic field fluctuations $\langle \Delta B^2 \rangle$ of randomly polarized spins [63].
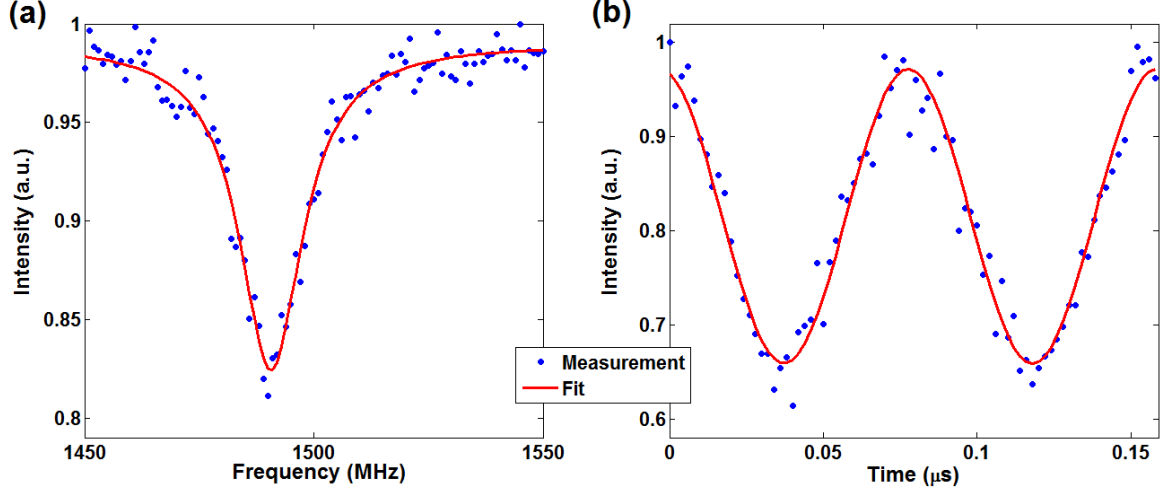
Figure 7.4: **Measured ODMR and Rabi oscillation.** (a) The Lorentz fit of the ODMR signal shows a dip at 1490.7 MHz, that relates to an aligned magnetic field of 493 Gauss. (b) The power of the microwaves can be adjusted, such that the Rabi frequency will show the desired period of 80 ns.

This relates to the power spectral density around the Larmor frequency as follows:

$$\left\langle \Delta B^2 \right\rangle = \int\limits_{-\infty}^{\infty} S\left(\omega\right) \mathrm{d}\omega \ . \tag{7.1}$$

Figure 7.5 shows two exemplary xy8-16 measurements and their related noise spectra, that have been calculated by deconvolution with the filter function (see section 2.2.3). The intensity dip in xy8-16 intensity signal relates to the resonance of the Larmor frequency of the proton spins, and consequently, to a detectable signal in the noise spectrum.

According to literature [63] [181], the depth of the NV centers can then be calculated as follows: Assuming a proton with the nuclear spin operator $\hat{I}_i$ and the magnetic moment $\mu_p = \hbar \gamma_p$ at the distance r_i to the NV center, the induced magnetic field B_z along the NV axis denotes as

$$B_z\left(r_i\right) = \frac{\mu_0 \mu_p}{4\pi r_i^3} \left[\left(3n_z^2 - 1\right) \hat{I}_{i,z} + 3n_z \left(n_x \hat{I}_{i,x} + n_y \hat{I}_{i,y}\right) \right] \ , \tag{7.2}$$

whereas the variance is given by

$$\Delta^2 B_z\left(r_i\right) = \left(\frac{\mu_0 \mu_p}{4\pi r_i^3}\right)^2 \left[\left(3n_z^2 - 1\right)^2 \left\langle \left(\hat{I}_{i,z}\right)^2 \right\rangle + 9n_z^2 \left(n_x^2 \left\langle \left(\hat{I}_{i,x}\right)^2 \right\rangle + n_y^2 \left\langle \left(\hat{I}_{i,y}\right)^2 \right\rangle\right) \right] . \tag{7.3}$$
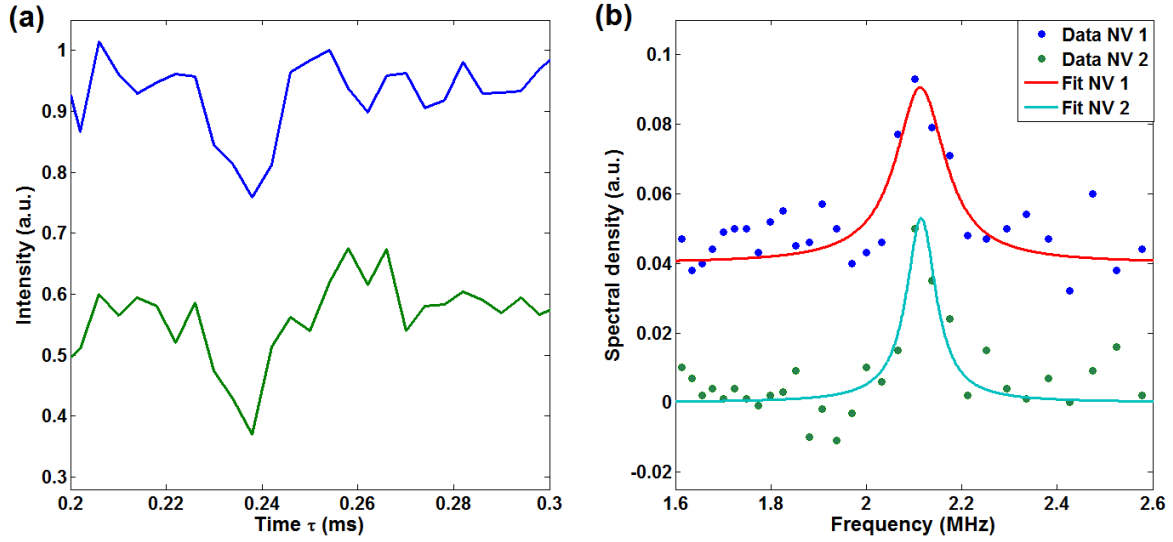
Figure 7.5: **Measurement results of two xy8-16 sequences and their related noise spectra.** (a) The applied xy8-16 pulse sequences for two different NV centers shows an intensity dip at a delay time of 0.238 ms, that relates to the Larmor frequency of the proton spins in the applied magnetic field of 493 Gauss. (b) The depth can then be determined to 5.5 ± 0.5 nm (blue) and 6.0 ± 0.5 nm (green) by integration of the noise spectra, whereas the fitting function is given by a Lorentzian. Note, that both measurements have been relatively shifted for illustrative purposes.

Assuming a random hydrogen spin orientation, and thus $\left\langle \left(\hat{I}_{i,j} \right)^2 \right\rangle = \frac{1}{3} s \left(s + 1 \right) = \frac{1}{4}$ with the spin quantum number $s = \frac{1}{2}$, one derives

$$\Delta^2 B_z^{\parallel} = \rho \frac{\left(\mu_0 \mu_p \right)^2}{64 \pi^2} \int\limits_0^{\pi/2} \int\limits_0^{2\pi} \int\limits_{z_0 / \cos \theta}^{\infty} \left(3 n_z^2 - 1 \right)^2 r^4 \sin \theta \mathrm{d}r \mathrm{d}\theta \mathrm{d}\phi \tag{7.4}$$

for the parallel component $\Delta^2 B_z^{\parallel}$ of the field fluctuations in relation to the NV axis for a depth z_0. With a tilt of the NV axis by $54.7°$ with respect to the surface normal, equation 7.4 integrates to

$$\sqrt{\langle \Delta B^2 \rangle} = \sqrt{\frac{5}{1536\pi}} \mu_0 \mu_p \sqrt{\frac{\rho}{z_0^3}} \ . \tag{7.5}$$

Consequently, according to equation 7.1, the depth of the NV center is related to the spectrum of the magnetic field fluctuations.

Exemplary results of our measurements are shown in figure 7.5. In total, the proton spin noise was successfully measured for 11 NV centers by xy8 pulse sequences with a

calculated average depth of 5.4 ± 1.9 nm. The results prove the proximity of the defects to the surface as well as their sensitivity to external magnetic field fluctuations. Thus, the next two sections investigate the effect of external spins in combination with the microfluidic chamber by measuring the coherence time of the NV centers.

7.2.2 Manganese Spin Sensing by Spin Lattice Relaxation Time T_1 Measurements

The first experiments, that have been performed with the microfluidic channel, determine the spin-lattice relaxation time T_1. Three different liquids (water, isopropyl alcohol and diluted manganese chloride) have been used to show the sensitivity of the coherence of the NV centers to the environment in the channel. In case of the manganese spins, this can be used to successfully determine the spin sensitivity of individual NV centers as well as their depths.

Obviously the interaction of NV centers to spins outside the diamond is dependent on the depth. The lower the distance to the surface, the higher is the spin sensitivity of the NV center. The power of sensitivity can be described by the detection volume as illustrated in figure 7.6. For a given depth z_0 the number of detected spins N is given by [209]

$$N = \frac{4}{3}\pi n z_0^3 \tag{7.6}$$

with the spin density n.
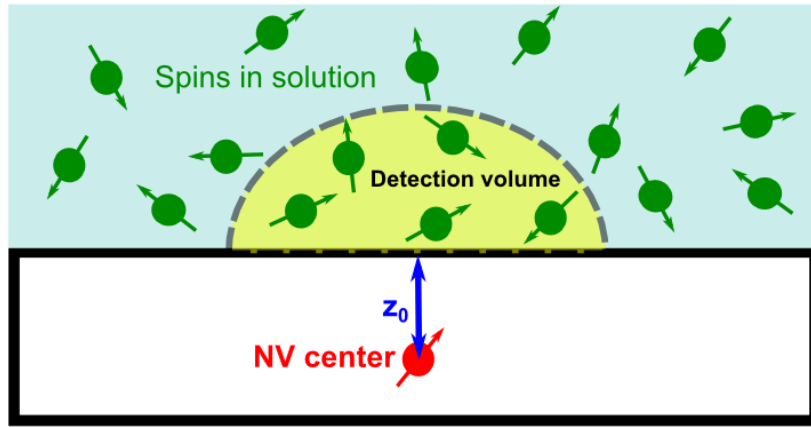
Figure 7.6: **Detection volume of a NV center.** The main contribution to the interaction can be related to the spins, that are closest to the NV center. Due to the r^{-3} dependency of the interaction, this ratio is attributed to less and less spins, resulting in a very sensitive measurement for shallow NV centers.

Due to the r^{-3} behavior of the dipole-dipole interaction the total contribution of the interaction is mainly defined by the nearest spins to the NV center. All in all this leads

to the some-how counterintuitive definition of the detection volume that gets smaller for a position nearer to the surface. However, this makes sense since the detection volume does not give the absolute volume in which spins are detected but the volume that gives the main relative contribution to the interaction.

Since the spins will contribute to a perturbation of the magnetic field, it is to be expected that they will cause a faster decay of the coherence of the NV centers. The decay of the NV state coherence $D(t)$ in time can be described by an exponential decay such as

$$D(t) \sim \exp(-\Gamma \cdot t) \tag{7.7}$$

Here the decoherence rate Γ can be directly related to the coherence time T_C by $\Gamma = T_C^{-1}$. In case of two noise sources with different decoherence rates, one can assume the total effect to be the sum of both:

$$\Gamma_{total} = \Gamma_1 + \Gamma_2 \tag{7.8}$$

This can be applied to the experiment by calibration measurements to cancel out all other environmental effects on the coherence time. In case of the spin-lattice relaxation time T_1 it is possible to determine the effective magnetic field variance $\langle B_i^2 \rangle$ caused by the species i by [212]

$$\left\langle B_i^2 \right\rangle = \frac{21 \cdot 10^6 \pi c N_A}{16 z_0^3} \left(\frac{\mu_0 \hbar}{4\pi} \tilde{\gamma}_{NV} \tilde{\gamma}_i \right)^2 . \tag{7.9}$$

with the spin concentration c, the Avogadro constant N_A and the magnetic permeability of the vacuum μ_0. $\tilde{\gamma}$ refers to the gyromagnetic ratio of the NV and the spin species divided by 2π. The decoherence rate is approximately defined by

$$\Gamma_i \approx \frac{f_i \left\langle B_i^2 \right\rangle}{f_i^2 + D^2} \tag{7.10}$$

where f_i denotes the zero-mean fluctuations of the spins i ($f_{Mn} \approx 100\,\text{MHz}$ [214]) and $D = 2.87\,\text{GHz}$ is the zero-field-splitting of the NV center. With this set of equations, it is possible to convert T_1 times into an effective magnetic field and calculate the depth of the NV center respectively the number of spins, that have been sensed in average.

Measurements confirmed the sensitivity of the NV centers to different liquids by a significant drop in the coherence times. For water, 10 different NV centers showed an average coherence time T_1 of $341 \pm 117\,\mu\text{s}$. In case of isopropyl alcohol, one observed an average decrease of T_1 by a factor of 3.3 ± 1.8, whereas the effect of Manganese spins (diluted MnCl_2 solution with a concentration of $0.2\,\text{mol/l}$) has been considerably larger with a factor of 10.3 ± 7.3. Figure 7.7 shows the results for two exemplary NV centers.

The high standard deviation of the results is believed to be specifically dependent on different depths of the NV centers. The effects of isopropyl alcohol have only be qualitatively evaluated and were not used for further calculations. According to equations 7.7 to 7.10, the Manganese spin measurements resulted in a calculated average depth of $3.5 \pm 1.4\,\text{nm}$ and is lower compared to the results, that have been achieved for the
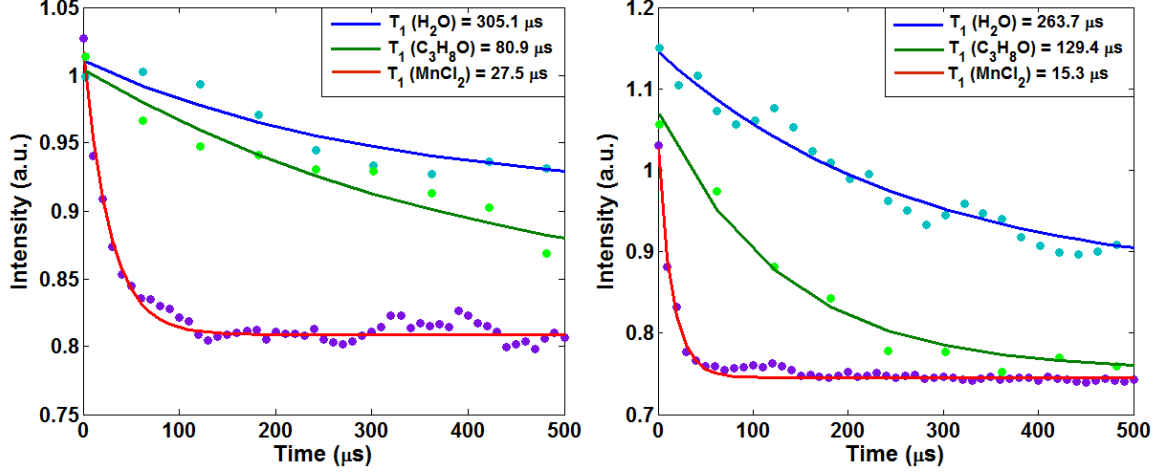
Figure 7.7: **Spin lattice relaxation related to different liquids.** Water, isopropyl alcohol and diluted manganese chloride with a concentration of 0.2 mol per liters have been filled into the microfluidic chamber. The presented measurements show the exponential decay of the coherence for two different NV centers. A significant drop of T_1 times, that is sensitive to the different liquids, can be confirmed.

surface noise measurements in section 7.2.1. However, since the measured NV centers have not been the same, this is no contradiction. The numbers of total detected spins lie in the range of only 5 to 70. These numbers are comparable to the results presented in [212] for gadolinium spins. However, here we have not used a widefield image of a NV ensemble, but addressed individual defects. Thus, a better lateral localization of the magnetic fluctuations can be expected by our measurements.

7.2.3 Manganese Spin Sensing by Coherence Time T_2 Measurements

The second type of experiments has been the investigation of T_2 times, that are sensitive to lower frequencies in the range of about 0.2 to 1 MHz. In case of spin echo measurements, the calculations are slightly different than in the previous section. If one assumes a surface spin bath, with the magnetic field strength B_{SS} and the effective surface spin density $\sigma = n^{2/3}$, interacting with the NV center, one can derive for the decoherence rate [209]

$$\Gamma_i = \frac{\gamma_{NV}^2 B_{SS}^2}{2 f_{ss}} \tag{7.11}$$

with $\gamma_{NV} = 1.7593 \cdot 10^{11}\,\mathrm{s^{-1}T^{-1}}$ [142] and $f_{ss} = 5.66\,\mathrm{GHznm^3} \cdot \sigma^{3/2}$ [209] as a general relaxation rate due to the surface spin dynamics. For a certain depth z_0 one can use a

so called cluster expansion [209] and gets the following relation to the surface spins:

$$B_{ss} = 277\mu\mathrm{Tnm}^3 \cdot \frac{\sigma^{1/2}}{z_0^2}. \tag{7.12}$$
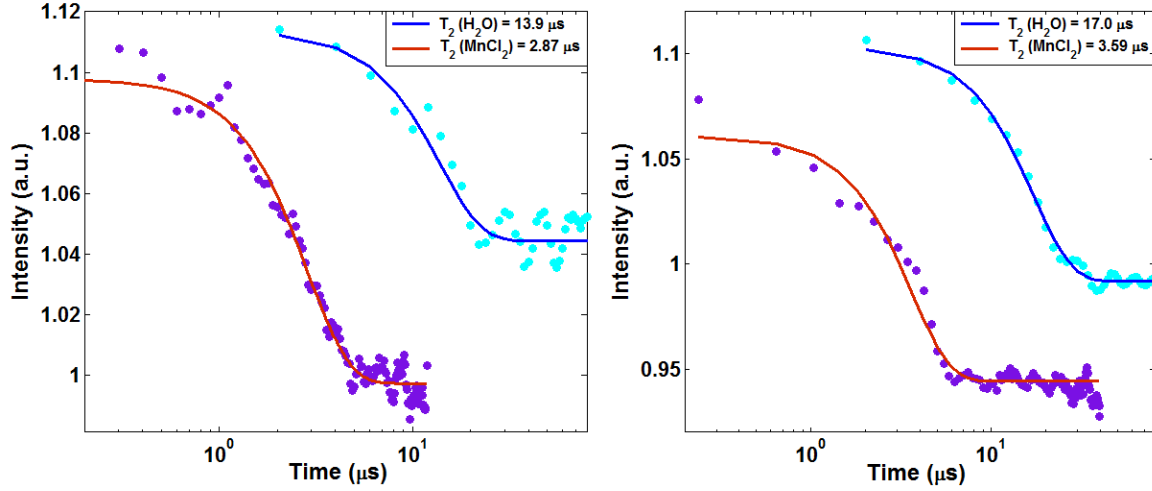
Figure 7.8: **Spin echo measurements of water and MnCl$_2$.** Two exemplary spin echo measurements of different NV centers for water and diluted manganese chloride in the microfluidic channel. As already measured for T_1 times, the external spins lead to a significant drop of the coherence time T_2.

Furthermore the contribution of one individual spin can be compared to the total variance of all spins interacting to the NV center. For the magnetic field of an individual spin B_j of the species i with distances r to the NV center one can consider

$$\left\langle B_j^2 \right\rangle = S\left(S+1\right)\left(\frac{\mu_0 g_i \mu_B}{4\pi r^3}\right)^2 \tag{7.13}$$

with the Landé factor of the spin g_i and the Bohr magneton μ_B. The overall interaction of all spins in the liquid can then be summed up to

$$\left\langle B^2 \right\rangle = 4\pi n \int_\infty^{z_0} \left\langle B_j^2 \right\rangle r^2 \approx S\left(S+1\right)\left(\frac{\mu_0 g_i \mu_B}{4\pi}\right)^2 \frac{1}{z_0^3}. \tag{7.14}$$

The effective number of spins N can then be stated to be the ratio

$$N = \frac{\left\langle B^2 \right\rangle}{\left\langle B_j^2 \right\rangle} = \frac{4}{3}\pi n z_0^3. \tag{7.15}$$

Thus this set of equations enables us to calculate the number of spins and depth of the NV center from the measurements of the spin echo decoherence rates.

In total, the evaluation of 21 T_2 measurements gives an average T_2 time of $29.8 \pm 19\,\mu s$ for water. Here, the diluted manganese chloride with a concentration of $0.2\,mol/l$ decreases the coherence time by a factor of 3.9 ± 1.5. The distribution of the coherence times is depicted in figure 7.9.
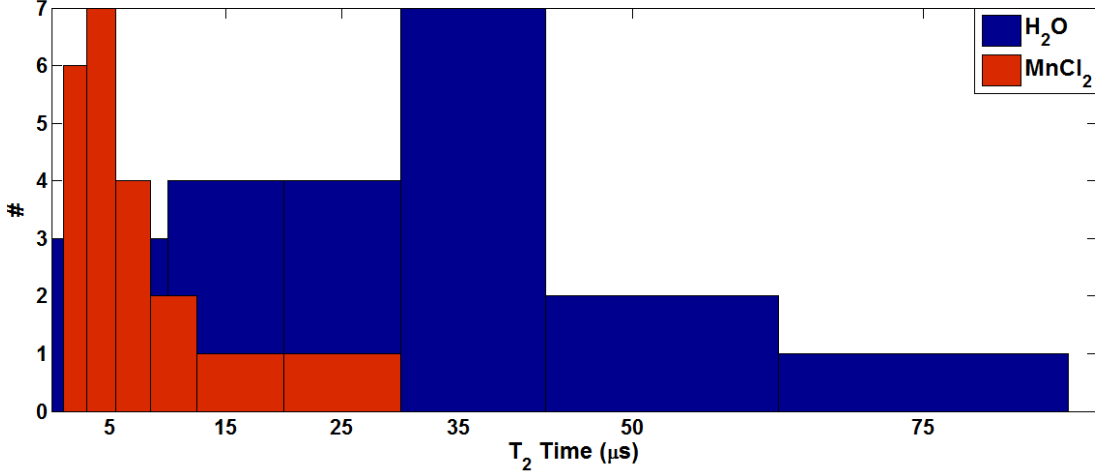
Figure 7.9: **T_2 time distribution for water and MnCl$_2$.** The distribution of 21 measured T_2 times shows an overall significant decrease for diluted manganese spins. Whereas coherence times for water are in the range of $8.8\,\mu s$ to $83.8\,\mu s$, an average decrease by a factor 3.9 gives a range of $2.3\,\mu s$ to $23.5\,\mu s$ in the presence of manganese spins of the concentration $0.2\,mol/l$.

Our calculations relate these values to a depth of $2.1 \pm 0.5\,nm$ for the measured NV centers, respectively to a range of 3 to 15 detected spins. The values are comparable to results presented for nanodiamonds with a size of $45\,nm$. Here the detection of order 10^3 spins have been stated [209]. Since our population of selected NV centers is located closer to the surface, our T_2 times proved to show a better sensitivity to external spins. Of course, the question of accuracy can be addressed to the calculations. A comparison of the results from T_2 times and T_1 times of the same NV centers give slightly deeper NV centers for the latter case of additional $0.5\,nm$. Nevertheless, the number of spins, that interact with the defect, both show values clearly below 100. Since both coherence time measurements show different sensitivites to certain frequencies, a deviation can be expected anyway.

In summary for all measurements, we successfully showed the implementation of magnetic sensing of small volumes of different liquids for water and a $0.2\,M$ MnCl$_2$ solution by single defect centers. The measured NV centers showed a decline of the coherence times that can be related to a sensitivity of few Mn^{2+} spins in a detection volume of $4.5\,nm^3$. Moreover, one can confirm another reliable method for depth determination in

case of shallow implanted emitters.

Note: Experiments with the microfludic chamber have been performed by the author together with bachelor student Felix Stürner. Parts of this summary have already been presented in the student's bachelor thesis. In case of surface noise spectroscopy measurements the author was supported by the bachelor student Felix Glöckler who helped investigating the implanted area and searching for measurable xy-8 signals. Dr. Liam McGuinness provided support and fruitful advices for the experiments and has been in charge for the preparation and pre-characterization of the sample. Laser cutting was done by him in the University of Melbourne, whereas the implantation has been performed by Nicole Raatz of the University of Bochum.

———— Summary

The focus of this thesis has been the highly resolved localization of NV centers in diamond, that can further be used as precise sensors, e.g. for magnetometry. In the optical part of the experiments, advanced methods of microscopy - namely GSD and FIONA - have been applied to achieve a superresolution of the position of the NV center. These methods were complemented by a spectroscopic approach for microfluidic measurements. Here, the sensing of external spins in proximity to the defect center has been exploited to use the NV center as a sensitive probe of magnetic field fluctuations, as well as for precise localization.

The GSD experiments confirmed a resolution of the same order of magnitude as the best results given in literature. It was even possible to distinguish two NV centers that showed a distance of only 14 nanometers between them. In case of FIONA, a totally new evaluation and measurement method has been developed and published, to determine the position of NV centers below the diamond surface with a precision in the regime of few nanometers. This has been achieved by an analysis of the correlation between two light signals, one from the reflected light at the surface and the other from the fluorescent emitter. The final optical resolution for shallow NV centers is significantly better than recent methods in literature. The overall measurements show a good agreement according to expected depth distributions and seem to confirm the reliability of the results. Furthermore a theoretical approach to the determination of the focal shift was given both by a calculated model and an experimental approach.

Finally, experiments that covered sensing of spins in liquids, have been successfully performed. These measurements provide a different localization method, that is not only dependent on an optical measurement, but uses the interaction of the NV center with magnetic field fluctuations. Three different evaluation concepts, namely spin noise spectroscopy, and determination of T_1 and T_2 coherence times were used and are based on recent publications in literature [63] [209] [212]. Here, these concepts have been assembled altogether to provide information about the depths of single NV centers for a custom-created microfludic device, as well as to confirm the possibility of sensitive spin sensing measurements. As opposed to recent publications, the coherence time measurements specifically focused on single NV centers instead of NV ensembles. A microfluidic chamber was constructed and a sensitivity of the NV centers to a small number of manganese spins has been successfully shown. The results are consistent to other experiments (e.g. see named literature) and show the applicability of NV centers combined with microfluidic devices for the measurements of spins in liquid. A sensitivity of the coherence time of shallow NV centers to only a small number of spins can be confirmed.

Summary

Outlook

The results presented in this thesis may provide a valuable resource for further advancements. Concerning the presented separation of NV pairs by GSD microscopy, it is possible to combine the measurements with the single photon source property of the NV center. For a standard confocal spot, a statistical evaluation by antibunching has succesfully resolved a NV center pair at a distance of 8.5 nm [215]. A combination to GSD - or similarly STED - could provide an additional boost of the resolution.

The second type of experiment - the application of the FIONA principle showed a promising absolute accuracy of 2.6 nm for shallow NV centers. However, these results still suffer from a high relative error. Nevertheless, even considering an increasing error for deeper emitters, the demonstrated technique can still be useful for such emitters. In this regime (beyond a depth of approximately 10 nm) sophisticated NMR and EPR measurements [63] cannot be easily applied and the absolute error is still way better than the diffraction limit. In this context, one has to state additionally, that the measurements of NMR signals rely on the NV center being in the negative charge state, that likely changes to NV^0 for very shallow NV centers (depth < 2 nm). Since our method does not distinguish between the two charge states, even these converted defects are detectable.

We believe, the method can be further improved by combining it with other experimental techniques. The calibration of the setup to measure the relative position of the NV centers to the surface could be done by NMR measurements [63] [181]. This would decrease the absolute error to a value below 1 nanometer and could be of much faster experimental application than a measurement of a whole ensemble of emitters. Further investigations could be supported by detailed surface profile measurements by AFM. This could provide insight of the surface roughness to the overall depth accuracy. Another idea is the use of a narrow band emitter like the silicon-vacancy center [216]. Here a more slender PSF is expected to improve the precision compared to our NV measurements. Furthermore a combination of this method to reversible saturable optical fluorescence transition (RESOLFT) measurement principles like STED and PALM [217] [218] could be suitable. The RESOLFT concepts alone are not applicable for depth measurements, since no improvement in determination of the surface is obtained. Thus, a simultaneous application of FIONA of the surface with STED measurements of NV centers could give more precise results.

Moreover, since the reported results show a spatial precision and accuracy far better than the diffraction limit, this method can support implantation and localization techniques for recent advances in quantum information processing [219] or NMR applications where a precise knowledge about the position of the emitter is crucial. Aside from that the investigation of biological processes is a possible application. Although superresolution techniques are already used in bioimaging [220] [221], NV centers could provide additional information for sensing of biomolecules [170] to gain further insight into organic processes on a molecular level, if the distance to the region of interest is known.

Finally, the spectroscopy experiments presented in chapter 7 can provide the basis of further investigations to magnetic sensing in liquids. The high sensitivity of the NV centers to only few spins can help to investigate the behavior of molecules like TEMPO

(short for (2,2,6,6-Tetramethyl-piperidin-1-yl)oxyl), which is a particularly stable radical and commonly used as a probe for biological systems [222].

The concept of the microfluidic channel is widely applicable to any kind of measurement. So far only hydrostatic experiments have been performed. However it is possible to apply a defined pressure and thus a constant flow through the chamber. One could investigate magnetic field fluctuations depending on the flow rate of different chemical species as well as different concentrations. It is even conceivable to get a time resolved measurement of chemical reactions that are filled in the microfluidic channel.

In conclusion, the results of this thesis will help a precise localization of NV defects in combination with a high sensitivity to external spins. The concepts, that have been laid out, are able to improve the usability especially for further investigations of spins in liquids, not only from a sensitivity point of view, but also from a perspective of precise localization.

BIBLIOGRAPHY

[1] E. Abbe, "Beiträge zur Theorie des Mikroskops und der mikroskopischen Wahrnehmung," Archiv für Mikroskopische Anatomie **9**(1), 413–468 (1873).

[2] C. Cremer and T. Cremer, "4π-Punkthologramme: Physikalische Grundlagen und mögliche Anwendungen," Dt. Patentamt, Patentschriftenvertriebsstelle, Patentschrift **P 21 16 521.9** (1971).

[3] C. Cremer and T. Cremer, "Considerations on a laser-scanning-microscope with high resolution and depth of field," Microscopica Acta **81**(1), 31–44 (1978).

[4] S. W. Hell, S. Lindek, C. Cremer, and E. H. K. Stelzer, "Measurement of the 4pi-confocal point spread function proves 75 nm axial resolution," Appl. Phys. Lett. **64**, 1335–1337 (1994).

[5] P. E. Hänninen, S. W. Hell, J. Salo, E. Soini, and C. Cremer, "Two-photon excitation 4Pi confocal microscope - Enhanced axial resolution microscope for biological research," Appl. Phys. Lett., **68**, 1698-1700 (1995).

[6] S. W. Hell, and J. Wichmann, "Breaking the diffraction resolution limit by stimulated emission: stimulated-emission-depletion fluorescence microscopy," Opt. Lett. **19**(11), S. 780–782 (1994).

[7] T. A. Klar, and S. W. Hell, "Subdiffraction resolution in far-field fluorescence microscopy," Opt. Lett. **24**(14), 954–956 (1999).

[8] S. W. Hell, "Toward fluorescence nanoscopy," Nat. biotechnol. **21**(11), 1347–1355 (2003).

[9] V. Westphal, and S. W. Hell, "Nanoscale resolution in the focal plane of an optical microscope," Phys. Rev. Lett. **94**, 143903 (2005).

[10] E. Rittweger, K. Y. Han, S. E. Irvine, C. Eggeling, and S. W. Hell, "Sted microscopy reveals crystal colour centres with nanometric resolution," Nat. Photonics **3**(3), 144–147 (2009).

[11] T. A. Klar, S. Jakobs, M. Dyba, A. Egner, and S. W. Hell, "Fluorescence microscopy with diffraction resolution barrier broken by stimulated emission," Proc. Natl. Acad. Sci. U.S.A. **97**(15), 8206–8210 (2000).

[12] U. V. Nägerl, K. I. Willig, B. Hein, S. W. Hell, and T. Bonhoeffer, "Live-cell imaging of dendritic spines by STED microscopy," Proc. Natl. Acad. Sci. U.S.A. **105**(48), 18982–18987 (2008).

[13] R. Wombacher, M. Heidbreder, S. van de Linde, M. P. Sheetz, M. Heilemann, V. W. Cornish, and M. Sauer, "Live-cell super-resolution imaging with trimethoprim conjugates," Nat. Methods **7**, 717–719 (2010).

[14] S. W. Hell and M. Kroug, "Ground-state-depletion fluorscence microscopy: A concept for breaking the diffraction resolution limit," Appl. Phys. B **60**(5), 495–497 (1995).

[15] K. Y. Han, S. K. Kim, C. Eggeling, and S. W. Hell, "Metastable dark states enable ground state depletion microscopy of nitrogen vacancy centers in diamond with diffraction-unlimited resolution," Nano Lett **10**(8), 3199–3203 (2010).

[16] E. Rittweger, D. Wildanger, and S. W. Hell, "Far-field fluorescence nanoscopy of diamond color centers by ground state depletion," Europhys. Lett. **86**(1), 14001 (2009).

[17] E. Betzig, G. H. Patterson, R. Sougrat, O. W. Lindwasser, S. Olenych, J. S. Bonifacino, M. W. Davidson, J. Lippincott-Schwartz, and H. F. Hess, "Imaging intracellular fluorescent proteins at nanometer resolution," Science **313**(5793), 1642–1645 (2006).

[18] S. T. Hess, T. P. K. Girirajan, and M. D. Mason, "Ultra-high resolution imaging by fluorescence photoactivation localization microscopy," Biophys. J. **91**(11), 4258–4272 (2006).

[19] M. J. Rust, M. Bates, and X. Zhuang, "Sub-diffraction-limit imaging by stochastic optical reconstruction microscopy (storm)," Nat. Methods **3**(10), 793–796 (2006).

[20] B. Huang, W. Wang, M. Bates, and X. Zhuang, "Three-dimensional super-resolution imaging by stochastic optical reconstruction microscopy," Science **319**(5864), 810–813 (2008).

[21] A. Yildiz and P. R. Selvin, "Fluorescence imaging with one nanometer accuracy: Application to molecular motors," Accounts Chem. Res. **38**(7), 574582 (2005).

[22] N. Bobroff, "Position measurement with a resolution and noise limited instrument," Rev. Sci. Instrum. **57**(6), 1152–1157 (1986).

[23] R. E. Thompson, D. R. Larson, and W. W. Webb, "Precise nanometer localization analysis for individual fluorescent probes," Biophys. J. **82**(5), 2775 – 2783 (2002).

[24] R. J. Ober, S. Ram, and E. S. Ward, "Localization accuracy in single-molecule microscopy," Biophys. J. **86**(2), 1185–1200 (2004).

[25] A. Pertsinidis, Y. Zhang, and S. Chu, "Subnanometre single-molecule localization, registration and distance measurements," Nature **466**, 647 - 651 (2010).

[26] A. Yildiz, J. N. Forkey, S. A. McKinney, T. Ha, Y. E. Goldman, and P. R. Selvin, "Myosin v walks hand-over-hand: single fluorophore imaging with 1.5-nm localization," Science **300**(5628), 2061–2065 (2003).

[27] A. D. Dinsmore, E. R. Weeks, V. Prasad, A. C. Levitt, and D. A. Weitz, "Three-dimensional confocal microscopy of colloids," Appl. Optics **40**(24), 4152–4159 (2001).

[28] S. R. P. Pavani, M. A. Thompson, J. S. Biteen, S. J. Lord, N. Liu, R. J. Twieg, R. Piestun, and W. E. Moerner, "Three-dimensional, single-molecule fluorescence imaging beyond the diffraction limit by using a double-helix point spread function," P. Natl. Acad. Sci. USA **106**(9), 2995–2999 (2009).

[29] S. H. Lee, M. Baday, M. Tjioe, P. D. Simonson, R. Zhang, E. Cai, and P. R. Selvin, "Using fixed fiduciary markers for stage drift correction," Opt. Express **20**(11), 12177–12183 (2012).

[30] A. J. Häußler, P. Heller, L. P. McGuinness, B. Naydenov, and F. Jelezko, "Optical depth localization of nitrogen-vacancy centers in diamond with nanometer accuracy," Opt. Express **22**(24), 29986–29995 (2014).

[31] S. Gerlich, S. Eibenberger, M. Tomandl, S. Nimmrichter, K. Hornberger, P. J. Fagan, J. Tüxen, M. Mayor, and M. Arndt, "Quantum interference of large organic molecules," Nat. Commun. **2**(263) (2011).

[32] M. Arndt, O. Nairz, J. Vos-Andreae, C. Keller, G.van der Zouw, and A. Zeilinger "Wave-particle duality of C60 molecules," Nature **401**, 680–682 (1999).

[33] M. Planck, "Über das Gesetz der Energieverteilung im Normalspektrum," Ann. Phys. **309**, 553–563 (1901).

[34] A. Einstein, "Über einen die Erzeugung und Verwandlung des Lichtes betreffenden heuristischen Gesichtspunkt," Ann. Phys. **322**, 132–148 (1905).

[35] L. de Broglie, "Ondes et Quanta," Comptes Rendus **177**, 507–510 (1923).

[36] W. Heisenberg, "Über quantentheoretische Umdeutung kinematischer und mechanischer Beziehungen," Z. Phys. **33**(1), 879–893 (1925).

[37] E. Schrödinger "Quantisierung als Eigenwertproblem," Ann. Phys. **384**(4), 361–376 (1926).

[38] D. Aerts, "Quantum theory and human perception of the macro-world," Front. Psychol. **5**(554) (2014).

[39] W. H. Zurek, "Decoherence, einselection, and the quantum origins of the classical," Rev. Mod. Phys. **75**, 716–775 (2003).

Bibliography

[40] M. W. Doherty, N. B. Manson, P. Delaney, F. Jelezko, J. Wrachtrup, L. C. L. Hollenberg, "The nitrogen-vacancy colour centre in diamond," Phys. Rep. **528**(1), 1–45 (2013).

[41] F. Jelezko, and J. Wrachtrup, "Single defect centres in diamond: A review," Phys. Stat. Solidi A **203**(13), 3207–3225 (2006).

[42] F. Neugart, A. Zappe, F. Jelezko, C. Tietz, J. P. Boudou, A. Krueger, and J. Wrachtrup, "Dynamics of Diamond Nanoparticles in Solution and Cells," Nano Lett. **7**(12), 3588–3591 (2007).

[43] J. P. Boudou, P. Curmi, F. Jelezko, J. Wrachtrup, P. Aubert, M. Sennour, G. Balasubramanian, R. Reuter, A. Thorel, and E. Gaffet, "High yield fabrication of fluorescent nanodiamonds," Nanotech. **20**(23), 235602 (2009).

[44] C. Kurtsiefer, S. Mayer, P. Zarda, and H. Weinfurter, "Stable Solid-State Source of Single Photons," Phys. Rev. Lett. **85**(2),290–293 (2000).

[45] T. M. Babinec, B. J. M. Hausmann, M. Khan, Y. Zhang, J. R. Maze, P, R. Hemmer, and Marko Loncar, "A diamond nanowire single-photon source," Nat. Nanotech. **5**, 195–199 (2010).

[46] A. Gruber, A. Drabenstedt, C. Tietz, L. Fleury, J. Wrachtrup, and C. von Borczyskowski, "Scanning Confocal Optical Microscopy and Magnetic Resonance on Single Defect Centers," Science **276**(5321), 2012–2014 (1997).

[47] G. Balasubramanian, P. Neumann, D. Twitchen, M. Markham, R. Kolesov, N. Mizuochi, J. Isoya, J. Achard, J. Beck, J. Tissler, V. Jacques, P. R. Hemmer, F. Jelezko, and J. Wrachtrup, "Ultralong spin coherence time in isotopically engineered diamond," Nat. Mater. **8**(5) 383–387 (2009).

[48] F. Jelezko, T. Gaebel, I. Popa, A. Gruber, and J. Wrachtrup, "Observation of coherent oscillations in a single electron spin," Phys. Rev. Lett. **92**(7), 076401 (2004).

[49] J. Wrachtrup, and F. Jelezko, "Processing quantum information in diamond," J. Phys.-Condens. Mat. **18**(21), S807–S824 (2006).

[50] T. Ladd, F. Jelezko, R. Laflamme, Y. Nakamura, C. Monroe, and J. L. O'Brien, "Quantum computers," Nature **464**(7285), 45–53 (2010).

[51] D. Deutsch, "Quantum Theory, the Church-Turing Principle and the Universal Quantum Computer," P. Roy. Soc. Lond. A Mat. **400**(1818), 97–117 (1985).

[52] F. Jelezko, T. Gaebel, I. Popa, M. Domhan, A. Gruber, and J. Wrachtrup, "Observation of coherent oscillation of a single nuclear spin and realization of a two-qubit conditional quantum gate," Phys. Rev. Lett. **93**(13), 130501 (2004).

[53] L. Jiang, G. Dutt, E. Togan, L. Childress, P. Cappellaro, J. Taylor, and M. Lukin, "Coherence of an Optically Illuminated Single Nuclear Spin Qubit," Phys. Rev. Lett. **100**(7), 073001 (2008).

[54] M. Dutt, L. Childress, L. Jiang, E. Togan, J. Maze, F. Jelezko, A. Zibrov, P. R. Hemmer, and M. Lukin, "Quantum register based on individual electronic and nuclear spin qubits in diamond," Science **316**(5829), 1312–1316 (2007).

[55] G. Waldherr, P. Neumann, S. F. Huelga, F. Jelezko, and J. Wrachtrup, "Violation of a Temporal Bell Inequality for Single Spins in a Diamond Defect Center," Phys. Rev. Lett. **107**, 090401 (2011).

[56] J. Maze, P. Stanwix, J. Hodges, S. Hong, J. Taylor, P. Cappellaro, L. Jiang, M. Dutt, E. Togan, A. Zibrov, A. Yacoby, R. Walsworth, and M. Lukin, "Nanoscale magnetic sensing with an individual electronic spin in diamond," Nature **455**, 644–647 (2008).

[57] G. Balasubramanian, I. Chan, R. Kolesov, M. Al-Hmoud, J. Tisler, C. Shin, C. Kim, A. Wojcik, P. R. Hemmer, A. Krueger, T. Hanke, A. Leitenstorfer, R. Bratschitsch, F. Jelezko, and J. Wrachtrup, "Nanoscale imaging magnetometry with diamond spins under ambient conditions," Nature **455**, 648–651 (2008).

[58] L. T. Hall, J. H. Cole, C. D. Hill, and L. C. L. Hollenberg, "Sensing of Fluctuating Nanoscale Magnetic Fields Using Nitrogen-Vacancy Centers in Diamond," Phys. Rev. Lett. **103**, 220802 (2009).

[59] S. Steinert, F. Dolde, P. Neumann, A. Aird, B. Naydenov, G. Balasubramanian, F. Jelezko, and J. Wrachtrup, "High sensitivity magnetic imaging using an array of spins in diamond, " Rev. Sci. Instrum. **81**(4), 043705 (2010).

[60] F. Dolde, H. Fedder, M. W. Doherty, T. Nobauer, F. Rempp, G. Balasubramanian, T. Wolf, F. Reinhard, L. C. L. Hollenberg, F. Jelezko, and J. Wrachtrup, "Electric-field sensing using single diamond spins," Nat. Phys. **7**, 459–463 (2011).

[61] J. M. Taylor, P. Cappellaro, L. Childress, L. Jiang, D. Budker, P. R. Hemmer, A. Yacoby, R. Walsworth, and M. D. Lukin, "High-sensitivity diamond magnetometer with nanoscale resolution," Nat. Phys. **4**(10), 810–816 (2008).

[62] B. Grotz, J. Beck, P. Neumann, B. Naydenov, R. Reuter, F. Reinhard, F. Jelezko, J. Wrachtrup, D. Schweinfurth, B. Sarkar, and P. R. Hemmer, "Sensing external spins with nitrogen-vacancy diamond," New Journal of Physics 13(5), 055004 (2011).

[63] T. Staudacher, F. Shi, S. Pezzagna, J. Meijer, J. Du, C. A. Meriles, F. Reinhard, and J. Wrachtrup, "Nuclear magnetic resonance spectroscopy on a (5-nanometer)^3 sample volume," Science **339**(6119), 561–563 (2013).

Bibliography

[64] H. J. Mamin, M. Kim, M. H. Sherwood, C. T. Rettner, K. Ohno, D. D. Awschalom, and D. Rugar, "Nanoscale nuclear magnetic resonance with a nitrogen-vacancy spin sensor," Science **339**(6119), 557–560 (2013).

[65] V. M. Acosta, E. Bauch, M. P. Ledbetter, A. Waxman, L.-S. Bouchard, and D. Budker, "Temperature Dependence of the Nitrogen-Vacancy Magnetic Resonance in Diamond," Phys. Rev. Lett. **104**, 070801 (2010).

[66] P. Neumann, I. Jakobi, F. Dolde, C. Burk, R. Reuter, G. Waldherr, J. Honert, T. Wolf, A. Brunner, J. H. Shim, D. Suter, H. Sumiya, J. Isoya, and J. Wrachtrup, "High-Precision Nanoscale Temperature Sensing Using Single Defects in Diamond," Nano Lett. **13**(6), 2738–2742 (2013).

[67] G. Kucsko, P. C. Maurer, N. Y. Yao, M. Kubo, H. J. Noh, P. K. Lo, H. Park, and M. D. Lukin, "Nanometre-scale thermometry in a living cell," Nature **500**(7460), 54–58 (2013)

[68] M. W. Doherty, V. V. Struzhkin, D. A. Simpson, L. P. McGuinness, Y. Meng, A. Stacey, T. J. Karle, R. J. Hemley, N. B. Manson, L. C. L. Hollenberg, and S. Prawer, "Electronic Properties and Metrology Applications of the Diamond NV$^-$ Center under Pressure," Phys. Rev. Lett. **112**, 047601 (2014).

[69] L. P. McGuinness, Y. Yan, A. Stacey, D. A. Simpson, L. T. Hall, D. Maclaurin, S. Prawer, P. Mulvaney, J. Wrachtrup, F. Caruso, R. E. Scholten, and L. C. L. Hollenberg, "Quantum measurement and orientation tracking of fluorescent nanodiamonds inside living cells," Nat. Nanotech. **6**, 358–363 (2011)

[70] J. Tisler, R. Reuter, A. Lämmle, F. Jelezko, G. Balasubramanian, P. R. Hemmer, F. Reinhard, and J. Wrachtrup "Highly efficient fret from a single nitrogen-vacancy center in nanodiamonds to a single organic molecule," ACS Nano **5**(10), 7893–7898 (2011).

[71] Y.-Y. Chen, H. Shu, Y. Kuo, Y.-K. Tzeng, and H.-C. Chang, "Measuring förster resonance energy transfer between fluorescent nanodiamonds and near-infrared dyes by acceptor photobleaching," Diam. Relat. Mater. **20**(5-6), 803 – 807 (2011).

[72] M. S. Grinolds, S. Hong, P. Maletinsky, L. Luan, M. D. Lukin, R. L. Walsworth, and A. Yacoby, "Nanoscale magnetic imaging of a single electron spin under ambient conditions," Nat. Phys. **9**, 215–219 (2013).

[73] P. Maletinsky, S. Hong, M. S. Grinolds, B. Hausmann, M. D. Lukin, R. L. Walsworth, M. Loncar, and A. Yacoby "A robust scanning diamond sensor for nanoscale imaging with single nitrogen-vacancy centres," Nat. Nanotech. **7**, 320–324 (2012).

[74] C. L. Degen, "Scanning magnetic field microscope with a diamond single-spin sensor," Appl. Phys. Lett. **92**, 243111 (2008).

[75] D. Rugar, R. Budakian, H. J. Mamin, and B. W. Chui, "Single spin detection by magnetic resonance force microscopy," Nature **430**, 329–332 (2004).

[76] H. Gross, "Handbook of Optical Systems, Volume 1, Fundamentals of Technical Optics," Wiley-VCH, ISBN 978-3-527-40377-9 (2005).

[77] W. Singer, M. Totzeck, and H. Gross, "Handbook of Optical Systems, Volume 2, Physical Image Formation," Wiley-VCH, ISBN 978-3-527-40378-3 (2005).

[78] H. Gross, H. Zügge, M. Peschka and F. Blechinger, "Handbook of Optical Systems, Volume 3, Aberration Theory and Correction of Optical Systems," Wiley-VCH, ISBN 978-3-527-40379-0 (2007).

[79] J. W. Strutt (3rd Baron Rayleigh), "Investigations in optics, with special reference to the spectroscope," Philos. mag. ser. 5 **8**(49), 261–274 (1879).

[80] U. Kubitscheck, "Fluorescence Microscopy. From Principles to Biological Applications," Wiley-VCH, ISBN 978-3-527-32922-9 (2013).

[81] P. Davidovits, and M. D. Egger, "Scanning Laser Microscope," Nature **223**, 831 (1969).

[82] P. Davidovits, and M. D. Egger, "Scanning Laser Microscope for Biological Investigations," Appl. Opt. **10**(7), 1615–1619 (1971).

[83] G. Cox, and C. J. R. Sheppard, "Practical limits of resolution in confocal and non-linear microscopy," Microsc. Res. Techniq. **63**(1), 18–22 (2004).

[84] F. Zernike, "Beugungstheorie des Schneidenverfahrens und seiner verbesserten Form, der Phasenkontrastmethode," Physica **1**(7-12), 689–704 (1934).

[85] R. J. Noll, "Zernike polynomials and atmospheric turbulence," J. Opt. Soc. Am., **66**(3), 207–211 (1976).

[86] L. Seidel, "Ueber die Theorie der Fehler, mit welchen die durch optische Instrumente gesehenen Bilder behaftet sind, und über die mathematischen Bedingungen ihrer Aufhebung," Abh. nat.-tech. Comm. Königl. Bayer. Ak. Wiss. München **1**, 227–267 (1857).

[87] R. K. Tyson, "Conversion of Zernike aberration coefficients to Seidel and higher-order power-series aberration coefficients," Opt. Lett. **7**(6), 262–264 (1982).

[88] G. Conforti, "Zernike aberration coefficients from Seidel and higher-order power-series coefficients," Opt. Lett. **8**(7), 407–408 (1983).

[89] G. T. Di Francia,"Super-gain antennas and optical resolving power," Il Nuovo Cimento **9**(3 Supplement), 426–438 (1952).

Bibliography

[90] W. Lukosz, "Optical Systems with Resolving Powers Exceeding the Classical Limit," J. Opt. Soc. Am. **56**(11), 1463–1471 (1966).

[91] C. Xu, W. Zipfel, J. B. Shear, R. M. Williams, and W. W. Webb, "Multiphoton fluorescence excitation: new spectral windows for biological nonlinear microscopy," Proc. Natl. Acad. Sci. U.S.A. **93**(20), 10763–10768 (1996).

[92] A. Schönle, and S.W. Hell, "Far-field fluorescence microscopy with repetitive excitation," Eur. Phys. J. D. **6**(3), 283–290 (1999).

[93] N. R. Heckenberg, R. McDuff, C. P. Smith, and A. G. White, "Generation of optical phase singularities by computer-generated holograms," Opt. Lett. **17**(3), 221–223 (1992).

[94] Y. Kozawa, and S. Sato "Generation of a radially polarized laser beam by use of a conical Brewster prism," Opt. Lett. **30**(22), 3063–3065 (2005).

[95] E. Rittweger, "Maximizing far-field optical microscopy resolution through selected fluorophore transitions," Universität Heidelberg, Fakultät für Physik und Astronomie, Dissertation (2009).

[96] K. I. Willig, B. Harke, R. Medda, and S. W. Hell, "STED microscopy with continuous wave beams," Nat. Meth. **4**, 915–918 (2007).

[97] G. Moneron, R. Medda, B. Hein, A. Giske, V. Westphal, and S. W. Hell, "Fast STED microscopy with continuous wave fiber lasers," Opt. Express **18**(2), 1302–1309 (2010).

[98] D. Wildanger, B. R. Patton, H. Schill, L. Marseglia, J. P. Hadden, S. Knauer, A. Schönle, J. G. Rarity, J. L. O'Brien, S. W. Hell, and J. M. Smith, "Solid Immersion Facilitates Fluorescence Microscopy with Nanometer Resolution and Sub-Ångström Emitter Localization," Adv. Mater. **24**(44), OP309–OP313 (2012).

[99] M. A. Lauterbach, C. K. Ullal, V. Westphal, and S. W. Hell, "Dynamic Imaging of Colloidal-Crystal Nanostructures at 200 Frames per Second," Langmuir **26**(18), 14400–14404 (2010).

[100] S. W. Hell, "Far-Field Optical Nanoscopy," Science **316**(5828), 1153–1158 (2007).

[101] S. W. Hell, "Microscopy and its focal switch," Nat. Meth. **6**, 24–32 (2009).

[102] M. K. Cheezum, W. F. Walker, and W. H. Guilford, "Quantitative comparison of algorithms for tracking single fluorescent particles," Biophys. J. **81**(4), 2378–2388 (2001).

[103] S. S. Rogers, T. A. Waigh, X. Zhao, and J. R. Lu, "Precise particle tracking against a complicated background: polynomial fitting with gaussian weight," Phys. Biol. **4**(3), 220 (2007).

[104] P. R. Hemmer, and T. Zapata, "The universal scaling laws that determine the achievable resolution in different schemes for super-resolution imaging," J. Opt. **14**, 083002 (2012).

[105] C. W. J. Beenakker, "Thermal Radiation and Amplified Spontaneous Emission from a Random Medium," Phys. Rev. Lett. **81**(9), 1829–1832 (1998).

[106] P. Török, and T. Wilson, "Rigorous theory for axial resolution in confocal microscopes," Opt. Comm. **137**(1-3), 127–135 (1997).

[107] H. Bornfleth, P. Edelmann, D. Zink, T. Cremer, and C. Cremer, "Quantitative Motion Analysis of Subchromosomal Foci in Living Cells Using Four-Dimensional Microscopy," Biophys. J. **77**(5), 2871–2886 (1999).

[108] D. Thomann, D. R. Rines, P. K. Sorger, and G. Danuser, "Automatic fluorescent tag detection in 3D with super-resolution: application to the analysis of chromosome movement," J. Micr. **208**(1), 49–64 (2002).

[109] T. M. Watanabe, and H. Higuchi, "Stepwise Movements in Vesicle Transport of HER2 by Motor Proteins in Living Cells," Biophys. J. **92**(11), 4109–4120 (2007).

[110] T. Ragan, Hayden Huang, Peter So, and Enrico Gratton , "3D Particle Tracking on a Two-Photon Microscope," J. Fluoresc. **16**(3), 325–336 (2006).

[111] H.P. Kao, and A.S. Verkman, "Tracking of single fluorescent particles in three dimensions: use of cylindrical optics to encode particle position," Biophys. J. **67**(3), 1291–1300 (1994).

[112] A.M van Oijen, J. Köhler, J. Schmidt, M. Müller, and G.J. Brakenhoff, "3-Dimensional super-resolution by spectrally selective imaging," Chem. Phys. Lett. **292**(1-2), 183–187 (1998).

[113] M. Speidel, Alexandr Jonáš, and E.-L. Florin, "Three-dimensional tracking of fluorescent nanoparticles with subnanometer precision by use of off-focus imaging," Opt. Lett. **28**(2), 69–71 (2003).

[114] M. F. Juette, T. J. Gould, M. D. Lessard, M. J. Mlodzianoski, B. S. Nagpure, B. T. Bennett, S. T. Hess, and J. Bewersdorf, "Three-dimensional sub-100 nm resolution fluorescence microscopy of thick samples," Nat. Meth. **5**, 527–529 (2008).

[115] Y. Sun, J. D. McKenna, J. M. Murray, E. M. Ostap, and Y. E. Goldman, "Parallax: High Accuracy Three-Dimensional Single Molecule Tracking Using Split Images," Nano Lett. **9**(7), 2676–2682 (2009).

[116] G. Davies, and M. F. Hamer, "Optical Studies of the 1.945 eV Vibronic Band in Diamond," Proc. R. Soc. Lond. A **348**(1653), 285–298 (1976).

Bibliography

[117] F. P. Bundy, H. T. Hall, H. M. Strong, and R. H. Wentorf, "Man-Made Diamonds," Nature **176**, 51–54 (1955).

[118] H. Sumiya, and S. Satoh, "High-pressure synthesis of high-purity diamond crystal," Diam. Rel. Mater. **5**(11), 1359–1365 (1996).

[119] P. K. Bachmann, D. Leers, and H. Lydtin, "Towards a general concept of diamond chemical vapour deposition," Diam. Rel. Mater. **1**(1), 1–12 (1991).

[120] J.Isberg, J. Hammersberg, E. Johansson, T. Wikström, D. J. Twitchen, A. J. Whitehead, S. E. Coe, and G. A. Scarsbrook, "High Carrier Mobility in Single-Crystal Plasma-Deposited Diamond," Science **297**(5587), 1670–1672 (2002).

[121] J. Meijer, B. Burchard, M. Domhan, C. Wittmann, T. Gaebel, I. Popa, F. Jelezko, and J. Wrachtrup, "Generation of single color centers by focused nitrogen implantation," Appl. Phys. Lett. **87**, 261909 (2005).

[122] J. R. Rabeau, P. Reichart, G. Tamanyan, D. N. Jamieson, S. Prawer, F. Jelezko, T. Gaebel, I. Popa, M. Domhan, and J. Wrachtrup, "Implantation of labelled single nitrogen vacancy centers in diamond using ^{15}N," Appl. Phys. Lett. **88**, 023113 (2006).

[123] K. Ohno, F. J. Heremans, L. C. Bassett, B. A. Myers, D. M. Toyli, A. C. Bleszynski Jayich, C. J. Palmstrøm, and D. D. Awschalom, "Engineering shallow spins in diamond with nitrogen delta-doping," Appl. Phys. Lett. **101**, 082413 (2012).

[124] K. Ohashi, T. Rosskopf, H. Watanabe, M. Loretz, Y. Tao, R. Hauert, S. Tomizawa, T. Ishikawa, J. Ishi-Hayase, S. Shikata, C. L. Degen, and K. M. Itoh, "Negatively Charged Nitrogen-Vacancy Centers in a 5 nm Thin ^{12}C Diamond Film," Nano Lett. **13**(10), 4733–4738 (2013).

[125] M. V. Hauf, B. Grotz, B. Naydenov, M. Dankerl, S. Pezzagna, J. Meijer, F. Jelezko, J. Wrachtrup, M. Stutzmann, F. Reinhard, and J. A. Garrido, "Chemical control of the charge state of nitrogen-vacancy centers in diamond," Phys. Rev. B **83**, 081304(R) (2011).

[126] "Dynamic Jahn-Teller distortions at trigonal optical centres in diamond," J. Phys. C Solid State **12**, 2551–2566 (1979).

[127] L. Du Preez, "Electron Paramagnetic Resonance and Optical Investigations of Defect Centres in Diamond," University of The Witwatersrand, Dissertation (1965).

[128] E. van Oort, N. B. Manson and M. Glasbeek, "Optically detected spin coherence of the diamond N-V centre in its triplet ground state," J. Phys. C Solid State **21**, 4385–4391 (1988).

[129] A. Batalov, C. Zierl, T. Gaebel, P. Neumann, I.-Y. Chan, G. Balasubramanian, P. R. Hemmer, F. Jelezko, and J. Wrachtrup, "Temporal Coherence of Photons Emitted by Single Nitrogen-Vacancy Defect Centers in Diamond Using Optical Rabi-Oscillations," Phys. Rev. Lett. **100**, 077401 (2008).

[130] N. B. Manson, J. P. Harrison, and M. J. Sellars, "Nitrogen-vacancy center in diamond: Model of the electronic structure and associated dynamics," Phys. Rev. B **74**, 10430 (2006).

[131] Andrei Faraon, Paul E. Barclay, Charles Santori, Kai-Mei C. Fu, and Raymond G. Beausoleil, "Resonant enhancement of the zero-phonon emission from a colour centre in a diamond cavity," Nat. Photonics **5**, 301–305 (2011).

[132] L. P. McGuinness, "Nanoscale Quantum Sensing Using Nitrogen-Vacancy-Centers in Diamond," The University of Melbourne, Dissertation (2012).

[133] J. Wrachtrup, C. von Borczyskowski, J. Bernard, M. Orritt, and R. Brown, "Optical detection of magnetic resonance in a single molecule," Nature **363**, 244–245 (1993).

[134] X.-F. He, N. B. Manson, and P. T. H. Fisk, "Paramagnetic resonance of photoexcited N-V defects in diamond. I. Level anticrossing in the ^{3}A ground state," Phys. Rev. B **47**, 8809 (1993).

[135] P. Neumann, R. Kolesov, V. Jacques, J. Beck, J. Tisler, A. Batalov, L. Rogers, N. B. Manson, G. Balasubramanian, F. Jelezko, and J. Wrachtrup, "Excited-state spectroscopy of single NV defects in diamond using optically detected magnetic resonance," New J. Phys. **11**, 013017 (2009).

[136] R. Hanbury-Brown, and R. Q. Twiss, "Correlation between Photons in two Coherent Beams of Light," Nature **177**, 27–29 (1956).

[137] R. Hanbury-Brown, and R. Q. Twiss, "A Test of a New Type of Stellar Interferometer on Sirius," Nature **178**, 1046–1048 (1956).

[138] U. Fano, "Quantum Theory of Interference Effects in the Mixing of Light from Phase-Independent Sources," Am. J. Phys. **29**, 539 (1961).

[139] H. Paul, "Photon antibunching," Rev. Mod. Phys. **54**, 1061 (1982).

[140] R. Brouri, A. Beveratos, J.-P. Poizat, and P. Grangier, "Photon antibunching in the fluorescence of individual color centers in diamond," Opt. Lett. **25**(17), 1294–1296 (2000).

[141] E.T. Jaynes, and F.W. Cummings, "Comparison of quantum and semiclassical radiation theories with application to the beam maser". Proc. IEEE **51**(1), 89–109 (1963).

Bibliography

[142] J. H. N. Loubser, and J. A. van Wyk, "Electron spin resonance in the study of diamond," Rep. Prog. Phys. **41**, 1201 (1978).

[143] J. Gea-Banacloche, "A new look at the Jaynes-Cummings model for large fields: Bloch sphere evolution and detuning effects," Opt. Comm. **88**(4-6), 531–550 (1992).

[144] E. C. Reynhardt, and G. L. High, "Dynamic nuclear-polarization of diamond," J. Chem. Phys. **109**, 4090–4107 (1998).

[145] E. Van Oort, and M. Glasbeek, "Optically detected low field electron spin echo envelope modulations of fluorescent N-V centers in diamond," Chem. Phys. **143**(1), 131–140 (1990).

[146] L. Childress, M. V. Gurudev Dutt, J. M. Taylor, A. S. Zibrov, F. Jelezko, J. Wrachtrup, P. R. Hemmer, and M. D. Lukin, "Coherent Dynamics of Coupled Electron and Nuclear Spin Qubits in Diamond," Science **314**(5797), 281–285 (2006).

[147] J. R. Maze, J. M. Taylor, and M. D. Lukin, "Electron spin decoherence of single nitrogen-vacancy defects in diamond," Phys. Rev. B **78**, 094303 (2008).

[148] T.A. Kennedy, F.T. Charnock, J.S. Colton, J.E. Butler, R.C. Linares, and P.J. Doering, "Single-Qubit Operations with the Nitrogen-Vacancy Center in Diamond," phys. status solidi (b) **233**(3), 416–426 (2002).

[149] T. A. Kennedy, J. S. Colton, J. E. Butler, R. C. Linares, and P. J. Doering, "Long coherence times at 300 K for nitrogen-vacancy center spins in diamond grown by chemical vapor deposition," Appl. Phys. Lett. **83**, 4190 (2003).

[150] N. Mizuochi, P. Neumann, F. Rempp, J. Beck, V. Jacques, P. Siyushev, K. Nakamura, D. J. Twitchen, H. Watanabe, S. Yamasaki, F. Jelezko, and J. Wrachtrup, "Coherence of single spins coupled to a nuclear spin bath of varying density," Phys. Rev. B **80**, 041201(R) (2009).

[151] V. M. Acosta, E. Bauch, M. P. Ledbetter, C. Santori, K.-M. C. Fu, P. E. Barclay, R. G. Beausoleil, H. Linget, J. F. Roch, F. Treussart, S. Chemerisov, W. Gawlik, and D. Budke, "Diamonds with a high density of nitrogen-vacancy centers for magnetometry applications," Phys. Rev. B 80, 115202 (2009).

[152] B. K. Ofori-Okai, S. Pezzagna, K. Chang, M. Loretz, R. Schirhagl, Y. Tao, B. A. Moores, K. Groot-Berning, J. Meijer, and C. L. Degen, "Spin properties of very shallow nitrogen vacancy defects in diamond," Phys. Rev. B **86**, 081406(R) (2012).

[153] T. Staudacher, F. Ziem, L. Häussler, R. Stöhr, S. Steinert, F. Reinhard, J. Scharpf, A. Denisenko, and J. Wrachtrup, "Enhancing the spin properties of shallow implanted nitrogen vacancy centers in diamond by epitaxial overgrowth," Appl. Phys. Lett. 101, 212401 (2012).

[154] G. D. Fuchs, V. V. Dobrovitski, D. M. Toyli, F. J. Heremans, and D. D. Awschalom, "Gigahertz Dynamics of a Strongly Driven Single Quantum Spin'," Science **326**(5959), 1520–1522 (2009).

[155] G. de Lange, Z. H. Wang, D. Risè, V. V. Dobrovitski, and R. Hanson, "Universal Dynamical Decoupling of a Single Solid-State Spin from a Spin Bath," Science **330**(6000), 60–63 (2010).

[156] A. M. Souza, G. A. Álvarez, and D. Suter, "Robust Dynamical Decoupling for Quantum Computing and Quantum Memory," Phys. Rev. Lett. **106**, 240501 (2011).

[157] N. Khaneja, T. Reiss, C. Kehlet, T. Schulte-Herbrüggen, and S. J. Glaser, "Optimal control of coupled spin dynamics: design of NMR pulse sequences by gradient ascent algorithms," J. Magn. Reson. **172**(2),296–305 (2005).

[158] S. Machnes, U. Sander, S. J. Glaser, P. de Fouquières, A. Gruslys, S. Schirmer, and T. Schulte-Herbrüggen, "Comparing, optimizing, and benchmarking quantum-control algorithms in a unifying programming framework," Phys. Rev. A **84**, 022305 (2011).

[159] D. Budker, and M. Romalis, "Optical magnetometry," Nat. Phys. **3**, 227–234 (2007).

[160] N. Gang, G. H. Parker, R. M. Lafrenie, and M. A. Persinger, "Intermittent exposures to nanoTesla range, 7 Hz, amplitude-modulated magnetic fields increase regeneration rates in planarian," Int. J. Radiat. Biol. **89**(5), 384–389 (2013).

[161] M. E. Huber, N. C. Koshnick, H. Bluhm, L. J. Archuleta, T. Azua, P. G. Björnsson, B. W. Gardner, S. T. Halloran, E. A. Lucero, and K. A. Moler, "Gradiometric micro-SQUID susceptometer for scanning measurements of mesoscopic samples," Rev. Sci. Instrum. **79**, 053704 (2008).

[162] R. Kleiner, D. Koelle, F. Ludwig, and J. Clarke, "Superconducting quantum interference devices: State of the art and applications," Proc. IEEE **92**(10), 1534–1548 (2004).

[163] G. Boero, M. Demierre, P.-.A. Besse, and R.S. Popovic, "Micro-Hall devices: performance, technologies and applications," Sens. Actuat. A Phys. **106**(1-3), 314–320 (2003).

[164] C. N. Owston, "A Hall effect magnetometer for small magnetic fields," J. Sci. Instrum. **44**, 798–800 (1967).

[165] M. Schaffry, E. M. Gauger, J. J. L. Morton, and S. C. Benjamin, "Spin Amplification for Magnetic Sensors Employing Crystal Defects," Phys. Rev. Lett., **107**(20), 207210 (2011).

Bibliography

[166] C. Degen, "Nanoscale magnetometry: Microscopy with single spins," Nat. Nanotechnol. **3**, 643 – 644 (2008).

[167] S. Hong, M. S. Grinolds, Linh M. Pham, D. Le Sage, L. Luan, R. L. Walsworth, and A. Yacoby, "Nanoscale magnetometry with NV centers in diamond," MRS Bull. **38**(2), 155–161 (2013).

[168] D. Le Sage, K. Arai, D. R. Glenn, S. J. DeVience, L. M. Pham, L. Rahn-Lee, M. D. Lukin, A. Yacoby, A. Komeili, and R. L. Walsworth, "Optical magnetic imaging of living cells," Nature **496**, 486–489 (2013).

[169] L. T. Hall, G. C. G. Beart, E. A. Thomas, D. A. Simpson, L. P. McGuinness, J. H. Cole, J. H. Manton, R. E. Scholten, F. Jelezko, J. Wrachtrup, S. Petrou, and L. C. L. Hollenberg, "High spatial and temporal resolution wide-field imaging of neuron activity using quantum NV-diamond," Sci. Rep. **2**, 401 (2012).

[170] A. Ermakova, G. Pramanik, J. Cai, G. Algara-Siller, U. Kaiser, T. Weil, Y.-K. Tzeng, H.-C. Chang, L. P. McGuinness, M. B. Plenio, B. Naydenov, and F. Jelezko, "Detection of a few metallo-protein molecules using color centers in nanodiamonds," Nano Lett. **13**(7), 3305–3309 (2013).

[171] S. Kaufmann, D. A. Simpson, L. T. Hall, V. Perunicic, P. Senn, S. Steinert, L. P. McGuinness, B. C. Johnson, T. Ohshima, F. Caruso, J. Wrachtrup, R. E. Scholten, P. Mulvaney, and L. Hollenberg, "Detection of atomic spin labels in a lipid bilayer using a single-spin nanodiamond probe," Proc. Natl. Acad. Sci. U.S.A. **110**(27), 10894–10898 (2013).

[172] L. Rondin, J.-P. Tetienne, S. Rohart, A. Thiaville, T. Hingant, P. Spinicelli, J.-F. Roch, and V. Jacques, "Stray-field imaging of magnetic vortices with a single diamond spin," Nat. Comm. **4**, 2279 (2013).

[173] J.-P. Tetienne, T. Hingant, J.-V. Kim, L. Herrera Diez, J.-P. Adam, K. Garcia, J.-F. Roch, S. Rohart, A. Thiaville, D. Ravelosona, and V. Jacques, "Nanoscale imaging and control of domain-wall hopping with a nitrogen-vacancy center microscope," Science **344**(6190), 1366–1369 (2014).

[174] A. Waxman, Y. Schlussel, D. Groswasser, V. M. Acosta, L.-S. Bouchard, D. Budker, and R. Folman, "Diamond magnetometry of superconducting thin films," Phys. Rev. B **89**, 054509 (2014).

[175] M. Loretz, T. Rosskopf, J. M. Boss, S. Pezzagna, J. Meijer, and C. L. Degen, "Single-proton spin detection by diamond magnetometry," Science DOI: 10.1126/science.1259464 (2014).

[176] M. Loretz et al., *Retraction*, Science **347**(6218), 139 (2015).

106

[177] L. Robledo, Lilian Childress, Hannes Bernien, Bas Hensen, Paul F. A. Alkemade, and Ronald Hanson, "High-fidelity projective read-out of a solid-state spin quantum register," Nature **477**, 574–578 (2011).

[178] M. S. Grinolds, M. Warner, K. De Greve, Y. Dovzhenko, L. Thiel, R. L. Walsworth, S. Hong, P. Maletinsky, and A. Yacoby, "Subnanometre resolution in three-dimensional magnetic resonance imaging of individual dark spins," Nat. Nanotech. **9**, 279–284 (2014).

[179] S. Meiboom, and D. Gill, "Modified Spin-Echo Method for Measuring Nuclear Relaxation Times," Rev. Sci. Instrum. **29**, 688–691 (1958).

[180] N. Bar-Gill, L. M. Pham, C. Belthangady, D. Le Sage, P. Cappellaro, J. R. Maze, M. D. Lukin, A. Yacoby, and R. Walsworth, "Suppression of spin-bath dynamics for improved coherence of multi-spin-qubit systems," Nat. Comm. **3**, 858 (2012).

[181] Y. Romach, C. Müller, T. Unden, L. J. Rogers, T. Isoda, K. M. Itoh, M. Markham, A. Stacey, J. Meijer, S. Pezzagna, B. Naydenov, L. P. McGuinness, N. Bar-Gill, and F. Jelezko,"Spectroscopy of surface-induced noise using shallow spins in diamond," Phys. Rev. Lett. **114**, 017601 (2015).

[182] T. Gullion, D.B. Baker, and M.S. Conradi, "New, compensated Carr-Purcell sequences," J. Magn. Reson., **89**(3), 479–484 (1990).

[183] C. Müller, X. Kong, J.-M. Cai, K. Melentijevic, A. Stacey, M. Markham, D. Twitchen, J. Isoya, S. Pezzagna, J. Meijer, J. F. Du, M. B. Plenio, B. Naydenov, L. P. McGuinness, and F. Jelezko, "Nuclear magnetic resonance spectroscopy with single spin sensitivity," Nat. Comm. **5**, 4703 (2014).

[184] L. Cywinski, R. M. Lutchyn, C. P. Nave, and S. Das Sarma, "How to enhance dephasing time in superconducting qubits," Phys. Rev. B **77**, 174509 (2008).

[185] Z. Bomzon, G. Biener, V. Kleiner, and E. Hasma, "Radially and azimuthally polarized beams generated by space-variant dielectric subwavelength gratings," Opt. Lett. **27**(5), 285–287 (2002).

[186] M. W. Beijersbergen, R. P. C. Coerwinkel, M. Kristensen, and J. P. Woerdman, "Helical-wavefront laser beams produced with a spiral phaseplate," Opt. Commun., **112**(5-6) 321 – 327 (1994).

[187] X. Hao, C. Kuang, T. Wang, and X. Liu, "Effects of polarization on the de-excitation dark focal spot in STED microscopy," J. Opt. **12**, 115707 (2010).

[188] S. Quabis, R. Dorn, M. Eberler, O. Glöckl, and G. Leuchs, "Focusing light to a tighter spot," Opt. Comm. **179**(1-6), 1–7 (2000).

Bibliography

[189] F. Dolde, I. Jakobi, B. Naydenov, N. Zhao, S. Pezzagna, C. Trautmann, J. Meijer, P. Neumann, F. Jelezko, and J. Wrachtrup, "Room-temperature entanglement between single defect spins in diamond," Nat. Phys. **9**, 139–143 (2013).

[190] B. Harke, J. Keller, C. K. Ullal, V. Westphal, A. Schönle, and S. W. Hell, "Resolution scaling in STED microscopy," Opt. Express, **16**(6), 4154 – 4162 (2008).

[191] W. H. Richardson, "Bayesian-Based Iterative Method of Image Restoration," J. Opt. Soc. Am. **62**(1), 55–59 (1972).

[192] S. Pezzagna, D. Wildanger, P. Mazarov, A. D. Wieck, Y. Sarov, I. Rangelow, B. Naydenov, F. Jelezko,S. W. Hell, and J. Meijer, "Nanoscale Engineering and Optical Addressing of Single Spins in Diamond," Small **6**(19), 2117–2121 (2010).

[193] S. Arroyo-Camejo, M.-P. Adam, M. Besbes, J.-P. Hugonin, V. Jacques, J.-J. Greffet, J.-F. Roch, S. W. Hell, and F. Treussart, "Stimulated Emission Depletion Microscopy Resolves Individual Nitrogen Vacancy Centers in Diamond Nanocrystals," ACS Nano **7**(12), 10912–10919 (2013).

[194] F. Goos, and H. Hänchen, "Über das Eindringen des totalreflektierten Lichtes in das dünnere Medium," Ann. Phys. **435**(5), 383–392 (1943).

[195] R. H. Renard, "Total Reflection: A New Evaluation of the Goos-Hänchen Shift," J. Opt. Soc. Am. **54**(10), 1190–1196 (1964).

[196] J. B. Götte, and M. R. Dennis, "Generalized shifts and weak values for polarization components of reflected light beams," New J. Phys., **14**(7), 073016 (2012).

[197] E. H. Hellen, and D. Axelrod, "Fluorescence emission at dielectric and metal-film interfaces," J. Opt. Soc. Am. B **4**(3), 337–350 (1987).

[198] J. Enderlein, E. Toprak, and P. R. Selvin, "Polarization effect on position accuracy of fluorophore localization," Opt. Express **14**(18), 8111–8120 (2006).

[199] A. V. Abraham, S. Ram, J. Chao, E. S. Ward, and R. J. Ober, "Quantitative study of single molecule location estimation techniques," Opt. Express **17**(26), 23352–23373 (2009).

[200] J. Gasper, G. C. Sherman, and J. J. Stamnes, "Reflection and refraction of an arbitrary electromagnetic wave at a plane interface," J. Opt. Soc. Am. **66**(9), 955–961 (1976).

[201] H. Ling, and S.-W. Lee "Focusing of electromagnetic waves through a dielectric interface," J. Opt. Soc. Am. A **1**(9), 965–973 (1984).

[202] E. R. MacQuarrie, T. A. Gosavi, N. R. Jungwirth, S. A. Bhave, and G. D. Fuchs, "Mechanical spin control of nitrogen-vacancy centers in diamond," Phys. Rev. Lett. **111**, 227602 (2013).

[203] S. H. Wiersma, P. Török, T. D. Visser, and P. Varga, "Comparison of different theories for focusing through a plane interface," J. Opt. Soc. Am. A **14**(7), 1482–1490 (1997).

[204] J. F. Ziegler, M. D. Ziegler, and J. P. Biersack, "Srim–the stopping and range of ions in matter (2010)," Nucl. Instrum. Meth. B **268**(11), 1818–1823 (2010).

[205] D. Antonov, T. Häußermann, A. Aird, J. Roth, H.-R. Trebin, C. Müller, L. McGuinness, F. Jelezko, T. Yamamoto, J. Isoya, S. Pezzagna, J. Meijer, and J. Wrachtrup, "Statistical investigations on nitrogen-vacancy center creation," Appl. Phys. Lett. **104**, 012105 (2014).

[206] A Young, C. Y. Hu, L. Marseglia, J. P. Harrison, J. L. O'Brien, and J. G. Rarity, "Cavity enhanced spin measurement of the ground state spin of an NV center in diamond," New J. Phys. **11**, 013007 (2009).

[207] L. Marseglia, J. P. Hadden, A. C. Stanley-Clarke, J. P. Harrison, B. Patton, Y.-L. D. Ho, B. Naydenov, F. Jelezko, J. Meijer, P. R. Dolan, J. M. Smith, J. G. Rarity, and J. L. O'Brien, "Nanofabricated solid immersion lenses registered to single emitters in diamond," Appl. Phys. Lett. **98**, 133107 (2011).

[208] H. J. Mamin, M. H. Sherwood, and D. Rugar, "Detecting external electron spins using nitrogen-vacancy centers," Phys. Rev. B 86, 195422 (2012).

[209] L. P. McGuinness, L. T. Hall, A. Stacey, D. A. Simpson, C. D .Hill, J. H. Cole, K. Ganesan, B. C. Gibson, S. Prawer, P. Mulvaney, F. Jelezko, J. Wrachtrup, R. E. Scholten, and L. C. L. Hollenberg, "Ambient nanoscale sensing with single spins using quantum decoherence," New J. Phys. **15**, 073042 (2013).

[210] K. Matsumoto, S. Subramanian, R. Murugesan, J. B. Mitchell, and M. C. Krishna, "Spatially Resolved Biologic Information from In Vivo EPRI, OMRI, and MRI," Antioxid. Redox Sign. **9**(8), 1125–1142 (2007).

[211] F. C. Ziem, N. S. GÖtz, A. Zappe, S. Steinert, and J. Wrachtrup, "Highly Sensitive Detection of Physiological Spins in a Microfluidic Device," Nano Lett. **13**(9), 4093–4098 (2013).

[212] S. Steinert, F. Ziem, L. T. Hall, A. Zappe, M. Schweikert, N. Götz, A. Aird, G. Balasubramanian, L. Hollenberg, and J. Wrachtrup, "Magnetic spin imaging under ambient conditions with sub-cellular resolution," Nat. Comm. **4**, 1607 (2013).

[213] S. Pezzagna, B. Naydenov, F. Jelezko, J. Wrachtrup, and J. Meijer, "Creation efficiency of nitrogen-vacancy centres in diamond," New J. Phys. **12**, 065017 (2010).

[214] L. P. McGuinness, Private Communication.

[215] J.-M. Cui, F.-W. Sun, X.-D. Chen, Z.-J. Gong, and G.-C. Guo, "Quantum Statistical Imaging of Particles without Restriction of the Diffraction Limit," Phys. Rev. Lett. **110**, 153901 (2013).

[216] L. J. Rogers, K. D. Jahnke, M. W. Doherty, A. Dietrich, L. P. McGuinness, C. Müller, T. Teraji, J. Isoya, N. B. Manson, and F. Jelezko, "Electronic structure of the negatively-charged silicon-vacancy center in diamond," Phys. Rev. B **89**, 235101 (2014).

[217] J. Keller, A. Schönle, and S. W. Hell, "Efficient fluorescence inhibition patterns for resolft microscopy," Opt. Express **15**(6), 3361–3371 (2007).

[218] K. Y. Han, K. I. Willig, E. Rittweger, F. Jelezko, C. Eggeling, and S. W. Hell, "Three-dimensional stimulated emission depletion microscopy of nitrogen-vacancy centers in diamond using continuous-wave light," Nano Lett. **9**(9), 3323–3329 (2009).

[219] J. Cai, A. Retzker, F. Jelezko, and M. B. Plenio, "A large-scale quantum simulator on a diamond surface at room temperature," Nat. Phys. **9**(3), 168–173 (2013).

[220] M. A. Thompson, M. D. Lew, and W.E. Moerner, "Extending microscopic resolution with single-molecule imaging and active control," Ann. Rev. Biophys. **41**(1), 321–342 (2012).

[221] A. Dupont and D. C. Lamb, "Nanoscale three-dimensional single particle tracking," Nanoscale **3**(11), 4532–4541 (2011).

[222] S. Barriga, "2,2,6,6-Tetramethylpiperidine-1-oxyl (TEMPO)," Synlett **4**, 563 (2001).

List of Figures

───── Acknowledgment

Acknowledgment

But life is not limited to university. Here, I need to thank my family for their permanent support in all situations. The most important supporters have certainly been my parents. Thanks for everything, be it support, advice or our time together. And I also want to especially mention my brother, with whom I have shared a lot of valuable experiences.

And so, the last part of the acknowledgment goes to people, who I am really grateful of knowing, some for several years: My dear friends. Special thanks to the Hawayingen crew, that is Juliane, Alex, Chrissie, Marc, Chrissy, Kili, Johanna, Andi, Marion and Boris for all the shared time (please note: order does not imply significance). And yes, there are certainly lots of other people, who I should also mention, like the *Oggi & die Kakerlaken* pubquiz team and the remnants of my FUESE group, especially my neighbor Annika.

So far, so good. Time to close this chapter. Done.

—— Curriculum Vitae

Andreas Johannes Häußler, born January 24, 1984 in Neu-Ulm (Bayern)

Education

05/2011–04/2015	**PhD Student** Institute for Quantum Optics, Ulm University PhD Thesis: *Superresolution Microscopy and Spectroscopy of Single Defect Centers in Diamond*
10/2003–11/2010	**Physics Studies, Diploma degree**, Ulm University Final grade: 1,2 Diploma Thesis: *Kraftmikroskopische Untersuchungen der nanomechanischen Eigenschaften des Zytoskelettproteins Keratin 8/18*
09/1994–06/2003	**Abitur**, Lessing-Gymnasium Neu-Ulm Final grade: 1,2

Lecturing / Teaching

10/2012–03/2015	**Lecturing**, VH Ulm / Aicher-Scholl-Kolleg Class: *Light and Colors*
04/2007–02/2015	**Teaching**, Faculty for Physics, Ulm University Seminars and Lab experiments; Classes in Mechanics, Optics, Electricity and Magnetism, Thermodynamics
10/2012–12/2014	**Presenting**, Faculty for Physics, Ulm University Physics Christmas lecture
08/2013–02/2014	**Educating**, ZAWIW, Ulm University Summer Science Camp 2013, u3gu lecture *Movie Physics*

Professional Experience

05/2014–12/2014	**Projekt Businessplan Ultraschall-App GbR**, Neu-Ulm *Project Manager*, Market Research and Economic Forecasting
12/2013–03/2014	**Projekt IGAV GbR**, Ulm *Assistant*, Homepage Programming
03/2008–02/2009	**Carl-Zeiss Surgical GmbH**, Oberkochen *Student Employee*, Assistance to CEO for Lecturing

Skills

Language	German (native), English (fluent), French (good), Spain (basics)
Programming	Matlab, Python, R, Origin, MS Office, LaTeX, Maple
Interests	Game Theory, Financial Investments, Communication psychology, Creative Writing

Erklärung

Hiermit erkläre ich, diese Arbeit selbstständig angefertigt zu haben. Alle verwendeten Hilfsmittel und Quellen, sowie wörtlich oder inhaltlich übernommene Stellen wurden als solche kenntlich gemacht. Die Satzung der Universität Ulm zur Sicherung guter wissenschaftlicher Praxis wurde berücksichtigt.

Ulm, den 27.04.2015

Andreas Johannes Häußler